Spring 1-1-2018

Dynamics of Complex Spacecraft Subject to Forced and Environmental Charging

Joseph A. Hughes
University of Colorado at Boulder, josephandrewhughes26@gmail.com

Dynamics of Complex Spacecraft Subject to Forced and Environmental Charging

by

Joseph A. Hughes

B.S., Mechanical Engineering, Walla Walla University

Walla Walla, Washington, 2014

B.S., Physics, Walla Walla University

Walla Walla, Washington, 2014

A thesis submitted to the

Faculty of the Graduate School of the

University of Colorado in partial fulfillment

of the requirements for the degree of

Doctor of Philosophy

Department of Aerospace Engineering Sciences

2018

This thesis entitled:
Dynamics of Complex Spacecraft Subject to Forced and Environmental Charging
written by Joseph A. Hughes
has been approved for the Department of Aerospace Engineering Sciences

Prof. Hanspeter Schaub

Dr. Jay McMahon

Dr. Zoltan Sternovsky

Dr. Delores Knipp

Prof. Bruce Jakosky

Date

The final copy of this thesis has been examined by the signatories, and we find that both the content and the form meet acceptable presentation standards of scholarly work in the above mentioned discipline.

Hughes, Joseph A. (Ph.D., Aerospace Engineering)

Dynamics of Complex Spacecraft Subject to Forced and Environmental Charging

Thesis directed by Prof. Hanspeter Schaub

Due to the space plasma environment and the sun, spacecraft can charge to very high negative voltages. These high charge levels can cause arcing which can seriously damage spacecraft electronics and even cause mission ending damage. Spacecraft charging can also cause significant perturbations for lightweight High Area to Mass Ratio (HAMR) objects. If correctly harnessed and directed, charging can be used to exert forces and torques on large debris objects without making physical contact through the Coulomb force. This concept is called the Electrostatic Tractor (ET) and can tug debris out of Geosynchronous Earth orbit (GEO) in a matter of months. To understand both the orbits of uncontrolled charged debris and the performance of the ET, accurate models for how spacecraft charge must be developed, the forces and torques that result from this charging must be estimated, and the effects of these forces and torques must be studied.

Spacecraft charging is studied by finding both equilibrium and time-varying solutions for the voltage. A major change with prior work is to use empirical models for the electron and ion flux rather than Maxwellian models. This, coupled with a more realistic Secondary Electron Emission (SEE) model, predicts that it is harder than previously thought for spacecraft to charge negative. The charging equations are also solved for time varying solutions.

Electrostatic force and torque prediction is advanced using both analytic and numeric tools. Analytic expressions for the force and torque on a geometrically complex object are presented, which give novel analytical insight. Numeric studies include using the Method of Moments (MoM) to create better-performing Multi-sphere Method (MSM) models. The MSM is also extended to model conductors and dielectrics with good accuracy.

The orbital effects of charging are studied for both environmentally charged debris and the ET. For charged debris, it is the electrostatic *torque* that matters since it can change the attitude

and influence Solar Radiation Pressure (SRP). This perturbing force is comparable to an initial attitude uncertainty. For the ET, the new charging model predicts that a few milliAmps of current are needed rather than the few hundred microAmps of current predicted from prior work. Collectively, these studies advance the frontier of knowledge in spacecraft charging, electrostatics, and astrodynamics.

Dedication

To Abby.

Thank you for your undying support and for listening to far too many rants about elastance

---

Acknowledgements

The four and a half years I have spent living in Colorado and attending CU Boulder have been my happiest. I owe this to many wonderful people who have made all of this possible. The first thank you goes to my advisor Dr. Hanspeter Schaub - without you none of this would have been possible. You have set the bar high with your excitement and rigor in the classroom, devotion to research, and utmost passion for good looking figures. Thank you for giving me the freedom to follow research wherever it lead, and for cautioning me when I was too eager. Thank you also to the rest of my committee: Jay McMahon, Zoltan Sternovsk, Delores Knipp, and Bruce Jakosky for your guidance and support.

Thank you to the kind and brilliant members of the AVS lab which have been more than colleagues. Thank you to Carl Seubert, Erik Hogan, Daan Stevenson, and Trevor Bennett for laying the groundwork for my work with the ET. JoAnna Fulton and Pat Kenneally, thank you for helping me to stay sane while going through classes and prelims in our first years. To all those who worked with me on electrostatics; Phillip Chow, Gabe Ingram, Jordan Maxwell, Heiko Engwerde, and Iosto Fodde, your contributions have made this work possible. And also thank you Miles Bengtson, Jordan Maxwell, and Kieran Wilson for picking up the torch and running with it. I am excited to see where you take it.

Thank you also to my family. More than anyone else you have made me who I am. Thank you for supporting whatever I happened to be interested in whether it be lizards or old Japanese cars. Thank you for instilling in me a love of science and the natural world. Thank you for sending me to science camps and taking me hiking. Lastly thank you to my wonderful group of friends who

have travelled this incredible journey with me. Every turn we have skied, trail we have biked, and pitch we have climbed have made me these years productive and worthwhile.

Contents

Chapter

Tables

Table

Figures

Figure

Chapter 1

Introduction

1.1 Background and Motivation

Due to interactions with the space plasma environment and the sun, spacecraft can charge naturally to negative 10s of kiloVolts. This charging has many bad effects such as arcing and difficult-to-predict perturbations for uncontrolled space debris but can also be leveraged for touchless actuation. This dissertation studies the effects of passive charging on the orbits of passive debris objects and the effects of active charging for the Electrostatic Tractor.

Although space is often thought of as being completely empty, it is actual full of plasma. In Geosynchronous Earth Orbit (GEO), the plasma is hot and tenuous with densities near 1 particle per cm^{-3} and thermal energies of a few keV. These electrons, ions and photons impact spacecraft and can cause spacecraft charging. Because electrons are much lighter than ions, they move much faster than ions with the same energy and many more of them impact a spacecraft which tends to charge a spacecraft negative. However, solar photons cause photoelectric emission on the spacecraft which is a positive current. Additionally, high energy electrons and ions can impact the spacecraft and eject electrons which causes an additional positive current to the spacecraft. Artificial currents from electron and ion guns are also considered for some scenarios. All of these currents contribute to spacecraft charging, and can result in dramatic positive or negative voltages depending on the environment. In GEO, most spacecraft float at +10 V in sunlight most of the time, but the SCATHA mission showed that charging naturally to -10 kV in Earth's shadow is possible [6, 7] and the ATS-6 spacecraft set the record for charging at a measured -19 kV [8].

Many applications seek to harness and control this charging for novel missions. For instance, a number of mission concepts have been proposed to purposely charge a spacecraft so that is pushed by the Earth's magnetic field through the Lorentz field to change its orbit without expending fuel [9, 10, 11]. Some concepts propose running current through a long electrodynamic tether for propellentless orbital changes. The tether still makes use of the Lorentz force, but the velocity is greater since the electrons velocity is the sum of the orbital motion of the spacecraft with their velocity due to the current. This tether can be deployed at end of life and used to de-orbit spacecraft in LEO [12, 13].

Although charging can have advantageous uses if controlled, it can cause mission-ending damage if it is not. If the spacecraft is not continuously conducting, different parts of the spacecraft can charge to different levels and arc, which can cause mission-ending damage to spacecraft electronics. For instance, the DSCS II, GOES 4, Fengyun 1A, MARECS A, Anik E1, Telstar 401, INSAT 2, Tempo 2, PAS-6, and ADEOS - II missions were all lost due to spacecraft arcing related failures [4]. One particular case of arcing is a sustained arc, where the current from a solar panel continuously powers an arc much like an arc welder rather than charging the battery [14]. Differential charging can also artificially increase or reduce the flux of charged particles to a detector. High energy flux can harm spacecraft electronics through Single Event Upsets (SEU) or Single Event Burnouts (SEB).

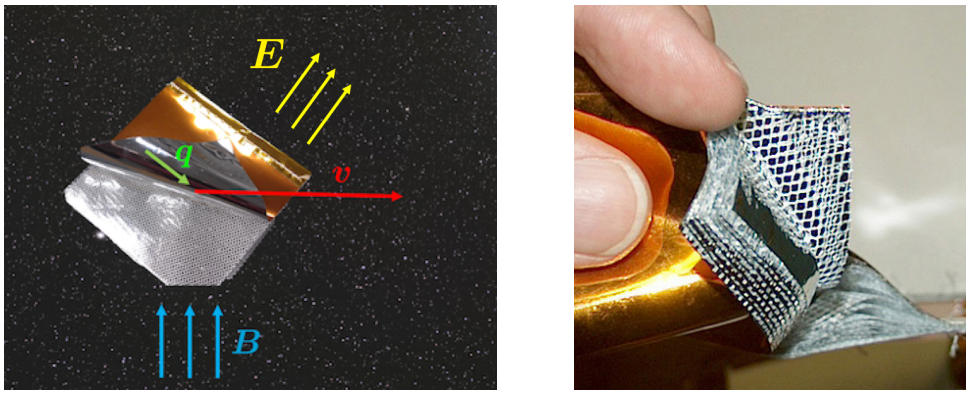

(a) Electromagnetic perturbations (b) MLI shown with layers exposed

Figure 1.1: MLI with charging perturbations

In addition to arcing, recent work by [2, 15, 16, 17] suggests that spacecraft charging can affect the orbits of lightweight debris objects such as the piece of Multi-Layer Insulation (MLI) shown in Fig. 1.1. All spacecraft are subject to a number of small forces that perturb their orbits from the closed-form conic section solution to the two body problem. At low altitudes, Earth's non-spherical gravity and drag strongly perturb certain orbits. Further out in GEO, all objects are perturbed by lunar and solar gravity, and some High Area-to-Mass (HAMR) objects are strongly perturbed by Solar Radiation Pressure (SRP) [18]. However, not all orbits are explained using just the above perturbations, Wiesel [19] reports some near-GEO debris objects which appear to accelerate *towards* the sun during the propagation interval, which is impossible with only SRP disturbances. The source of this discrepancy is speculated to be that these objects are interacting with Earth's magnetic field. Some of these unknown objects are thought to be torn-off pieces of MLI as discussed by [20]. Samples returned from the Hubble Space Telescope showed cracks in areas of constrained loading, and [21] discuss a tendency of MLI to curl up when peeling off.

While these pieces of MLI weigh only a few grams, they will have closing velocities of near 1 km/sec with objects in nominal GEO orbit if their inclination gets pulled up to $\sim 16^\circ$ by the moon's gravity [22]. This represents similar momentum to a low-caliber bullet and if the debris were to hit an operational spacecraft, it could easily damage sensors or solar panels. Understanding the orbits of such debris objects is crucial to predicting and preventing collisions.

GEO is a very unique and valuable orbit - satellites in GEO do not move when viewed from earth which makes them excellent platforms for telecommunications and earth observation. In 2011, all the civil, commercial, and defense assets in GEO were insured for $18.3 billion [23]. In 2016, the total value of all space assets (not just GEO) was estimated at $261 billion, up from $177 billion in 2011 [24]. Assuming the insured value of GEO grows linearly with time gives an estimated insured value for GEO assets in 2018 of over $30 billion. Alarmingly, of the 1369 tracked objects in GEO in 2011, only 21% were controlled [23]. Worse yet, many of those uncontrolled objects are not lightweight pieces of MLI, but rather multi-ton satellites that could cause even more damage.

Whereas natural forces such as atmospheric drag exist in Low Earth Orbit which will deorbit

objects over time, no such forces exist in GEO and objects in orbit will remain indefinitely [25]. The number of active satellites in GEO is steadily increasing along with the number of mission-related debris, such as rocket bodies or kick motors. The risk of collision has been identified as a hazard for operational and future missions. In an effort to reduce the congestion in GEO, the Inter-agency Space Debris Coordination Committee (IADC), an international governmental forum, has established end-of-life disposal guidelines for satellites in GEO, recommending a minimum altitude boost of at least 235 km be performed [26]. These guidelines, however, are only followed on a voluntary basis by operators. End-of-life orbit-raising maneuvers can be costly and operators must decide between extending operations and risking not being able to raise the orbit, or voluntary orbit raising [27]. Further, there are often uncertainties in the remaining propellant mass and satellites commonly do not achieve the desired altitude. Between 1997 and 2003, approximately 2 out of every 3 retired satellites raised their orbit to an insufficiently high altitude or did not even try [28]. More recently the compliance rate with GEO operators has improved where in 2013 the 20 satellites that reached end-of-life status were all attempted to be moved to the disposal orbit [29]. However, only 15 such disposal maneuver were fully successful.

This crowding of large, often school-bus sized objects creates the probability of collision, which is expected to worsen with current launch and re-orbiting trends [30, 22]. Although much orbital debris research focuses on the Low Earth Orbit (LEO) regime, Oltrogge shows that the spatial densities in GEO can be as high as those in LEO [31]. Anderson [22, 30] determines that given the imperfect mitigation efforts, the number of near-miss events near gravitational wells will double in 50 years. Multiple studies conclude that mitigation measures must be combined with active debris removal to ensure the long-term safety and usability of the GEO ring [32, 33, 23, 34].

The need for remediation was demonstrated on February 10, 2009 when the American Iridium 33 satellite collided with the Russian Cosmos 2251 satellite above Siberia as depicted in Fig. 1.2. These two spacecraft had an altitude of 790 km and a closing speed of 11.7 km/s [35]. The collision created at least 1,000 pieces of debris larger than 10 cm, and much more smaller debris. Although Cosmos was defunct and could not have avoided the crash, Iridium was operational but its operators

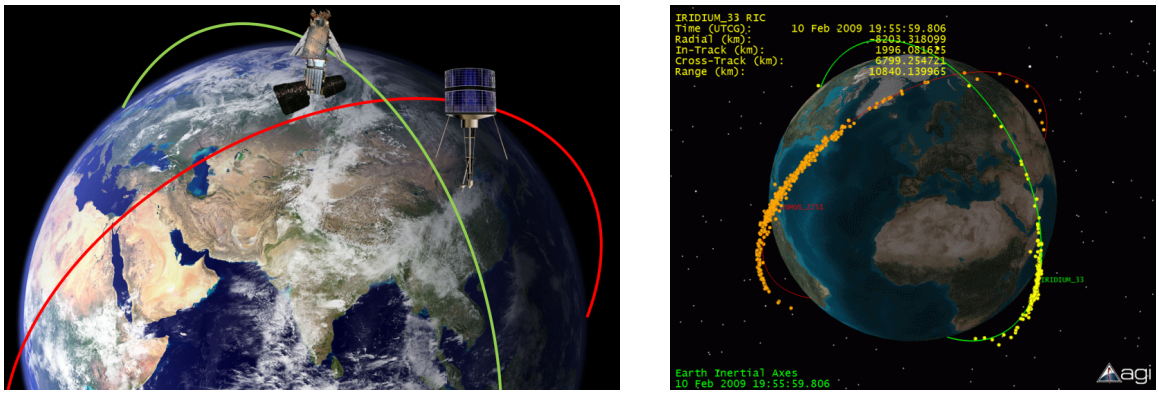

(a) Illustration of Iridium and Cosmos orbits before collision

(b) Orbital debris created from Iridium-Cosmos collision [1]

Figure 1.2: Iridium-Cosmos collision

decided not to perform the maneuver to conserve fuel. This decision did not seem risky at the time since the predicted miss distance between the two spacecraft was 584 m [36] and this was not even in the top ten list of near misses for the week. Nevertheless, the two spacecraft did definitely collide and much of the debris is still in orbit.

To reduce the collision probability, many concepts have been proposed to move GEO debris into a graveyard orbit. Many studies propose using a net [37] or harpoon [38, 39, 40, 41] to capture debris and then tug it to a higher orbit. A recent experiment launched from the International Space Station will perform on-orbit testing of net and harpoon systems [42] with a simulated debris object. Other studies investigate the dynamics of the physical tether which must be able to withstand a high-force tugging [43, 44, 45]. These methods present a number of advantages and disadvantages. Once contact is made the tug spacecraft can use its thrusters to raise the debris semi-major axis in only a few orbits. However, even in the event the capture system hits the target, it may not fully capture it. The structural integrity of retired satellites is uncertain and the debris is only pulled at a single point of contact, so there is also a risk that the target object would breakup, thereby worsening the debris situation. The number of objects which can be deorbited with this method is also limited by the number of dispensables such as nets or harpoons on board the chief craft.

Other work focuses on developing robotic grapplers to interface with debris objects [46, 47,

48, 49, 50]. Whereas the disadvantages of firing objects at the debris are avoided with this method, it is extremely technically challenging and financially expensive to grapple with an uncooperative object which may have unknown mass characteristics. Extremely close proximity operations are also required, which carries a high risk of creating large amounts of additional debris in the event of a mission failure. Again, the structural integrity of the debris may be unknown and solar panels or antennas may break off during the grappling process. Finally, robotic arms cannot grapple objects with rotations rates greater than a few degrees per second, whereas debris objects are commonly rotating at 10s of degrees per second, so significant propellant mass may be required to match the relative rotation rate of a tumbling object, thereby limiting the financial effectiveness of such a mission [51, 52]. As another solution, missions have been proposed to distribute reorbiting kits, add-on propulsion modules which would be attached via robotic arm and then provide the required thrust for reorbit [53, 54]. Disadvantages of this method are the difficulty in placing the module and the need for pointing control to provide the proper thrust vector as well as the "single use" weight in each reorbiting kit.

Methods have been proposed for touchless detumbling of space debris, including electrostatic actuation, laser ablation of surface material such that the resulting ejecta provides an impulse to alter the target's attitude [55], eddy currents in the target induced by a magnetic field generated by a servicing craft [56], as well as the ion-shepherd method that employs the ion engine exhaust to push the debris object [57, 58].

Another family of concepts use the Coulomb force between a pair of charged spacecraft to exert touchless forces and torques. If a servicing vehicle irradiates a passive space object with an electron beam, the servicer charges positive and the passive craft charges negative resulting in an attractive Coulomb force between them. This force can be used for small orbital corrections in a formation flying mission with negligible use of propellant [59, 60, 61, 62]. The concept has broad applicability with propellent-free formation flying and docking or servicing.

One special case of this concept is the called the Electrostatic Tractor (ET) shown in Fig. 1.3 where a tug craft pulls a piece of space debris from geosynchronous orbit into a graveyard orbit

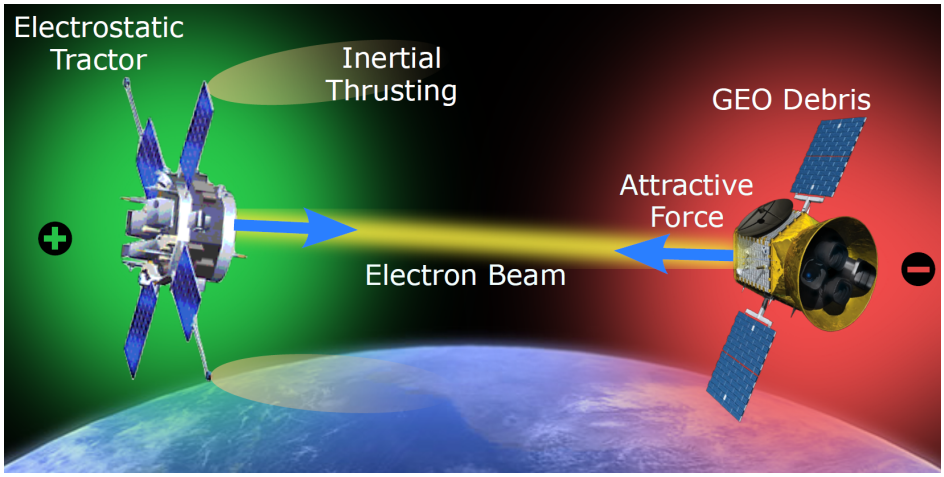

Figure 1.3: Electrostatic Tractor concept of operations [3]

[63, 64, 3]. For two moderately sized spacecraft (3 m diameter) charged at ±20 kV, and separated by 7 craft radii, the debris feels a 1.2 mN force that could raise its orbit by more than 5 km/day [65]. A tug craft equipped with an electron gun and low thrust motors could move defunct GEO satellites to a graveyard orbit in a matter of months [65]. Additionally, spacecraft with non-symmetric charge distributions will also feel and apply torques through this charging [66, 67, 68, 5]. This torque can be used to touchlessly detumble non-cooperative space objects in a matter of days [69] depending on the debris inertia and spin rate.

There are many separate challenges when studying how spacecraft charging, either natural or forced, can affect spacecraft kinetics. For the purposes of this dissertation they can be thought of in three key steps as shown in Fig. 1.4. First, to what voltage does a spacecraft charge to in the space environment both naturally or with electron and ion beams? Second, what are the forces and torques on a spacecraft due to this charging? Third, how do these electromagnetic forces and torques change the dynamics of a spacecraft? This work develops new insights in each of these three categories. In combination with these three steps, there are also 2 main applications: first the electrostatic tractor, and second the problem of lightweight charged debris. In total these three steps and two applications divide this very large and onerous problem into six more tractable pieces – the charging, forces, and orbital effects on lightweight debris and for the ET concept.

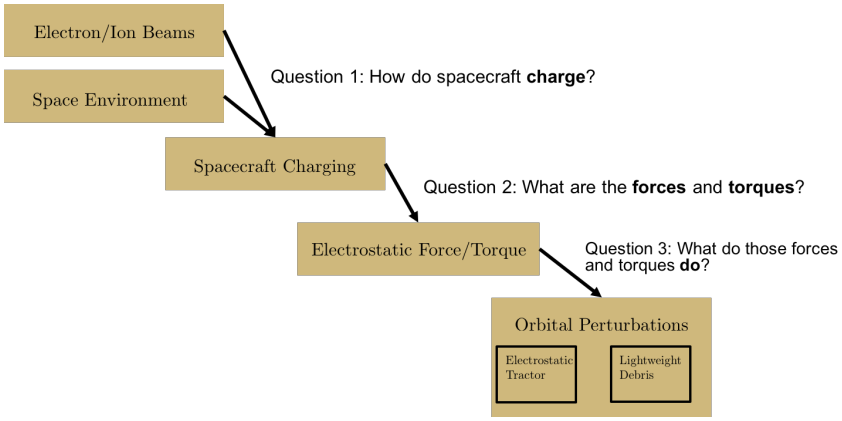

Figure 1.4: Organizational chart for understanding the effects of spacecraft charging

1.2 Literature Review

1.2.1 Spacecraft Charging

Spacecraft charging started to receive considerably more attention from aerospace engineers when spacecraft in orbit began to suffer electronic anomalies due to charging and arcing. Minnow and Parker [4] curated a list of spacecraft charging related impacts to missions which is shown in Fig. 1.5. In this counting, there have been 11 lost missions due to spacecraft charging with the majority of these losses (8/11) at GEO. Due to these mission losses, much work has been devoted to the topic [70, 71].

Because of spacecraft charging has its roots in plasma probe theory, and because of ease, Maxwellian distributions are commonly used to model the space environment. A plasma at equilibrium should be Maxwellian, but many space and laboratory plasmas are either double Maxwellian or significantly non-Maxwellian. When the plasma is non-collisional, it can take a long time to reach equilibrium and become Maxwellian. While numerous theoretical and experimental studies have investigated spacecraft charging in the presence of an electron beam [72], there is little work with high energy electron beams. Additionally, all of these studies are for a single spacecraft attempting to control its own potential rather than to control both its and a debris object's potential as in the ET.

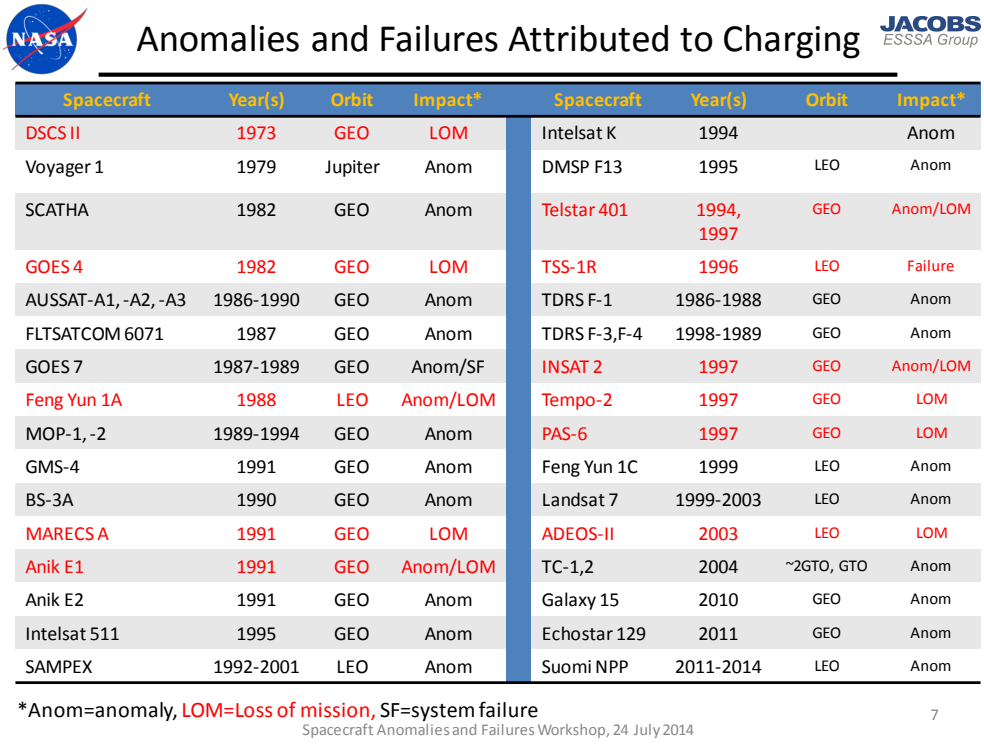

Anomalies and Failures Attributed to Charging

JACOBS ESSSA Group

Spacecraft	Year(s)	Orbit	Impact*	Spacecraft	Year(s)	Orbit	Impact*
DSCS II	1973	GEO	LOM	Intelsat K	1994		Anom
Voyager 1	1979	Jupiter	Anom	DMSP F13	1995	LEO	Anom
SCATHA	1982	GEO	Anom	Telstar 401	1994, 1997	GEO	Anom/LOM
GOES 4	1982	GEO	LOM	TSS-1R	1996	LEO	Failure
AUSSAT-A1, -A2, -A3	1986-1990	GEO	Anom	TDRS F-1	1986-1988	GEO	Anom
FLTSATCOM 6071	1987	GEO	Anom	TDRS F-3,F-4	1998-1989	GEO	Anom
GOES 7	1987-1989	GEO	Anom/SF	INSAT 2	1997	GEO	Anom/LOM
Feng Yun 1A	1988	LEO	Anom/LOM	Tempo-2	1997	GEO	LOM
MOP-1, -2	1989-1994	GEO	Anom	PAS-6	1997	GEO	LOM
GMS-4	1991	GEO	Anom	Feng Yun 1C	1999	LEO	Anom
BS-3A	1990	GEO	Anom	Landsat 7	1999-2003	LEO	Anom
MARECS A	1991	GEO	LOM	ADEOS-II	2003	LEO	LOM
Anik E1	1991	GEO	Anom/LOM	TC-1,2	2004	~2GTO, GTO	Anom
Anik E2	1991	GEO	Anom	Galaxy 15	2010	GEO	Anom
Intelsat 511	1995	GEO	Anom	Echostar 129	2011	GEO	Anom
SAMPEX	1992-2001	LEO	Anom	Suomi NPP	2011-2014	LEO	Anom

*Anom=anomaly, LOM=Loss of mission, SF=system failure

Spacecraft Anomalies and Failures Workshop, 24 July 2014 7

Figure 1.5: Historical list of notable spacecraft charging related deleterious effects [4]

There has also been analysis of the charging aspect of the ET, starting with Schaub and Sternovsky [73] analysis which includes photoelectron currents, ion and electron thermal currents, the electron beam and its resulting Secondary Electron Emission (SEE), but ignores SEE and backscattering from the thermal currents. Only the beam and electron current are considered for the tug, which allows the tug voltage to be found analytically. Later on, Hogan and Schaub [74] used the same charging model but looked at the effects of a geomagnetic storm which changes the space environment (still modeled by Maxwellian distributions) on the performance of the ET and found only small changes to the ET performance. Hogan and Schaub also looked at the normal variations in the plasma environment over an orbit in [75] and found that although there is a more optimal solution which modulates the current and energy of the electron beam over an orbit, a set current produces similar results. Stevenson and Schaub also looked at the charge-up time in [76] for the electrostatic detumble which required them not to find the equilibrium charging configuration but to numerically integrate the currents through time. All of this work uses Maxwellian descriptions

of the plasma environment, neglects SEE and backscattering from the thermal currents, neglects backscattering from the electron beam, and furthermore uses only one model of SEE which was developed in 1979 for micron-sized dust grains [77].

1.2.2 Electrostatic Force Prediction

Knowing what the Coulomb force will be between two spacecraft charged to arbitrary voltages in the space environment is a complex problem. Most studies ignore plasma shielding as the Debye length at GEO is considerably larger than the planned separation between spacecraft, and shielding may be even less of an issue due to the high voltages [78]. Closed-form analytical solutions for the Coulomb force exist for the special case of a point near an infinite plate in vacuum [79] using the method of images, and a rapidly converging infinite series solution is given in [80] for two nearby spheres. A necessarily less concise approach is given in [81] for the case of an arbitrary number of spheres.

Numerical methods also exist for finding the Coulomb force in vacuum. Many commercial electromagnetic Finite Element Analysis (FEA) programs such as COMSOL and ANSYS have the ability to calculate Coulomb force, but it is nearly always slower than realtime and is also very sensitive to the mesh. The Multi-Sphere Method (MSM) was developed by Stevenson and Schaub [67] to address this issue. MSM approximates a spacecraft as a collection of equipotential spheres and uses an elastance matrix to calculate the charge on each sphere and then apply the Coulomb force law between each pair of spheres. The radius and location of each sphere are optimized to match the force and torque or E field predicted by a higher fidelity FEA program. This approach differs from the Method of Moments (MoM) which derives the location and capacitance of the nodes from first principles.

The MSM divides into *Volume* MSM (VMSM) and *Surface* MSM (SMSM). The guiding principle behind SMSM is to place many spheres uniformly on the surface of the object rather than in the volume of the object and vary the radius of all spheres so that the SMSM model has the same self capacitance as the object being modeled [120]. This approach is much easier to set

up than VMSM because there is no optimization for the location or size of the spheres, but much slower to evaluate due to the large number of spheres. The optimization for a general VMSM model has $4N$ free parameters for an N sphere MSM model which leads to very difficult optimizations. Nonetheless, 2 sphere models can deliver less than 2% error for template box and panel spacecraft shapes [130].

1.2.3 Electromagnetic Orbital Effects

The concept of electrostatic actuation was first explored as early as 1966 to inflate reflecting membranes [82]. In the early 2000s, the concept re-gained popularity both with Coulomb and Lorentz based schemes. Peck and others have proposed that the Lorentz force could be used to change the orbits of earth-orbiting satellites with no propellent use [83, 84, 9]. Electrostatic charge manipulation is also considered for cooperative spacecraft formation flying where each craft could manipulate its own charge. Ion or chemical thrusters for position control are undesirable in close proximity formations on the order or multiple craft radii due to the thruster plumes that can impinge upon and contaminate other craft in the formation [85]. Forces on the order of tens of milli-Newtons (corresponding to potential levels up to 20 kiloVolts and miliAmps of current) are found to be sufficient for maintaining High Earth Orbit formations of spacecraft with spacings less than 100 meters, ideal for maintaining the sparse apertures needed for interferometry applications [85, 86]. These concepts for relative motion control are appealing, as they are effectively propellantless, use less power than any available electric thrusters, and avoid potential contamination of nearby spacecraft that could be detrimental to delicate sensors. The dynamics and control of such formations, which range from simple 2 craft formations to complex N-body configurations, are discussed further in [62, 87, 88, 59, 89, 90]. The electrostatic tractor concept is first proposed as a mechanism for debris reorbiting in GEO by Schaub and Moorer in 2011 [91, 92, 64]. The electrostatic tractor has since been studied extensively as a way to touchlessly move GEO debris safely to a graveyard orbit [64, 63, 93, 74, 94] as well as for asteroid deflection [95]. All previous studies on the ET have focused on a constant beam current.

The orbital effects of charging on uncontrolled debris objects has gained traction in the last few years. Früeh et al. [2] were the first to publish results modeling the electrostatic charging effects on HAMR objects. This initial work adds the Lorentz force and eddy torque to the more standard list of perturbations for a HAMR plate. Including these two new effects changes the orbit by nearly a tenth of a degree in inclination and 0.002 in eccentricity after only 12 hours. Paul and Früeh [15] model a sphere for which torques are not included and found much less dramatic results. These two works have either attitude-dependent SRP, or a realistic charging model, but not both at the same time. Additionally, they do not delve into the specific mechanisms by which charging can affect the orbits, for which objects charging will play the greatest role, or compare the strength of these perturbations to the natural spread from initial attitude.

1.3 Dissertation Outline

The proposed research advances all three of these categories. In the first category the charging equations are solved numerically through time with SEE and backscattering currents accounted for as well as a more realistic and modern model of SEE. Additionally, measured distributions for GEO will be used rather than Maxwellian distributions. In the second category MSM is linked to MoM to better understand how to place and size the spheres for general objects. MSM is expanded to include modeling dielectrics. Additionally, closed-form analytic expressions for the Coulomb force and torque between two conductors are developed using a binomial expansion. This provides analytical insight for electrostatic actuation as opposed to strictly numerical methods. In the last category, the performance of the ET is studied with the more realistic charging and storm models. Higher-fidelity charging models are also used to study the orbits of lightweight HAMR debris, and the specific mechanisms by which electrostatics can change the orbits are found. The objects for which these perturbations are the most significant are categorized.

1.4 Contributions

The main contributions of this research are divided by topic and summarized below.

- Spacecraft Charging
  - Time-varying solution to two-body active charging
  - Inclusion of Secondary Electron Emission (SEE) and backscattering from environmental electrons
  - SEE from isotropic flux using modern SEE models
  - Comparison of charging with Maxwellian vs. empirical flux models
- Electrostatic Force and Torque Prediction
  - Closed-form analytic expressions for force and torque found for general conductors as functions of the voltages
  - Implementation of the Method of Moments and comparison to SMSM
  - Modification of MSM to include dielectrics
- Electrostatic Orbital Effects
  - Mechanism for orbit changes through charging found
  - Comparison between attitude uncertainty and electromagnetic perturbations
  - Pulsed electron beam analysis performed for ET
  - Normalized charging model for ET created

1.5 Publications

The following journal and conference papers are the results of the work completed in this thesis:

1.5.1 Journal Papers

- J. Hughes and H. Schaub, "Prospects of Using a Pulsed Electrostatic Tractor With Nominal Geosynchronous Conditions," **IEEE Transactions on Plasma Science**, Vol. 45, No. 8, 2017, pp. 1887–1897. doi:10.1109/TPS.2017.2684621

- J. Hughes and H. Schaub, "Spacecraft Electrostatic Force and Torque Expansions Yielding Appropriate Fidelity Measures," Submitted to **Journal of Astronautical Sciences.**

- J. Hughes and H. Schaub, "Rapid Charged Geosynchronous Debris Perturbation Modeling of Electromagnetic Disturbances," **Journal of Astronautical Sciences**, Vol 65, No 2, 2018, pp. 135 – 156. doi:https://doi.org/10.1007/s40295-017-0127-3

- J. Hughes and H. Schaub, "Space Weather Influence on Electromagnetic Geosynchronous Debris Perturbations Using Statistical Fluxes," **AGU: Space Weather**, Vol. 16, No. 4, 2018, pp. 391–405. doi:https://doi.org/10.1002/2017SW001768.

- J. Hughes and H. Schaub, "Electrostatic Tractor Analysis Using a Measured Flux Model," Submitted to **Journal of Spacecraft and Rockets.**

- J. Hughes and H. Schaub, "Heterogeneous Surface Multi-Sphere Models using Method of Moments Foundations," In Preparation for **Journal of Spacecraft and Rockets.**

- J. Hughes and H. Schaub, "Rapid Modeling of Electrostatic Forces and Torques Considering Dielectrics," In Preparation for **Acta Astronautica.**

1.5.2 Conference Papers

- **J. Hughes**, and H. Schaub, "Appropriate Fidelity Electrostatic Force Evaluation Considering a Range of Spacecraft Separations," In AAS/AIAA Spaceflight Mechanics Meeting, Napa Valley, California, Feb. 14–18, 2016

- P. Chow, **J. Hughes**, T. Bennett, and Hanspeter Schaub. "Automated Sphere Geometry Optimization For The Volume Multi-Sphere Method ", In AAS/AIAA Spaceflight Mechanics Meeting, Napa Valley, California, Feb. 14–18, 2016

- **J. Hughes** and H. Schaub. "Monte Carlo Analysis of the Pulsed Electrostatic Tractor Strength," In 14th Spacecraft Charging Technology Conference, ESTEC, Netherlands, April 4–8, 2016

- H. Schaub, T. Bennett and **J. Hughes**,"Current Developments in Three-Dimensional Electrostatic Detumble of Axi-Symmetric GEO Debris," 4th International Workshop on Space Debris Modeling and Remediation, CNES, Paris, June 6–8, 2016. Paper No. 6.4

- **J. Hughes** and H. Schaub. "Charged Geosynchronous Debris Perturbation Using Rapid Electromagnetic Force and Torque Evaluation," In Advanced Maui Optical and Space Surveillance Technologies Conference, Maui, Hawaii, Sep 20–23, 2016

- H. Engwerda, **J. Hughes**, and H. Schaub, "Remote Sensing for Planar Electrostatic Characterization using the Multi-Sphere Method," Stardust Final Conference on Asteroids and Space Debris, ESTEC, Netherlands, Oct 31–Nov 4 2016.

- G. Ingram, **J. Hughes**, T. Bennett, C. Reily, and H. Schaub. "Autonomous Volume Multi-Sphere-Model Development Using Electric Field Matching," In AAS Spaceflight Mechanics Meeting, San Antonio, Texas, Feb 5–9, 2017

- **J. Hughes** and H. Schaub. "Rapid Charged Geosynchronous Debris Perturbation Modeling Of Electromagnetic Disturbances," In AAS Spaceflight Mechanics Meeting, San Antonio, Texas, Feb 5–9, 2017

- **J. Hughes** and H. Schaub. "Spacecraft Electrostatic Force And Torque Expansions Yielding Appropriate Fidelity Measures," In AAS Spaceflight Mechanics Meeting, San Antonio, Texas, Feb 5–9, 2017

- **J. Hughes** and H. Schaub, "Orbital And Storm Time Analysis Of The Pulsed Electrostatic Tractor," European Conference on Space Debris, ESOC, Darmstadt, Germany, April 18–21, 2017

- **J. Hughes** and H. Schaub, "The Impact of Space Weather on GEO Space Debris Orbit Evolution," Space Weather Workshop, Broomfield, Colorado, May 1–5, 2017.

- **J. Hughes** and H. Schaub. "Effects of Charged Dielectrics on Electrostatic Force and Torque." In International Workshop on Spacecraft Formation Flying, Jun 19–21, 2017

- **J. Hughes** and H. Schaub, "Effects of Space Weather on Geosynchronous Electromagnetic Spacecraft Perturbations Using Statistical Fluxes," AGU Fall Meeting, New Orleans, Louisiana, December 11–15, 2017.

- **J. Hughes** and H. Schaub, "Electrostatic Tractor Analysis Using a Measured Flux Model," 15^{th} Spacecraft Charging Technology Conference, Kobe, Japan, June 24-29, 2017.

- **J. Hughes** and H. Schaub, "Rapid Modeling of Electrostatic Forces and Torques Considering Dielectrics," International Astronautical Congress, Bremen, Germany, Oct 1 - 5, 2018.

Chapter 2

Spacecraft Charging

This chapter answers the first of the three questions: How do spacecraft charge? A space object is subject to many currents from the space plasma and the sun as shown in Fig. 2.1. The main currents are the thermal electron and ion currents ($I_{\mathrm{e}}, I_{\mathrm{i}}$), secondary electron emission (SEE) from both electrons and ions ($I_{\mathrm{SEE}_e}, I_{\mathrm{SEE}_i}$), electron backscattering (I_{b}), the photoelectric current (I_{ph}), and the beam current (I_{beam}).

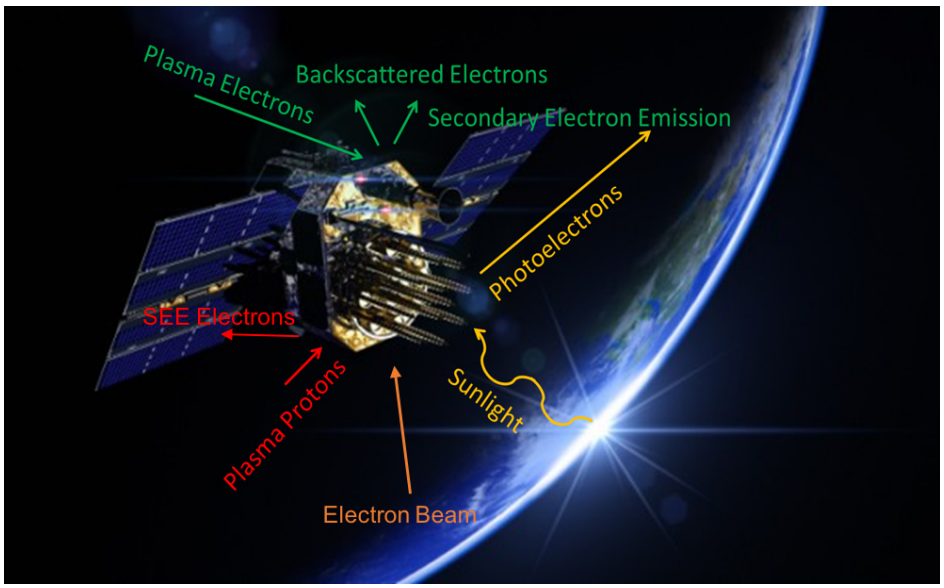

Figure 2.1: Major currents for a geostationary spacecraft

All these currents add together to change the charge of the spacecraft, which changes the voltage, which in turn changes the currents. This Ordinary Differential Equation (ODE) is shown in Eq. (2.1) and can be solved for a time varying voltage or an equilibrium voltage. Because the

charging time for spacecraft is so short, the equilibrium solution is sufficient in most cases.

$$I_{\mathrm{e}}(\phi) + I_{\mathrm{i}}(\phi) + I_{\mathrm{SEE}_e}(\phi) + I_{\mathrm{SEE}_i}(\phi) + I_b(\phi) + I_{\mathrm{ph}}(\phi) + I_{\mathrm{beam}}(\phi) = 0 \tag{2.1}$$

The first charging model developed in this study was in [96]. It included the thermal electron and ion currents ($I_{\mathrm{e}}, I_{\mathrm{i}}$), secondary electron emission (SEE) and backscattering from electrons, the photoelectric current (I_{ph}), and the beam current (I_{beam}). It used Maxwellian models for the thermal currents, neglected SEE from incident ions, and used a SEE model from [97] assuming normally incident electrons. Since the electron beam is pulsed at a fast frequency, the time-varying voltage is found for two spacecraft by numerically integrating the ODE at each time step.

Next, a model for purely environmental charging is developed in [17]. This model has many changes and is much more accurate. Rather than Maxwellian currents, this charging model uses empirical fluxes provided by [98] to calculate the thermal currents, SEE, and backscattering. Ion-induced SEE is included and a new model for electron-induced SEE is used as well. Since there is no pulsed electron beam and the environment changes slowly with local time, only the equilibrium solution is needed.

The most recent and most accurate charging model is presented in [99]. This charging model is based on that used in [100]. The main differences are that the beam current is included, the model for electron induced yields is changed to the NASCAP-2k model [101], and all yields other than that from the beam current assume isotropic flux rather than normal incidence. Since this paper investigates pulsed electron beams with long pulse periods, the equilibrium solution is sufficient.

This chapter first discusses the plasma environment in which spacecraft charge with emphasis on empirical vs Maxwellian distributions. Next, the models for all the major currents in Eq. (2.1) are described. For brevity, only the most recent current models which are used in [99] are presented. Finally, solutions for both the time varying, from [96], and equilibrium solutions for both the environmental [17] and ET [99] are presented.

2.1 The Geosynchronous Orbit Charging Environment

The geosynchronous orbit regime lies near the boundary between the inner and outer magnetosphere at a radius of ∼6.6 Earth radii or 42,164 km. The motion of the plasma in the inner magnetosphere is governed mainly by curvature and gradient drift, while the outer magnetosphere transitions to the global magnetospheric convection cycle. For the purposes of spacecraft charging, the electron and ion populations are often approximated as single or double Maxwellian distributions.

In early analysis of charging for the ET, [73, 74, 75], electrons were modeled by a single Maxwellian with $n_E \sim 1$ cm^{-3} and $kT_E \sim 1$ keV and ions by a single Maxwellian with $n_I \sim 1$ cm^{-3} and $kT_I \sim 50$ eV. In contrast, the spacecraft charging community often uses much hotter distributions corresponding to the ring current particles for both ions and electrons with temperatures in the 10s of keV for electrons and near 30 keV for ions [102].

Denton et al. [98] present an empirical model that uses 82 satellite-years of observed electron and ion flux data. Both populations are measured by Magnetospheric Plasma Analyzers (MPAs) on board multiple Los Alamos National Labs (LANL) satellites. The MPAs are capable of measuring the flux between 1 eV and 40 keV in three spatial dimensions every 86 seconds. All of this data is tagged with local time (LT), K_P index, and solar wind electric field (vB_z), which allows interpolation on a variety of cases. The model allows users to specify three inputs (Energy, LT, and K_P or vB_z) and outputs the mean, median, and percentile flux values. This work considers a calm case where $K_P = 2-$ and a severe storm with $K_P = 8$. Because the flux is only measured between 1 eV and 40 keV, it is not a complete picture of the environment since there is flux at both higher and lower energies. Also, the measured electron flux at low energies is a combination of the natural space environment and the secondary and photoelectrons generated by the spacecraft itself. Additionally, because the spacecraft is sometimes negative, it will turn away environmental electrons with less energy than the spacecraft's voltage. These two effects both obscure the true environmental electrons below ∼ 100 eV. These contaminations of the electron data and the missing

data above 40 keV and below 1 eV are sources of error. For instance, the total density of electrons in the late night sector at K_P = 2- is slightly less than 1 cm^{-3}, but the ion density is between 2 and 4 cm^{-3}. If this were true it would seriously violate the principle of quasi-neutrality, which indicates that around 1-3 cm^{-3} of electrons are not counted in this dataset.

To investigate the sensitivity of the following charging analysis to a missing population of electrons, intermediate results were computed with an added Maxwellian population with low density (10^{-5} cm^{-3}) and high temperature (200 keV) [103], as well as a dense (0.1 cm^{-3}) and cold (5 eV) population. The tenuous population makes no significant difference to the charging, but the dense and cold one does reduce the charging.

Additionally, while there is a lot of data from which to produce the mean fluxes at $K_P = 2-$, there is not much at all from which to estimate the mean flux at $K_P = 8$. This level of storm is incredibly rare, occurring only ~0.1% of the time. Thus, these statistics may not reflect the true mean at such a high K_P value.

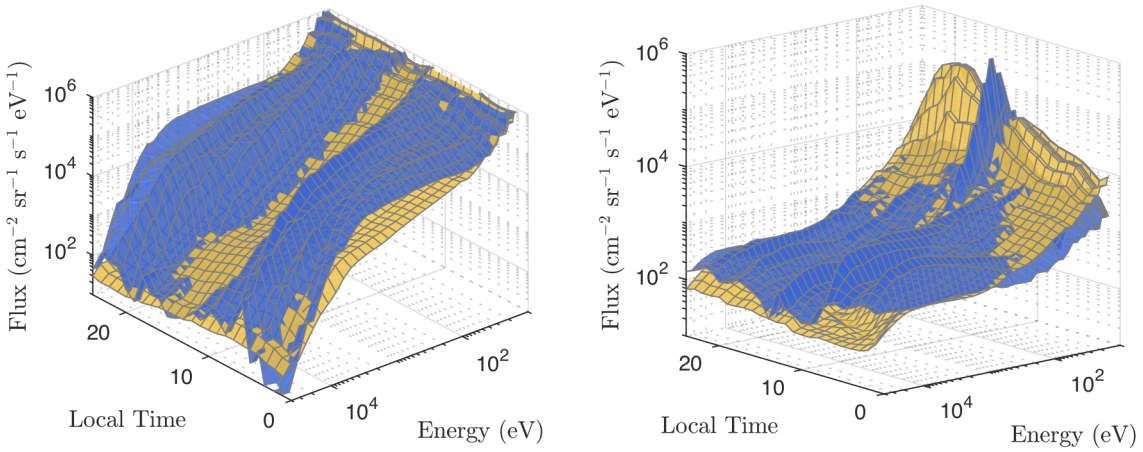

(a) Empirical Electron Fluxes

(b) Empirical Ion Fluxes

Figure 2.2: Differential ion and electron fluxes at GEO for K_P = 2- (yellow) and $K_P = 8$ (blue) as well as commonly used Maxwellian fits

The statistical mean electron fluxes for GEO are shown in Fig. 2.2a, with the yellow sheet indicating $K_P = 2-$ and the blue sheet for $K_P = 8$. For the calm condition, the flux monotonically decreases with energy and is fairly smooth with respect to local time. The storm flux is higher

nearly everywhere and has a definite hump ∼1 keV, and a dramatic trough near local noon. There is also a lot more noisy texture with respect to local time.

The ion fluxes are shown with the same colors indicating the same K_P indices in Fig. 2.2b. The ion fluxes are more flat with respect to energy than the electron fluxes, but have a more distinct peak at low energy. Once again the storm flux is higher and more textured with respect to local time, although the low energy flux is lower during a storm except for a very sharp peak at local noon.

Table 2.1: Space environment fits

	n_E (cm^{-3}	T_E (keV)	n_I (cm^{-3}	T_I (keV)
NASA worst case	1.1	12	0.24	29.5
ATS - 6	1.2, 1.2	16, 1	0.24, 0.00882	29.5, 0.111
Sept. 4	0.3, 0.2	4,7	0.3, 0.2	4,7

In Fig. 2.3, the electron and ion flux is compared to the single and Bi-Maxwellian fits used by NASCAP-2k [102] and shown in Tab. 2.1. Fig. 2.3a shows the electron flux predicted by the three Maxwellian models alongside two traces from the empirical model - the upper one is chosen as a harsh charging condition ($K_P = 8$, $LT = 6$) and the lower one as a mild condition ($K_P = 2-$, $LT = 18$). The empirical model predicts significantly higher flux at low energies (which may be due to photoelectrons), similar flux at medium energies depending on the K_P and LT, and lower flux at higher energies above 10 keV than the Maxwellian fits.

For aluminum assuming isotropic electron flux, any flux between 120 eV and 6 keV produces more than one secondary electron and contributes to positive charging rather than negative charging. This "positive zone" is greyed out in the plot and sees more flux relative to the high energy zone above 6 keV in the empirical model than the Maxwellian models, which has implications for the net yields.

The empirical ion flux is compared to the same Maxwellian fits shown in Tab. 2.1 in Fig. 2.3b. The empirical trace with the large low energy spike corresponds to $K_P = 8$, $LT = 13$ and the other

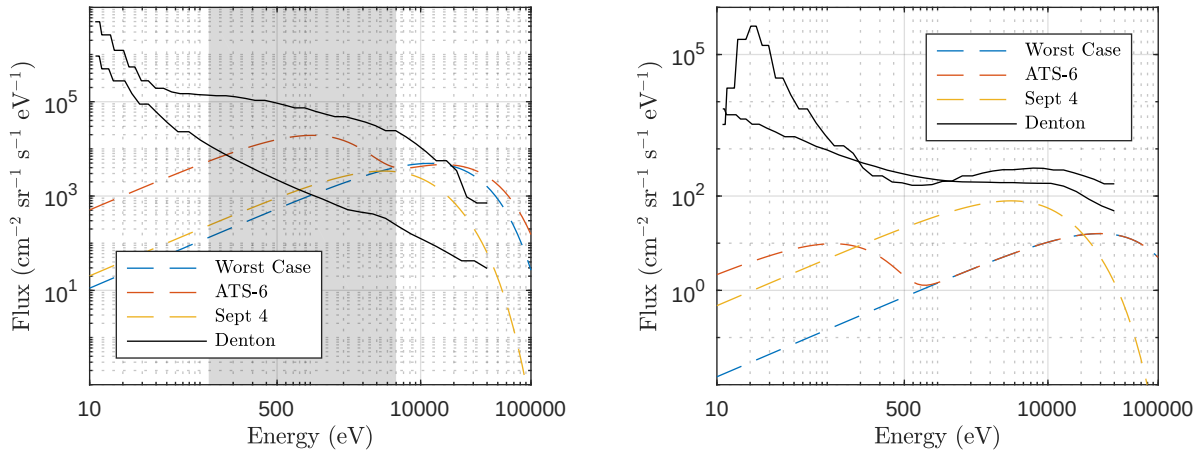

(a) Electron comparisons

(b) Ion comparisons

Figure 2.3: Differential ion and electron fluxes at GEO as well as commonly used Maxwellian fits

to K_P = 2-, LT = 2. The empirical model predicts more flux everywhere than the Maxwellian models, especially at low energies. Additionally, the calm fluxes are much more flat in the empirical model. In the storm condition at local noon, there are two very distinct populations predicted by the empirical model, one with energy near 50 eV, and the other is much more spread out with an energy range of 1-20 keV.

A fundamental property of a Maxwellian fit when plotted on a log-log scale is it's shape - It is always a hump with a shallow slope at low energies and steep slope at high energies. Changing the density moves it up and down, and changing the temperature moves it left and right, but neither of these properties change its width. Adding multiple Maxwellian populations with similar energy can approximate a wider peak, but there is no way to produce a narrow peak as is seen in the empirical storm flux at LT = 13 using Maxwellian distributions.

2.2 Spacecraft Charging

The environmental electron and ion flux that impacts a spacecraft can charge a spacecraft as well as cause SEE. These plasma currents add to the photoelectric current and any electron or ion beams to change the charge on a spacecraft. Each of the major currents are detailed below.

2.2.1 Electron and Ion Thermal Currents

Electrons and ions impact the spacecraft, electrons causing a negative current and ions absorbing an electron to neutralize themselves and causing a positive current. For a flux distribution over energy $F(E)$, the current is

$$I(\phi) = q_0 2\pi A \int_L^\infty \left(\frac{E}{E \pm \phi}\right) F(E \pm \phi) dE \tag{2.2}$$

where q is the particle charge, A is the effective area exposed to the plasma, and ϕ is the spacecraft potential. The lower bound of the integral L is 0 for the repelled particle, and $|\phi|$ for the attracted particle. Ions take the upper sign and electrons take the lower.

2.2.1.1 Maxwellian Distributions

At equilibrium all plasmas should theoretically have a Maxwellian distribution of speed. The resulting differential flux from this distribution is given by

$$F(E) = n\sqrt{\frac{q_0}{2\pi m kT}} \frac{E}{kT} e^{\frac{-E}{kT}} \tag{2.3}$$

where q_0 is the fundamental charge (a positive number), n is the density of the plasma, m is the particle mass, and kT is the thermal energy of the plasma in units of eV. The factor of q_0 is used for dimensional purposes so that kT can be used in eV rather than Joules. Typical Maxwellian parameters for GEO are given in Tab. 2.1 and are shown graphically in Fig. 2.3. If this distribution is used in the current integral in Eq. (2.2), the following elegant analytic expressions are found:

$$I(\phi) = \begin{cases} I_0(1 - \frac{q_0\phi}{kT}) & \text{Attracted} \\ I_0 e^{-q_0\phi/kT} & \text{Repulsed} \end{cases} \tag{2.4}$$

where I_0 is the current that the object draws with no voltage. This is given by

$$I_0 = \frac{1}{4} n q_0 \sqrt{\frac{8kTq_0}{\pi m}} \tag{2.5}$$

Once again the factor of q_0 is included to convert kT from eV to Joules. These simple formulas predict a linear increase in current with voltage for the attracted particle and an exponential decay in current from the repulsed particle.

2.2.1.2 Empirical Flux

Although Maxwellian distributions are popular and easy to use, they do not always fit the observed data well, as shown in Sec. 2.1. If measured flux distributions are used, these integrals are done numerically using an adaptive quadrature integration program that uses linear interpolation on the flux data. The flux data is logarithmically spaced in 40 increments for $K_P = 2$- and 50 increments for $K_P = 8$ as shown in Figs. 2.2a and 2.2b. The lower bound for the attracted particle is $|\phi| + 0.1$ V to avoid a mathematical singularity, and since data for $F(E)$ only exists up to 40 keV for the distributions used, the upper bound is taken as $40,000 \text{ V} + \phi$. To counteract some of the enrichment of the low energy electron flux by photoelectrons and secondary electrons created on the spacecraft, the electron flux at all energies lower than 50 eV is reassigned to the flux at 50 eV.

2.2.2 Secondary Electron Emission

When an electron or ion impacts a material, it deposits much of its energy in the first few nanometers of the material. Some of this energy goes into freeing electrons near the surface which can escape the material. This phenomena is referred to as Secondary Electron Emission (SEE) and can significantly reduce the net electron thermal current and amplify the ion thermal current. Additionally, there is a chance that an electron bounces off the material rather than sticking. This phenomena is called "backscatter". The probability that an electron backscatters is given by η, the expected number of secondary electrons generated by a single incident electron is typically given by δ, and the total yield as $Y = \eta + \delta$. Since the total yield is a function of energy, it must be integrated over the distribution to find the current:

$$I(\phi) = q_0 2\pi A \int_L^\infty Y(E)\left(\frac{E}{E \pm \phi}\right) F(E \pm \phi) dE \tag{2.6}$$

Rather than calculating the actual current, the mean yield $< Y >$ is typically used which is total ratio of the outgoing secondary electrons to incoming electrons for a particular distribution.

$$< Y >= \frac{I_Y}{I} = \frac{\int_L^\infty Y(E)\left(\frac{E}{E\pm\phi}\right)F(E\pm\phi)dE}{\int_L^\infty \left(\frac{E}{E\pm\phi}\right)F(E\pm\phi)dE} \tag{2.7}$$

The mean yield is a function of the distribution and the spacecraft voltage ϕ which shifts the distribution. Even if Maxwellian distributions are used, this integral must be done numerically using the same adaptive quadrature integration program. The SEE function δ for both ion and electron impact as well as the backscattering function η are discussed next.

2.2.2.1 Electron-Induced SEE

The electron-induced SEE yield is typically small at low landing energies, then it rises to a large value for intermediate energies around a few hundred eV, then falls back to a small yield for keV energies. There have been numerous different models for SEE, and considerable tuning in those models. The NASCAP-2k model [101] for electron-generated SEE as a function of landing energy (E) and angle (ψ) is used with $\psi = 0°$ for the electron beam and a modification [104] to account for isotropic flux (δ_I) for the environmental currents:

$$\delta(E,\psi) = C\frac{1 - e^{-R\alpha\cos(\psi)}\sec(\psi)}{\alpha(b_1 q_1 E^{q_1-1} + b_2 q_2 E^{q_2-1})} \tag{2.8}$$

$$\delta_I(E) = 2CE\frac{R\alpha - 1 + e^{-R\alpha}}{(R\alpha)^2} \tag{2.9}$$

where $R = b_1 E^{q_1} + b_2 E^{q_2}$ is the range of the electrons in the material. For Aluminum $b_1 = 154$ Å, $b_2 = 220$ Å, $q_1 = 0.8$, and $q_2 = 1.76$, assuming the landing energy E is in keV. The parameters C and α are hand tuned to $C = 9.9808, \alpha = 3.0486e8$ in order to match the peak yield and energy (for incident flux) of 0.97 and 400 eV.

2.2.2.2 Ion-Induced SEE

Ions may also cause SEE, and for many materials the number of secondaries caused by ions is much larger than that caused by electrons. In this analysis the two parameter Nascap-2k model

[101] for isotropic flux is used:

$$\delta(E) = 2\frac{\beta E^{1/2}}{1 + E/E_M} \tag{2.10}$$

Where E is the energy in keV, and for aluminum $\beta = 1.36$ and $E_M = 40$ are fitting parameters. To get the mean yield, this function must be integrated alongside the ion flux as shown in Eq. (2.7).

2.2.3 Electron Backscattering

Backscattering occurs when an electron is reflected from the spacecraft rather than absorbed. Once again there are numerous models for this phenomena but the only one presented here is the NASCAP-2k model for energy-dependent backscattering [101]. First the albedo for normal (A_N) and isotropic (A_I) flux are calculated:

$$A_N = 1 - (2/e)^{0.037Z} \tag{2.11}$$

$$A_I = 2\frac{1 - \eta_0(1 - \log(\eta_0))}{\log(\eta_0)^2} \tag{2.12}$$

and then either are multiplied by a string of Heaviside step functions that account for low energy cases

$$\eta(E) = \left(\frac{H(1-E)H(E-0.05)\log(\frac{E}{0.05})}{\log(20)} + H(E-1)\right)\left(\frac{e^{-E/5}}{10} + A\right) \tag{2.13}$$

Where E is the landing energy in keV, $H(x)$ is the Heaviside step function, log is the logarithm with base 10, and Z is the atomic number of the material (aluminum in this analysis). The formulas above can be added to produce the total yield $Y(E) = \eta(E) + \delta(E)$ for monoenergitic electrons.

2.2.4 Mean Yields

Putting all of this together, the mean yield $< Y >$ is shown in Fig. 2.4 as a function of local time using the empirical model for flux as well as the three chosen Maxwellian fits for a spacecraft at 0 V.

The yields computed using Denton's model for flux are much higher than those from the Maxwellian distributions - this is due to the difference in flux in the "positive zone" from 120 eV

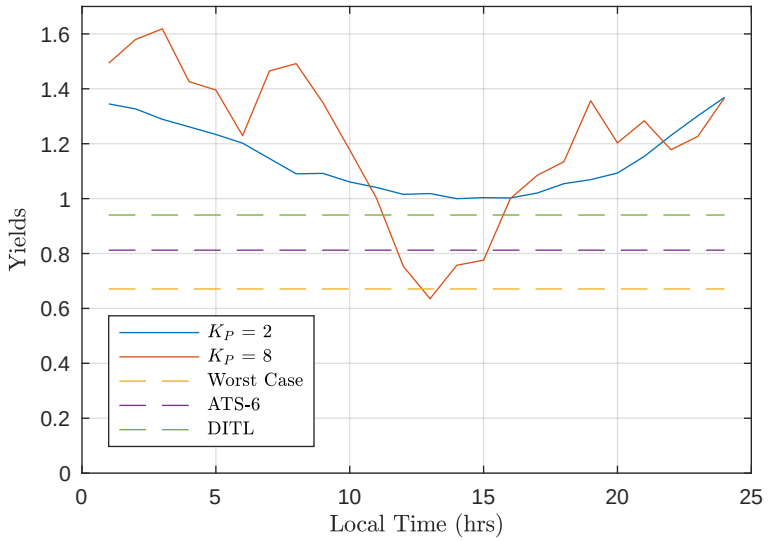

Figure 2.4: Mean yields to an uncharged spacecraft using various environmental models

and 6 keV shown in Fig. 2.3. As a function of local time, the yield in both storm conditions dips below 1 for a new hours near local noon at $K_P = 8$. In all other conditions, the yield is larger than one, which means that the net electron current is positive and a spacecraft cannot charge negative no matter how much flux there is.

In Reference [105], Ferguson et al. propose that flux above 9 keV is the best proxy for charging, adding that charging will often occur if there is more than 4e8 electrons/cm^2/s above 9 keV. The empirical model predicts flux higher than this threshold when $K_P = 8$ at local times of 6 and 22 (12e8 and 11e8 electrons/cm^2/s of flux, respectively), but the isotropic aluminum yields for both of these instances are above 1, which prohibits any charging. This disagreement between the two models could be for many reasons. It is possible that averaging the flux misses some subtleties that affect the charging. For instance, a very hot but tenuous population one day and a very dense but cold population the next day will average to a flatter population and predict no charging on average, even though on the first day there would definitely have been charging.

To investigate the voltage dependency of the mean yields, the above formulas for SEE and backscattering are inserted into Eq. (2.7) to calculate $< Y >$ for electrons and ions as a function

of both space weather and local time for both space weather conditions using the empirical flux model. This is shown in Figs. 2.5a and 2.5b.

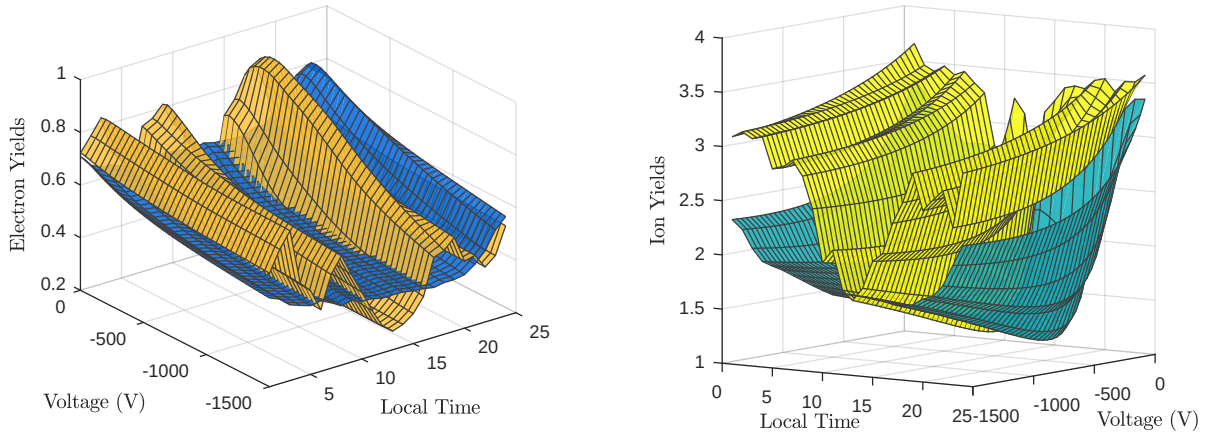

(a) Electron-Induced yields for $K_P = 8$ (orange), $K_P = 2$ (blue) as a function of Local Time and voltage

(b) Ion-Induced yields for $K_P = 2$ (teal), $K_P = 8$ (yellow) as a function of Local Time and voltage

Figure 2.5: Electron and Ion yields for aluminum

Fig. 2.5a shows the electron yields for stormy and calm space weather conditions. The effective yield is zero for a positive craft since although secondaries are generated, they are re-collected by the craft. The yield is always less than 1, but it gets very close for low voltages where there are still a lot of low energy particles. The dependence on local time is much more dramatic during the storm, which matches the higher dependence for the flux. At local noon, the storm yields are lowest, which matches the depleted low energy section of the flux. Although the local time dependence for the flux is low in the morning and afternoon/night sectors in the flux, the yields have high dependence there.

Fig. 2.5b shows the ion yields, which are much higher than the electron yields, although since the incident ion flues are much lower this current is smaller than the electron-induced yields. There is a huge dip around local noon for the storm case, just as with the electron yields. Since the peak for ion-induced SEE is at much higher energies in the keV range, this matches the increase in low energy ions and decrease in high energy ions observed around local noon.

2.2.5 Photoelectric Current

Energy from the sun can energize electrons in the first few nanometers of the spacecraft so that they leave the surface. The fraction that have enough energy to escape the potential well of the spacecraft cause a net positive current given by [70]:

$$I_p = \begin{cases} j_{\text{ph}} A e^{-q\phi/k_{\text{B}}T_{\text{ph}}} & \phi > 0 \\ j_{\text{ph}} A & \phi \leq 0 \end{cases} \tag{2.14}$$

Where j_{ph} is the photoelectron flux, A is the cross-sectional area, and $k_{\text{B}}T_{\text{ph}}$ is the thermal energy of the ejected photoelectrons. For aluminum, $k_{\text{B}}T_{\text{ph}} = 2$ eV and $j_{\text{ph}} = 40\ \mu\text{A/m}^2$. For a negative spacecraft this current is constant, it quickly vanishes with increasing surface potential.

2.2.6 Beam Current

The electron beam will only escape the potential well of the tug and cause any charging if it has sufficient energy. If it has enough energy to escape the well of the tug, but not to reach the debris, it will deflect and fly off into space and cause a net current on the tug but not the debris. Finally, if the beam is energetic enough it will reach the debris and cause a negative current. This is shown in Eq. (2.15) under the assumption that $\phi_T > 0$ and $\phi_D < 0$:

$$I_T = 0, I_D = 0 \qquad E < q_0\phi_T \tag{2.15}$$

$$I_T = I_{\text{beam}}, I_D = 0 \qquad q_0\phi_T < E < q_0(\phi_T - \phi_D) \tag{2.16}$$

$$I_T = I_{\text{beam}}, I_D = -I_{\text{beam}} \qquad E > q_0(\phi_T - \phi_D) \tag{2.17}$$

where I_T and I_D are the currents to the tug and debris, I_{beam} is the current that actually comes out of the electron gun, and E is the energy of the electron beam.

The yield for the electron beam is calculated assuming normal incidence and from the landing energy $LE = q_0(V_b - \phi_T + \phi_D)$ where V_b is the accelerating voltage of the beam, and ϕ_T and ϕ_D are the potentials of the tug and debris respectively. In reality, the debris may be rotating so the

angle of incidence will change as the angle between the beam and the debris surface changes, which will reduce the effectiveness of the beam.

2.3 Time-Varying Charging Solutions

In [96], a simpler charging model then the one presented above is developed and is used to propagate the charges of two neighboring spacecraft through time. The charging model uses Maxwellian models for the thermal currents, neglects SEE from incident ions, and uses a SEE model from [97] assuming normally incident electrons. Since the charging model is outdated it is not presented, but the high level results are. The historically curious reader is referred to the original paper.

The concept of pulsing the electron beam is investigated because it could offer higher forces for the same power as a continuous beam. Additionally, it opens windows of opportunity where measurements can be taken without interference of the electron beam. The physical explanation of the average pulsed force being higher than the continuous force for equal power is that the average pulsed force is decreased linearly by the duty cycle but increased quadratically. As an example consider two equal power beams applied in a vacuum, one continuous and one pulsed at a 50% duty cycle. Since the pulsed beam is only running half the time, it can draw twice the power in the time that it is on. If it uses this extra power to double the voltage, it can double the charge stored on each craft. Since the force is roughly proportional to the product of the two charges, it will increase by a factor of four while the beam is on, and decay to zero in other half of the time. This results in an average force that is more than twice the continuous force in this simple vacuum case. However, in a plasma the situation is more complex. The current required to achieve a potential is increased at higher voltages to offset the increased current from the plasma. Further, it takes some time for the large space objects to charge to their steady-state values. In contrast to the earlier continuous beam ET studies, the time-varying charging equations must be considered. The result is a complex set of competing conditions which are investigated in this section.

Since the currents directly change the charge of each craft, not the voltage, a mapping between

voltage and charge is needed. The voltage of each spacecraft is a function of its own charge and the charge of nearby spacecraft. Assuming two spherical spacecraft separated by ρ which is much larger than the debris and tug spacecraft radii $R_{\mathrm{D}}, R_{\mathrm{T}}$, the relation becomes [106]:

$$\begin{bmatrix} \phi_{\mathrm{T}} \\ \phi_{\mathrm{D}} \end{bmatrix} = \frac{1}{4\pi\epsilon_0} \begin{bmatrix} 1/R_{\mathrm{T}} & 1/\rho \\ 1/\rho & 1/R_{\mathrm{D}} \end{bmatrix} \begin{bmatrix} q_{\mathrm{T}} \\ q_{\mathrm{D}} \end{bmatrix} \tag{2.18}$$

Here ϕ_{T} and ϕ_{D} are the absolute potentials and $R_{\mathrm{T}}, R_{\mathrm{D}}$ are the effective radii of the tug and debris, respectively. This relationship is used at each time step to calculate the voltages which are then used to calculate the currents.

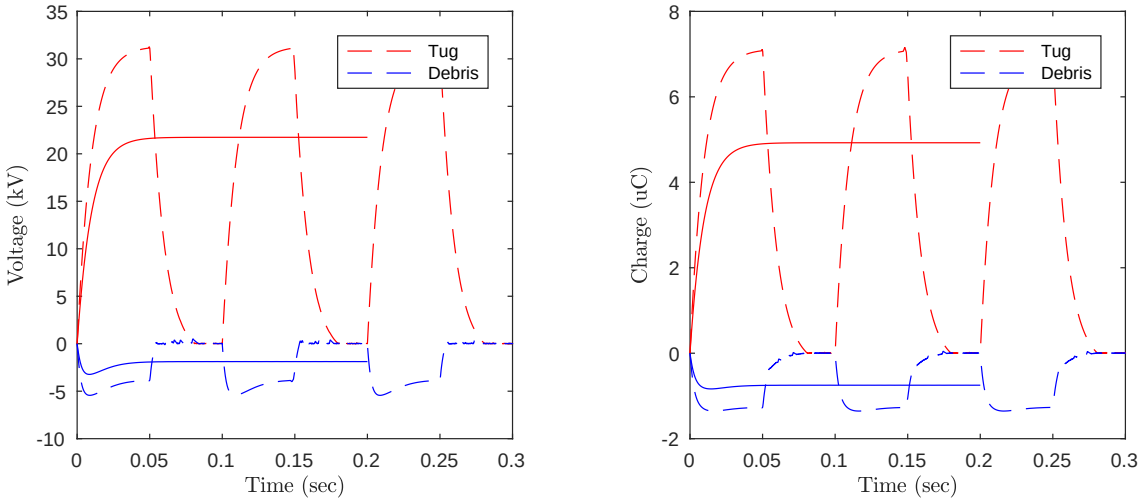

(a) Voltages (b) Charges

Figure 2.6: Voltage and charges for pulsed and continuous beams. The tug is red, the debris blue, and pulsed beams are dashed lines while continuous beams are continuous lines

A numerical simulation is developed to find the currents as a function of both the spacecraft charge levels and time. This is used to propagate the charge on the tug and debris spacecraft $[q_{\mathrm{T}}, q_{\mathrm{D}}]^T$ through time using an RK4 integrator. This is shown explicitly below:

$$\begin{bmatrix} \dot{q}_{\mathrm{T}} \\ \dot{q}_{\mathrm{D}} \end{bmatrix} = \begin{bmatrix} \sum I_{\mathrm{T}}(\phi_{\mathrm{T}}, t) \\ \sum I_{\mathrm{D}}(\phi_{\mathrm{D}}, t) \end{bmatrix} \tag{2.19}$$

Auxiliary variables of $\boldsymbol{\phi}(t) = [\phi_T(t), \phi_D(t)]^T$ and $F(t)$ are also recorded. An example case [107] is run with an absolute tolerance of 10^{-9} corresponding to 1 nC, and a relative tolerance of 10^{-3}

corresponding to about 3 significant figures. The timespan of integration is 0.2 seconds for the continuous cases, and 3 pulse periods for the pulsed cases. The charge, voltage, and force history are computed for an example pulsed and continuous case with $V_B = 23.9$ kV and $I_B = 536\mu$A for the continuous case, and $d = 0.5, V_B = 42.25$ kV, and $I_B = 758\mu$A for the pulsed case. Both of these sets have an average power of 16 Watts.

The voltage and charge history are shown for pulsed and continuous cases in Fig. 2.6. The continuous cases have continuous lines while the pulsed have dashed lines. The tug is red and the debris is blue in all the voltage and charge plots. When the beam is on, the pulsed voltage, charges, and force are all higher than the continuous beam, but once the beam turns off all of these decay to zero. Since the force is proportional to the product of the charges, its increase during the time the beam is on outweighs the decrease in the average force during the time the beam is off. In this example the pulsed force (not shown) is 8% higher.

2.4 Equilibrium Charging Solutions

For many charging scenarios, the environment changes slowly enough that the spacecraft can always be assumed to be at the equilibrium solution. Referencing Fig. 2.6, the spacecraft reaches its equilibrium in a few 10s of milliseconds. As long as the currents change slower than that, the spacecraft can be assumed to be at the equilibrium solution without introducing large errors. If the pulse period of the electron beam is increased to 100s of ms or longer, the pulsed ET can be analyzed using only the equilibrium voltages. If the electron beam is removed, this process can also be used to analyze environmental charging of debris.

2.4.1 Electrostatic Tractor Equilibrium Charging

The current balance equation (Eq. (2.1)) is solved for different local times and different net beam current densities using the empirical flux model. The beam current density is computed as the actual beam current (which would actually be directed in a small spot) divided by the total surface area of the spacecraft. For the debris, this current must be reduced using the yield. The

photoelectric current is only applied on 1/4 of the total surface area, since the cross sectional area of a sphere is 1/4 the total area. This normalization allows the spacecraft charging calculations to be done once and then interpolated to cover a wide variety of cases. These voltages are shown in Fig. 2.7.

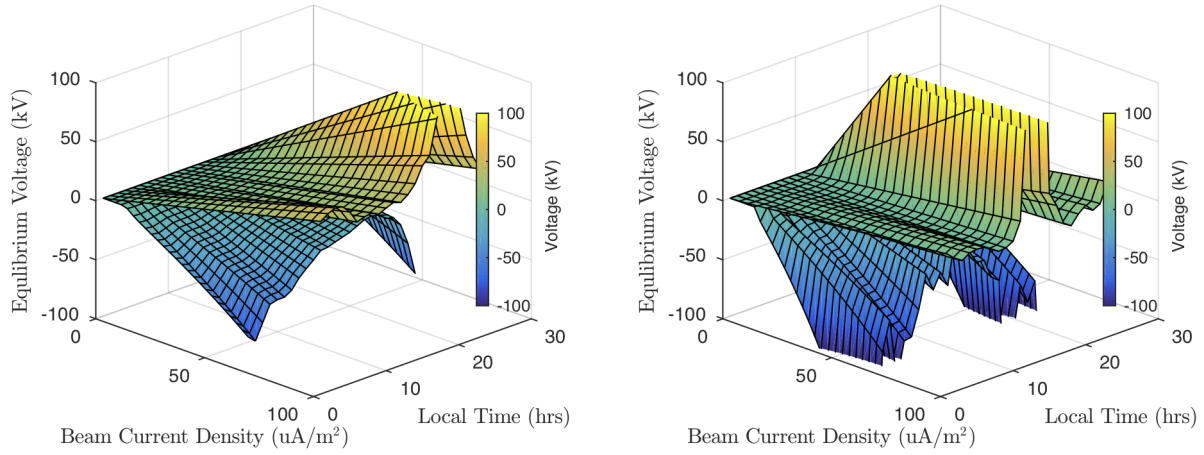

(a) $K_P = 2-$ (b) $K_P = 8$

Figure 2.7: Equilibrium voltages for tug (top sheet) and debris (bottom sheet) at different local times and beam currents

Figure 2.7a shows the equilibrium voltage at $K_P = 2-$ computed using the empirical model. The upper sheet represents the tug for which the beam is a positive net current, and the lower sheet represents the debris for which the beam is negative. The most obvious trend is that it takes less beam current to charge negative than positive. Next, at low beam currents it is very hard to charge negative. This is because the photoelectron current very effectively resists any negative charging until it is overwhelmed by the beam. It is easiest for the tug to charge positive in the late night sector, and easiest for the debris to charge negative near local midnight.

Figure 2.7b shows the tug and debris equilibrium voltages in the same format, but for $K_P = 8$. There is a lot more variation over local time during a storm - the tug can charge positive very easily near local noon and has a difficult time everywhere else. The debris has a much more complex trend across local time, but it experiences both more and less charging than the calm case at different

local times.

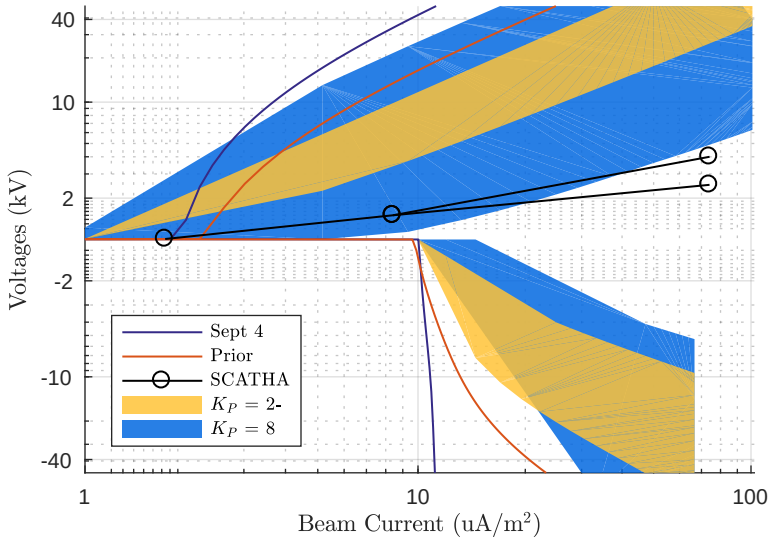

Figure 2.8: Equilibrium voltage comparison

Figure 2.8 compares the equilibrium voltage found the empirical model with that from using the Sept. 4 Bi-Maxwellian fit, a single Maxwellian fit used in prior charging analysis of the ET, and the SCATHA data. The empirical voltages are shown as colored blocks that encompass the curves at all local times with yellow and blue representing the calm and stormy condition. The increased variation over local time at $K_P = 8$ can clearly be seen in this format. The Sept. 4 model uses the Bi-Maxwellian fit presented in Tab. 2.1 and predicts more positive charging than the empirical model at either storm condition at high currents. It also predicts a much more negative voltages for the debris once the current overpowers the photoelectron current (10 μA/m^2 = $j_{\text{ph}}/4$). This is because the ion populations are very hot which reduces the ion current significantly. The fit from prior work uses the parameters from Hogan and Schaub [74] and due to the much lower ion temperature it predicts a less extreme voltage for the debris past the photoelectric cutoff. The SCATHA data is taken from [108] where the spacecraft emitted a electron beam and charged itself up to 3 keV. Since the charging was often limited by the energy of the beam, the spacecraft voltage at that beam current might be even higher if the beam energy was increased. The surface area of

SCATHA, if approximated by a cylinder, is 13.5 m^2 [109]. SCATHA is made from many different materials with different SEE parameters and is also spinning which changes the sunlit area as a function of time, thus, these data points are provided more as an order of magnitude estimate.

The charging models based on Maxwellian flux, empirical flux, and the SCATHA data all have sources of error. For the purposes of the ET, which takes a few months to tow a debris object out of GEO, the empirical flux data changing model is used because it provides a better estimate of the average space weather that would be encountered on such a multi-month trip. It is worth noting that all three classes of models predict similar trends in performance.

2.4.2 Debris Equilibrium Charging

For the case of a thin and rigid piece of torn MLI, the photoelectric current will be attitude dependent since it will not always present the same area to the sun. This effect is captured by adding a cosine term to the earlier equation:

$$I_p = \begin{cases} j_{\text{ph}} A \cos(\theta) e^{-q\phi/k_{\text{B}}T_{\text{ph}}} & \phi > 0 \\ j_{\text{ph}} A \cos(\theta) & \phi \leq 0 \end{cases} \tag{2.20}$$

where θ is the angle of incidence.

Equation (2.1) can be solved at each local time and each sun facing angle θ to provide a look-up table to interpolate and determine the voltage of both plates at any point in the orbit. Assuming the voltage to always be at the equilibrium value is justified since the charging time is very short compared to the orbit time.

Figure 2.9a shows the equilibrium voltage for aluminum as a function of local time and sun incidence angle. An angle of 90 or greater indicates that the object is shaded, and has no photoelectric current. Most of the charging happens in the absence of sunlight, and in the early morning sector when LT is between 0 and 6. This matches intuition as high energy electrons cluster in that region due to their drifts. The most negative voltage occurs when the spacecraft is entirely shaded and at a local time of 5, and is -170 V. For $\theta < 88°$, the voltage varies between 5 and 10 V

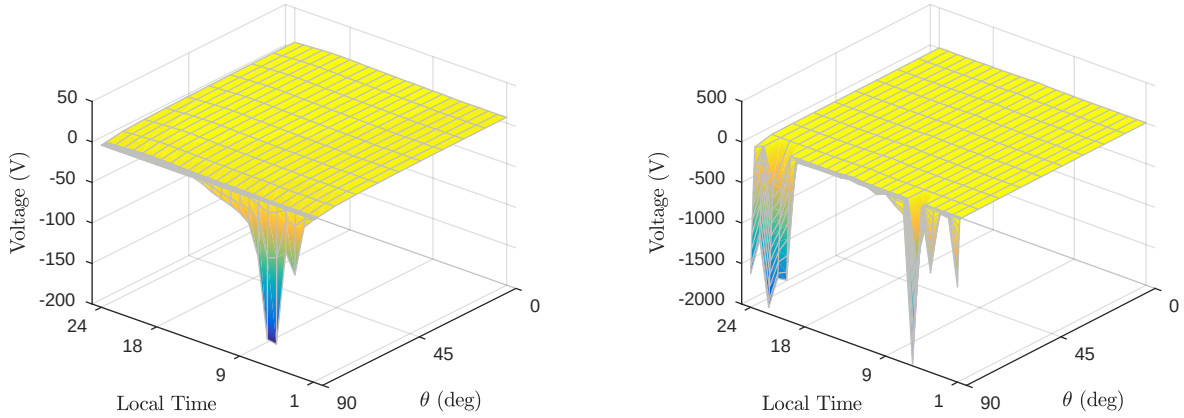

(a) Equilibrium voltage at $K_P = 2-$

(b) Equilibrium voltage at $K_P = 8$

Figure 2.9: Equilibrium voltage as a function of sun incidence angle and local time

positive as expected for a sunlit object in calm space weather.

Figure 2.9b shows the equilibrium voltage in the same format as Fig. 2.9a but for the stormy condition of $K_P = 8$. Again, most of the charging occurs for shaded or almost shaded angles, although the minimum angle moves down by a few tenths of a degree. The charging occurs in the early morning sector, but also very dramatically in the late night sector where LT is between 20 and 24. This may be linked to pre-midnight charging in the auroral region [**?**]. The charge levels are much lower here as well, dropping to -1.9 kV at LT = 6 and -1.8 kV at LT = 22. Additionally, the voltage stays below -1 kV for the entire sector between LT = 20 and 24. There is good intuition for the existence of high charging in the early morning sector due to the electron drift, but the strong charging in the late night sector is unexpected.

Even at this high K_P index, there is still not enough flux in the high-energy region where the yield is low to cause very severe charging. Once again, the fully sunlit voltages range between 5 and 10 V positive. Each sheet is assigned the voltage corresponding to the LT, and its sun angle θ since the plates are not electrically connected. This means that one plate is always shaded while the other is always sunlit.

These results for voltage must be taken with a grain of salt as they depend on a number

of parameters. Firstly, the photoemission for aluminum is chosen as the round number of 40 $\mu A/m^2$ to match that used by Nascap-2k. Second and most importantly, the model parameters for electron-induced SEE have a good amount of variability. The max yield used here of 0.97 and in Nascap-2k is reported as 2.0 by [97] and found experimentally to be near 2.5 by [110]. Additionally, Balcon et al. found that the SEE parameters had strong dependence on the angle of incidence (an electron that has grazing incidence creates more secondaries since it deposits more energy close to the surface where the secondaries have a better chance or escaping). There is also dependance on the surface condition (smooth or rough) and the temperature of the sample. This work also only considers normally incident flux.

If a maximum yield of of 2.0 is used, the voltages range from 0 to 17 V positive even in shade. This is because the net electron yield is greater than 1, and the instant the spacecraft starts to charge negative the SEE current turns on and pushes it back to positive since the secondary electrons can now escape the system.

2.5 Spacecraft Charging Conclusions

This chapter answers the first of the three questions: How do spacecraft charge? A space object is subject to many currents from the space plasma and the sun. The main currents are the thermal electron and ion currents, secondary electron emission from both electrons and ions, electron backscattering, the photoelectric current, and possibly the beam current. All these currents add together to change the charge of the spacecraft, which changes the voltage, which in turn changes the currents. This Ordinary Differential Equation (ODE) can be solved for a time varying voltage or an equilibrium voltage.

The time varying voltage is needed when the currents change on the order of 10s of milliseconds or faster, and the equilibrium voltage is sufficient if the changes are slower then that. Solutions are presented for both time varying and equilibrium voltages.

Chapter 3

Electrostatic Force and Torque estimation

This chapter assumes knowledge of the voltages and answers the question, "what are the forces and torques due to this charging?". This chapter is structured by first discussing plasma shielding at GEO, then discussing analytic force and torque expressions, and then moving to numerical solutions. The numerical solutions are divided into Method of Moments inspired models with lots of spheres and Volume MSM models for spacecraft with both conducting and dielectric parts.

3.1 Plasma Shielding

A charged object in a plasma will develop a sheath around it. This sheath contains oppositely charged particles and reduces the E field surrounding the charged object or the force between two charged objects. In all presented work, this effect is ignored and the Coulomb force law is used:

$$F = \frac{Q_T Q_D}{4\pi\epsilon_0 \rho^2} \tag{3.1}$$

Prior work [78] has shown that the effect of plasma shielding is very small, typically less than 1%, for the small separations considered. However, on rare occasions very dense plasma can make its way into GEO in the afternoon sector [111] and this would introduce significant shielding and make charging much more difficult.

3.2 Appropriate Fidelity Measures

Analytical formula for the electrostatic two-body problem are found for the special case of two conducting spheres using the Method of Images [80, 112, 113]. If the bodies are not spherical,

the multipole expansion method can be used to find the electric potential in the vicinity of a charge distribution by expanding the charge distribution in powers of $1/R$ [80]. The potential energy of two charged molecules can also be found and differentiated with respect to position attitude to find force and torque [114]. These expansions use terms similar to the inertia integrals for gravity used by Hou [115]. The conference paper cited in Reference [116] introduces a similar method for finding the electrostatic force and torque between two charged spacecraft, but differs in that it does not find the potential but finds the force and torque directly. This method for predicting force and torque is called the Appropriate Fidelity Measures (AFM) method, named for the measures of the charge distribution that appear due to the appropriate fidelity truncation of the binomial series.

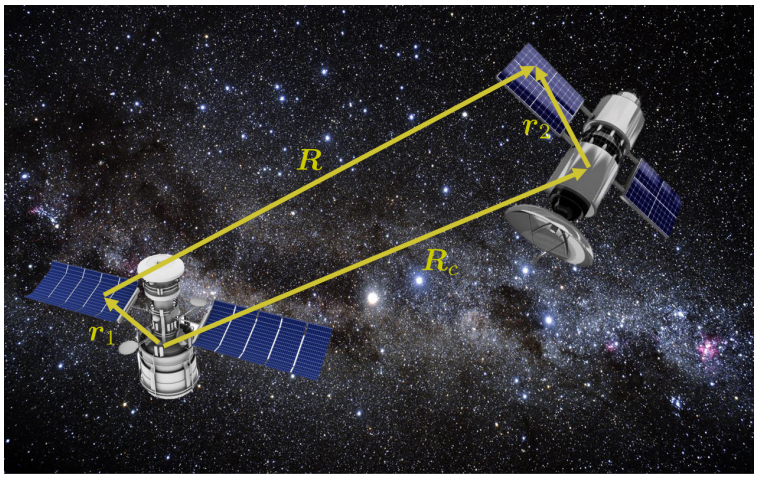

Figure 3.1: Coordinate system for inter-craft derivation

Consider two charged, conducting neighboring spacecraft as is shown in Figure 3.1 with a known charge distribution. They each experience a force and torque due to the other's charge. The force and torque on body 2 is found by integrating the differential force, which is a function of body 1's charge distribution, across body 2.

$$\mathrm{d}\boldsymbol{F}_2 = \frac{\mathrm{d}q_1 \mathrm{d}q_2 \boldsymbol{R}}{4\pi\epsilon_0 R^3} \tag{3.2}$$

where $\boldsymbol{R}$ points from $\mathrm{d}q_1$ to $\mathrm{d}q_2$. The separation vector is expressed from body vectors and a vector between the center of mass of each body $\boldsymbol{R} = \boldsymbol{R}_c + \boldsymbol{r}_2 - \boldsymbol{r}_1$. Using this substitution makes the

differential force

$$\mathrm{d}\boldsymbol{F}_2 = \frac{\mathrm{d}q_1\ \mathrm{d}q_2\ \boldsymbol{R}_c + \boldsymbol{r}_2 - \boldsymbol{r}_1}{4\pi\epsilon_0\ ||\boldsymbol{R}_c + \boldsymbol{r}_2 - \boldsymbol{r}_1||^3} \tag{3.3}$$

Where ϵ_0 is the permittivity of free space, $\epsilon_0 \approx 8.854187 * 10^{-12}$ F/m. The differential force is approximated by binomially expanding the denominator and truncating higher-order terms on the assumption that the body radii ($\boldsymbol{r}_1$ and $\boldsymbol{r}_2$) are small compared to their separation ($\boldsymbol{R}_c$).

$$\frac{1}{||\boldsymbol{R}_c + \boldsymbol{r}_2 - \boldsymbol{r}_1||^3} = (R_c^2 + r_1^2 + r_2^2 + 2(\boldsymbol{R}_c \cdot \boldsymbol{r}_2 - \boldsymbol{R}_c \cdot \boldsymbol{r}_1 - \boldsymbol{r}_2 \cdot \boldsymbol{r}_1))^{-3/2} \tag{3.4}$$

$$= \frac{1}{R_c^3}\left[1 + \left(\frac{r_2^2}{R_c^2} + \frac{r_1^2}{R_c^2} + \frac{2}{R_c^2}(\boldsymbol{R}_c \cdot \boldsymbol{r}_2 - \boldsymbol{R}_c \cdot \boldsymbol{r}_1 - \boldsymbol{r}_2 \cdot \boldsymbol{r}_1)\right)\right]^{-3/2} \tag{3.5}$$

Expand the denominator to second order using a binomial series $(1+x)^{-3/2} \approx 1 - \frac{3}{2}x + \frac{15}{8}x^2$ and reassemble to approximate the differential force as:

$$\mathrm{d}\boldsymbol{F}_2 = \frac{\mathrm{d}q_1\ \mathrm{d}q_2}{4\pi\epsilon_0 R_c^3}(\boldsymbol{R}_c + \boldsymbol{r}_2 - \boldsymbol{r}_1)\left(1 - \frac{3r_1^2}{2R_c^2} - \frac{3r_2^2}{2R_c^2} - \frac{3(\boldsymbol{R}_c \cdot \boldsymbol{r}_2 - \boldsymbol{R}_c \cdot \boldsymbol{r}_1 - \boldsymbol{r}_2 \cdot \boldsymbol{r}_1)}{R_c^2} + \frac{15((\boldsymbol{R}_c \cdot \boldsymbol{r}_2)^2 + (\boldsymbol{R}_c \cdot \boldsymbol{r}_1)^2 - (\boldsymbol{R}_c \cdot \boldsymbol{r}_1)(\boldsymbol{R}_c \cdot \boldsymbol{r}_2))}{2R_c^4}\right) \tag{3.6}$$

This differential is integrated over the entire body to obtain the net electrostatic force on this object, or crossed with the body position vector and integrated over the body to obtain torque. Just as moments of the mass distribution play a key role in solving the gravitational two-body problem [115], moments of the charge distribution play a key role in predicting electrostatic force and torque. Three especially important moments of the charge distribution are identified and named here:

$$Q = \int_B \mathrm{d}q \qquad \boldsymbol{q} = \int_B \boldsymbol{r}\,\mathrm{d}q \qquad [Q] = \int_B -[\tilde{\boldsymbol{r}}][\tilde{\boldsymbol{r}}]\,\mathrm{d}q \tag{3.7}$$

Q is a scalar and is the total charge, $\boldsymbol{q}$ is a 3×1 vector and is defined as the dipole moment, and $[Q]$ is a 3×3 tensor defined as the charge tensor. The vector $\boldsymbol{r}$ points from the center of mass to the differential charge $\mathrm{d}q$, and $[\tilde{\boldsymbol{r}}]$ is the matrix form of the vector cross product: $\boldsymbol{a} \times \boldsymbol{b} = [\tilde{\boldsymbol{a}}]\boldsymbol{b}$. If the gravity analogy is used, the total charge Q is similar to the total mass, the dipole moment $\boldsymbol{q}$ is similar to the total mass multiplied by the offset between the center of a coordinate system and the true center of mass, and the charge tensor $[Q]$ is similar to the inertia tensor. The dipole

moment $\boldsymbol{q}$ provides a measure of where the center of charge is in relation to the center of mass. If $\boldsymbol{q}$ is zero, then the center of charge and mass locations are identical. To relate these AFM terms to the variables commonly used in multipole expansions, Q and $\boldsymbol{q}$ are the monopole and dipole terms, and the charge tensor $[Q]$ defined here is related to the quadrupole $[Q_p]$ by $[Q_p] = -3[Q] + 2\text{tr}([Q])$ [80].

The full derivation for force and torque is given in the appendix and is long. For brevity, only the results are presented here. The force on body 2 is given by

$$\begin{aligned}\boldsymbol{F}_2 = \frac{1}{4\pi\epsilon_0 R_c^3}\Bigg[&\Bigg(Q_1Q_2 + \frac{3Q_2}{2R_c^2}\text{tr}([Q_1]) + \frac{3Q_1}{2R_c^2}\text{tr}([Q_2]) - \frac{3Q_1}{R_c^2}\boldsymbol{R}_c\cdot\boldsymbol{q}_2 + \frac{3Q_2}{R_c^2}\boldsymbol{R}_c\cdot\boldsymbol{q}_1 + \frac{3Q_2}{R_c^2}\boldsymbol{q}_2\cdot\boldsymbol{q}_1 \\ &- \frac{15Q_1}{2R_c^4}\boldsymbol{R}_c^T[Q_2]\boldsymbol{R}_c - \frac{15Q_2}{2R_c^4}\boldsymbol{R}_c^T[Q_1]\boldsymbol{R}_c - \frac{15}{R_c^4}(\boldsymbol{R}_c\cdot\boldsymbol{q}_2)(\boldsymbol{R}_c\cdot\boldsymbol{q}_1)\Bigg)\boldsymbol{R}_c \\ &+ Q_1\boldsymbol{q}_2 + \frac{3Q_1}{R_c^2}[Q_2]\boldsymbol{R}_c + \frac{3(\boldsymbol{R}_c\cdot\boldsymbol{q}_1)}{R_c^2}\boldsymbol{q}_2 - Q_2\boldsymbol{q}_1 + \frac{3Q_2}{R_c^2}[Q_1]\boldsymbol{R}_c + \frac{3(\boldsymbol{R}_c\cdot\boldsymbol{q}_2)}{R_c^2}\boldsymbol{q}_1\Bigg] \end{aligned} \quad (3.8)$$

This equation is visualized in Table 3.1, where the common factor of $4\pi\epsilon_0 R_c^3$ is omitted, allowing easy ordering of terms based on which measures $(Q, \boldsymbol{q}, [Q])$ they incorporate. They are also ordered by the dimensionless ratio r/R_c where r is a characteristic dimension of either spacecraft. As the spacecraft move farther and farther away, the higher order terms in this variable matter less and less. The zeroth order term is in the upper left, the two boxes with two terms each are the first order terms, and the three boxes containing twelve terms along the diagonal are the second order terms. This table allows easy selection of the force terms needed for appropriate fidelity. As might be expected, the force expression is symmetric, if one changes the sign on all $\boldsymbol{R}_c$ terms and switches the subscripts the force on body 1 is found to be equal in magnitude but opposite in direction to the force on body 2. This satisfies Newton's 3$^{\text{rd}}$ law.

The torque is given by

$$\boldsymbol{T}_2 = \frac{1}{4\pi\epsilon_0 R_c^3}\left[Q_1\boldsymbol{q}_2\times\boldsymbol{R}_c + \frac{3(\boldsymbol{R}_c\cdot\boldsymbol{q}_1)\boldsymbol{q}_2\times\boldsymbol{R}_c}{R_c^2} - \frac{3Q_1\boldsymbol{R}_c\times[Q_2]\boldsymbol{R}_c}{R_c^2} + (\boldsymbol{q}_1\times\boldsymbol{q}_2)\right] \quad (3.9)$$

This equation is visualized in Table 3.2 which follows Table 3.1 in omitting the factor of $4\pi\epsilon_0 R_c^3$ and grouping terms by their order in the dimensionless ratio r/R_c. Terms closer to the upper left corner are lower order.

Table 3.1: Force ordering matrix

	Q_1	$\boldsymbol{q}_1$	$[Q_1]$
Q_2	$Q_1 Q_2 \boldsymbol{R}_c$	$\frac{3Q_2}{R_c^2}(\boldsymbol{R}_c \cdot \boldsymbol{q}_1)\boldsymbol{R}_c - Q_2\boldsymbol{q}_1$	$\frac{3Q_2}{2R_c^2}\mathrm{tr}([Q_1])\boldsymbol{R}_c$ $-\frac{15Q_2}{2R_c^4}(\boldsymbol{R}_c^T[Q_1]\boldsymbol{R}_c)\boldsymbol{R}_c$ $+\frac{3Q_2}{R_c^2}[Q_1]\boldsymbol{R}_c$
$\boldsymbol{q}_2$	$Q_1\boldsymbol{q}_2 - \frac{3Q_1}{R_c^2}(\boldsymbol{R}_c \cdot \boldsymbol{q}_2)\boldsymbol{R}_c$	$\frac{3}{R_c^2}(\boldsymbol{q}_2 \cdot \boldsymbol{q}_1)\boldsymbol{R}_c$ $-\frac{15}{R_c^4}(\boldsymbol{R}_c \cdot \boldsymbol{q}_2)(\boldsymbol{R}_c \cdot \boldsymbol{q}_1)\boldsymbol{R}_c$ $+\frac{3(\boldsymbol{R}_c \cdot \boldsymbol{q}_1)}{R_c^2}\boldsymbol{q}_2 + \frac{3(\boldsymbol{R}_c \cdot \boldsymbol{q}_2)}{R_c^2}\boldsymbol{q}_1$	
$[Q_2]$	$\frac{3Q_1}{2R_c^2}\mathrm{tr}([Q_2])\boldsymbol{R}_c$ $-\frac{15Q_1}{2R_c^4}(\boldsymbol{R}_c^T[Q_2]\boldsymbol{R}_c)\boldsymbol{R}_c$ $+\frac{3Q_1}{R_c^2}[Q_2]\boldsymbol{R}_c$		

As expected, there are no zeroth order terms, in fact there are no terms at all corresponding to the scalar charge Q_2. Unlike the force expansion, the torque is not symmetric, i.e. $\boldsymbol{T}_1 \neq -\boldsymbol{T}_2$. This is because the torque on body 1 and body 2 are not measured about the same point, but rather the center of mass of each body. If all torques are measured about the same point, such as the barycenter of the system, the torques are equal and opposite and cancel out and are not able to change the angular momentum of the system.

3.2.1 Flat Electrostatic Field Simplification

It is also of interest to calculate the force and torque on charged conducting bodies due to ambient flat electric and magnetic fields. The differential force on a differential charge moving at $\boldsymbol{v}$ subject to $\boldsymbol{E}$ and $\boldsymbol{B}$ fields is given in Reference [79] as:

$$\mathrm{d}\boldsymbol{F} = \mathrm{d}q(\boldsymbol{E} + \boldsymbol{v} \times \boldsymbol{B}) \tag{3.10}$$

This differential force only varies significantly across a body if it is rotating very quickly near the geostationary point. The velocity is the orbital velocity $\boldsymbol{v_o}$ plus the transport velocity: $\boldsymbol{\omega}_{\mathcal{B}/\mathcal{E}} \times \boldsymbol{r}$ [117], where $\boldsymbol{\omega}_{\mathcal{B}/\mathcal{E}}$ is the angular velocity between the satellite body frame $\mathcal{B}$ and the magnetic field frame $\mathcal{E}$. For a spacecraft with $r = 1$ m, $\omega_{\mathcal{B}/\mathcal{E}} = 1$ deg/sec, and an ECEF orbital velocity of 1

Table 3.2: Torque ordering matrix

	Q_1	$\boldsymbol{q}_1$	$[Q_1]$
Q_2			
$\boldsymbol{q}_2$	$Q_1\boldsymbol{q}_2 \times \boldsymbol{R}_c$	$\frac{3}{R_c^2}(\boldsymbol{R}_c \cdot \boldsymbol{q}_1)\boldsymbol{q}_2 \times \boldsymbol{R}_c + (\boldsymbol{q}_1 \times \boldsymbol{q}_2)$	
$[Q_2]$	$-\frac{3}{R_c^2}Q_1\boldsymbol{R}_c \times [Q_2]\boldsymbol{R}_c$		

km/sec, the ratio of the transport velocity to the orbital velocity will be less than 10^{-5}. In many scenarios the transport term can be dropped. The force is then:

$$\boldsymbol{F} = \int_B (\boldsymbol{E} + \boldsymbol{v}_o \times \boldsymbol{B})\mathrm{d}q = Q(\boldsymbol{E} + \boldsymbol{v}_o \times \boldsymbol{B}) \tag{3.11}$$

$$= Q\boldsymbol{A} \tag{3.12}$$

where $A = \boldsymbol{E} + \boldsymbol{v}_o \times \boldsymbol{B}$ is the total field. The torque is

$$\boldsymbol{L} = \int_B \boldsymbol{r} \times (\boldsymbol{E} + \boldsymbol{v}_o \times \boldsymbol{B})\mathrm{d}q = (\boldsymbol{E} + \boldsymbol{v}_o \times \boldsymbol{B}) \times \boldsymbol{q} \tag{3.13}$$

$$= \boldsymbol{q} \times \boldsymbol{A} \tag{3.14}$$

This is the exact answer for the torque on a pure dipole in a flat field [79, 118].

3.2.2 Susceptibilities of the Measures

The expansions for force and torque in the electrostatic two-body problem are useful formula. However, they rely on knowledge of the charge distribution on both bodies in order to perform the integrations and find the measures. Unlike the rigid gravitational two-body problem, these measures change as charge moves throughout the bodies. Recalculating the entire charge distribution for both bodies would be a very intensive process. Here, a method for predicting the measures from parameters that are much more feasible to measure in situ such as the voltage, attitude, and position of each craft is presented.

To do this, a matrix dependent on the relative position and attitude is used to translate the voltage of each craft into a representation of the charge distribution. From this distribution, the

measures are formed as functions of the voltage of each craft. There are many ways to make this matrix, including the Method of Moments or Boundary Element Method. A recent addition is the Multi-Sphere Method, which uses hand-tuned parameters for the size and locations of spheres which are constrained to be equipotential [67, 119].

MSM emerged as a way to predict the force and torque with high-enough fidelity to be useful, while also evaluating fast enough to be practical. MSM approximates the satellite as a collection of spheres with variable position and radii. The voltage of any sphere is a function of both its own charge and the charge on neighboring spheres. If these spheres are far enough away to be approximated as point charges, the voltage on the i^{th} sphere is given by: [79, 67, 119]

$$V_i = \frac{1}{4\pi\epsilon_0}\frac{q_i}{R_i} + \sum_{j=1,\, j\neq i}^{N} \frac{1}{4\pi\epsilon_0}\frac{q_j}{r_{i,j}} \tag{3.15}$$

Where q_i and R_i are the charge and radius of the i^{th} sphere, respectively, and $r_{i,\,j}$ is the distance between spheres i and j. If the voltages of each sphere are given by $\boldsymbol{V} = [V_1, V_2, ...V_N]^T$ and the charges are given by $\boldsymbol{Q} = [q_1, q_2, ...q_N]^T$, the relationship between the two is $\boldsymbol{V} = [S]\boldsymbol{Q}$ or $\boldsymbol{Q} = [C]\boldsymbol{V}$, where $[C]$ is the capacitance matrix and $[S]$ is the elastance matrix defined below [106]:

$$[S] = \frac{1}{4\pi\epsilon_0}\begin{bmatrix} 1/R_1 & 1/r_{1,2} & \cdots & 1/r_{1,N} \\ 1/r_{2,1} & 1/R_2 & \cdots & r_{2,N} \\ \vdots & \vdots & \ddots & \vdots \\ 1/r_{N,1} & 1/r_{N,2} & \cdots & 1/R_N \end{bmatrix} \tag{3.16}$$

Since the voltage is assumed known, the charge distribution is found by numerically solving the linear system. If two conductors with n_1 and n_2 spheres each are considered, the elastance matrix can be put into block form:

$$\begin{bmatrix} \boldsymbol{V}_1 \\ \boldsymbol{V}_2 \end{bmatrix} = \frac{1}{4\pi\epsilon_0}\begin{bmatrix} S_1 & S_M \\ S_M^T & S_2 \end{bmatrix}\begin{bmatrix} \boldsymbol{Q}_1 \\ \boldsymbol{Q}_2 \end{bmatrix} \tag{3.17}$$

Where the voltage and charge of each craft are separated. Note that the self elastance terms S_1 and S_2 are much larger than the mutual elastance terms S_M because the inter-sphere separations are

much smaller inside one body rather than between the two bodies. Additionally, the self elastance matrices contain the diagonal $1/R$ terms which are larger than the off-diagonal $1/r$ terms. As an example, consider a template box and panel spacecraft with an 8 meter boom made from 248 spheres and a 3×1 meter cylinder made from 138 spheres. The log of the elastance matrix for these two objects with a separation of 40 meters is shown in Figure 3.2.

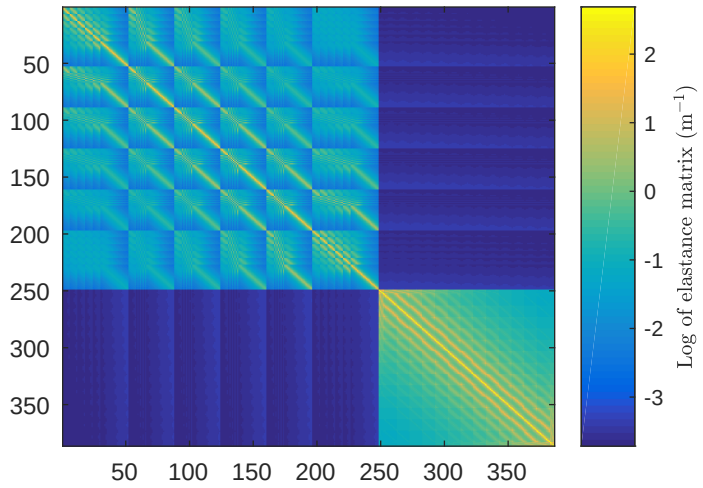

Figure 3.2: Log of elastance matrix

There are clearly four blocks, and the diagonals are $10^2 - 10^5$ times larger than the non-diagonal blocks. The blocky structure in the upper diagonal block comes from the method of assembly for the the box and panel spacecraft which is made from six rectangles. In general, the diagonal blocks will not change with relative position or attitude. The blocky structure, symmetry, and the time-fixed properties of the diagonal blocks are exploited when inverting using the Schur complement.

$$\begin{bmatrix} A & B \\ B^T & D \end{bmatrix}^{-1} = \begin{bmatrix} (A - BD^{-1}B^T)^{-1} & -A^{-1}B(D - B^TA^{-1}B)^{-1} \\ -D^{-1}B^T(A - BD^{-1}C)^{-1} & (D - B^TA^{-1}B)^{-1} \end{bmatrix} \tag{3.18}$$

Recognizing that A and D represent the self capacitance matrices, which contain much larger terms

than the mutual matrix B, terms second order in B are dropped:

$$\begin{bmatrix} A & B \\ B^T & D \end{bmatrix}^{-1} \approx \begin{bmatrix} A^{-1} & -A^{-1}BD^{-1} \\ -D^{-1}B^TA^{-1} & D^{-1} \end{bmatrix} = \begin{bmatrix} C_1 & -C_1S_MC_2 \\ -C_2S_M^TC_1 & C_2 \end{bmatrix} \tag{3.19}$$

Where $[C_i] = [S_i]^{-1}$ for all blocks. The two matrices C_1 and C_2 are not functions of the relative separation and orientation, which means they will be constant in time. The terms in S_M are of the form $1/||\boldsymbol{R}_c + \boldsymbol{r}_{2_i} - \boldsymbol{r}_{1_j}||$. Since the center to center separation R_c is much greater than the dimensions of either craft r_1 or r_2, this is approximated as

$$[S_M]_{i,j} = \frac{1}{||\boldsymbol{R}_c + \boldsymbol{r}_{2_i} - \boldsymbol{r}_{1_j}||} \sim \frac{1}{R_c} \tag{3.20}$$

Approximating all elements in the mutual capacitance matrix as $1/R_c$ ignores the relative attitude while still capturing some first-order mutual capacitance and susceptibility. The elastance matrix is now approximately inverted as

$$\begin{bmatrix} \boldsymbol{Q}_1 \\ \boldsymbol{Q}_2 \end{bmatrix} = \frac{1}{4\pi\epsilon_0} \begin{bmatrix} C_1 & -C_1\mathbb{1}(n_1,n_2)C_2/R_c \\ -C_2\mathbb{1}(n_2,n_1)C_1/R_c & C_2 \end{bmatrix} \begin{bmatrix} \boldsymbol{V}_1 \\ \boldsymbol{V}_2 \end{bmatrix} \tag{3.21}$$

Where $\mathbb{1}(n,m)$ is a matrix consisting of ones of size (n,m). If the two bodies are both conductors, each MSM sphere is at the same voltage this matrix equation is transformed to a vector equation

$$\boldsymbol{Q}_1 = [C_1]\mathbb{1}(n_1,1)V_1 - \frac{[C_1]\mathbb{1}(n_1,n_2)[C_2]}{R_c}\mathbb{1}(n_2,1)V_2 \tag{3.22}$$

$$\boldsymbol{Q}_2 = [C_2]\mathbb{1}(n_2,1)V_2 - \frac{[C_2]\mathbb{1}(n_2,n_1)[C_1]}{R_c}\mathbb{1}(n_1,1)V_1 \tag{3.23}$$

Now the charge on each MSM sphere is approximated as a function of a collection of matrices that do not change with state, and the scalar voltage of each craft. The susceptibility of the total charges, dipoles, and charge tensors to the voltage of each craft are found next.

3.2.2.1 Total Charges

The total charge on each spacecraft is found by summing the charge on each sphere

$$Q = \sum_{i=1}^{n_1} q_i = \mathbb{1}(1,n)\boldsymbol{Q} \tag{3.24}$$

Thus, the scalar charge of body 1 is given by

$$Q_1 = C_S V_1 + C_M V_2 \tag{3.25}$$

Where the self and mutual capacitances are given by

$$C_S = \mathbb{1}(1, n_1)[C_1]\mathbb{1}(n_1, 1) = \sum_{i=1}^{n_1}\sum_{j=1}^{n_1}[C_1]_{i,j} \tag{3.26}$$

$$C_M = \frac{-\mathbb{1}(1, n_2)[C_1]\mathbb{1}(n_1, n_2)[C_2]\mathbb{1}(n_2, 1)}{R_c} = -\frac{\sum_{i=1}^{n_1}\sum_{j=1}^{n_2}[C_1]\mathbb{1}(n_1, n_2)[C_2]}{R_c} \tag{3.27}$$

The scalar self capacitance can be computed with high fidelity using a MSM model with hundreds or thousands of spheres and re-used in each time step for computation. The numerator of the mutual capacitance can be similarly computed at high fidelity and then divided by the norm of the separation vector at each time step.

3.2.2.2 Dipole Moments

The dipole $\boldsymbol{q}$ is defined in a continuous charge distribution and MSM model as

$$\boldsymbol{q} = \int_B \boldsymbol{r}\mathrm{d}q = \sum_{i=1}^{N} \boldsymbol{r}_i q_i = [R]\boldsymbol{q} \tag{3.28}$$

where $[R]$ is a $3 \times N$ matrix containing the x, y, and z coordinates of each MSM sphere:

$$[R] = \begin{bmatrix} x_1 & \dots & x_N \\ y_1 & \dots & y_N \\ z_1 & \dots & z_N \end{bmatrix} \tag{3.29}$$

The dipole is given by

$$\boldsymbol{q} = \boldsymbol{\chi}_S V_1 + \boldsymbol{\chi}_M V_2 \tag{3.30}$$

Where the self and mutual susceptibilities of the dipole for body 1 are

$$\boldsymbol{\chi}_S = [R_1][C_1]\mathbb{1}(n_1, 1) \tag{3.31}$$

$$\boldsymbol{\chi}_M = \frac{-[R_1][C_1]\mathbb{1}(n_1, n_2)[C_2]\mathbb{1}(n_2, 1)}{R_c} \tag{3.32}$$

Once again, these 3×1 vectors can be computed with high fidelity from SMSM models of each body. Each element in the mutual term must be divided by the separation distance, which may change with time.

3.2.2.3 Charge Tensor

The charge tensor is defined from a continuous charge distribution or MSM model as

$$[Q] = \int_B -[\tilde{\boldsymbol{r}}][\tilde{\boldsymbol{r}}]\mathrm{d}q = \sum_i^N -[\tilde{\boldsymbol{r}}_i][\tilde{\boldsymbol{r}}_i]q_i \tag{3.33}$$

Define $[R_s]$ as a $3 \times 3N$ matrix containing the cross product matrix of each MSM sphere position and A is a $3N \times N$ matrix used to interweave three copies of the charge vector made from smaller matrices a.

$$[R_s] = \begin{bmatrix} [\tilde{\boldsymbol{r}}_1] \\ \vdots \\ [\tilde{\boldsymbol{r}}_N] \end{bmatrix} \qquad [a] = \begin{bmatrix} 1 \\ 1 \\ 1 \end{bmatrix} \qquad [A] = \begin{bmatrix} a & 0 & \dots & 0 \\ 0 & a & \dots & 0 \\ \vdots & \vdots & \ddots & \vdots \\ 0 & 0 & \dots & a \end{bmatrix} \tag{3.34}$$

The charge tensor is now found as a function of both voltages, and two 3×3 matrices,

$$[Q_1] = [\psi_S]V_1 + [\psi_M]V_2 \tag{3.35}$$

where the self and mutual susceptibilities of the charge tensor for body 1 are given by

$$[\psi_S] = [R_{s_1}]^T \mathrm{diag}([A][C_1]\mathbb{1}(n_1, 1))[R_{s_1}] \tag{3.36}$$

$$[\psi_M] = -[R_{s_1}]^T \frac{\mathrm{diag}([A][C_1]\mathbb{1}(n_1, n_2)[C_2]\mathbb{1}(n_2, 1))}{R_c}[R_{s_1}] \tag{3.37}$$

These matrices can be found using high fidelity MSM models before propagation and the mutual term can be adjusted by dividing by the separation distance. The derivations are done for body 1, but the susceptibilities for body 2 can easily be found by changing all subscript 2s to 1s and vice versa.

3.2.3 Numerical Validation

For the two-body problem, the accuracy of predictive AFMs is checked against the truth model of SMSM, which places a large number of equal radius spheres uniformly across the surface of the body. The radius of all spheres is varied to achieve the known self capacitance. Although this method is slower to evaluate (due to the much larger number of spheres), it removes the need for hand tuning and has good accuracy relative to commercial FEA software [120]. An example SMSM model for two template "box and panel" spacecraft in close proximity is shown in Fig. 3.3. Note that charge, which is shown as color, tends to bunch up at the corners of conductors and is affected by the nearby spacecraft.

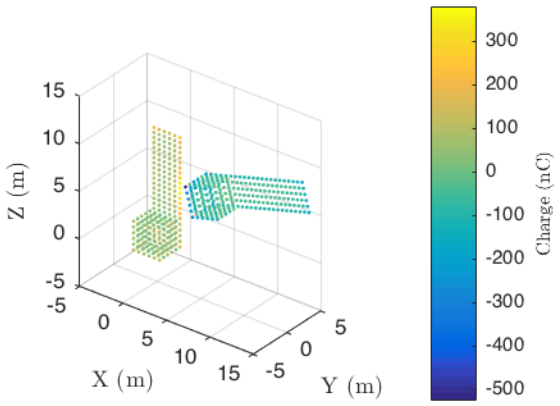

Figure 3.3: Example SMSM configuration for two satellites

For validation, one "box and panel" spacecraft has fixed location and attitude at the origin of the coordinate system. The second spacecraft occupies many different positions and attitudes on a shell of a given radius. SMSM is used to find the force and torque on the fixed craft. The force and torque is also predicted using AFMs with the susceptibilities $C_S, C_M, \boldsymbol{\chi}_S, \boldsymbol{\chi}_M, [\psi_S]$, and $[\psi_M]$ for each craft found before computation from the same 256-sphere SMSM model. The average

percent error is computed for each spherical shell. The percentage error is computed as:

$$PE = 100 * \frac{||\boldsymbol{a}_{\text{AFM}} - \boldsymbol{a}_{\text{T}}||}{||\boldsymbol{a}_{\text{T}}||} \tag{3.38}$$

Where $\boldsymbol{a}$ is either the force or torque, and the subscript "T" indicates the truth model.

The second craft is placed at points on a spherical shell precomputed using a golden spiral algorithm [121] which arranges 20 points equidistantly on the surface of a sphere. The shells are varied in radius logarithmically from 15 to 200 meters in 10 steps. The attitude of the second object at each of these points is changed using three random Euler angles while the first object is held fixed in attitude at the origin. The mean percentage error per shell is shown in Figure 3.4

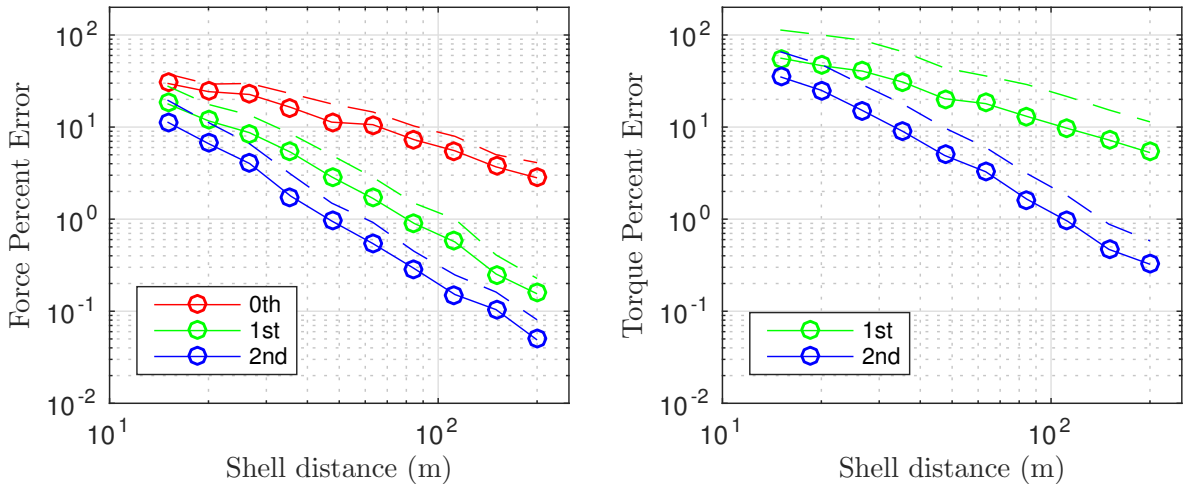

(a) Force percent error

(b) Torque percent error

Figure 3.4: Percentage errors for force and torque using predictive AFMs

The mean percentage error for the zeroth, first, and second order expressions for force are shown as red, green, and blue lines in the force plot. Since there is no zeroth order term for torque prediction, only the first and second order expressions are shown in the torque plot. A dashed line is shown 1 standard deviation above each of these to give a sense of the variation a user should expect.

The errors are initially very high, a few hundreds of percent, but they drop quickly as the spacecraft move farther apart. Since the AFM derivation hinges on the assumption that the space-

craft sizes are much smaller than the distance between them, this matches intuition. The second order term for force drops below 5% error at 25 meters and the second order term for torque drops below 5% at 48 meters.

3.2.4 Analysis and Applications

There are many numerical methods for electrostatic force and torque prediction for conductors. However, they do not give good analytical forms for force and torque. This section summarizes previous work that curve fit the angular and voltage dependencies of electrostatic torque, and then uses AFMs to analytically predict the same result. Next AFMs are used to predict the torque in the case where the center of mass is not aligned with the geometric center of the target object.

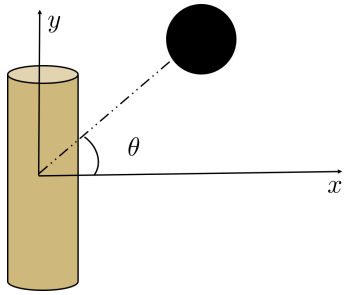

Figure 3.5: Coordinate system for example analysis

Bennett et al. used MSM to calculate the torque on a 3 × 1 meter target cylinder due to a spherical tug craft for different voltages and angles [5]. This is shown in Fig. 3.5. The cylinder has the same voltage magnitude as the sphere, and is always positive while the tug sphere can change the polarity of its voltage: $V_2 = |\phi|, V_1 = \phi$. The torque is only about the z axis due to the symmetry, and is shown as a function of both the angle θ and the voltage ϕ. The torque is shown for near field (2.5 meter separation) and far field (15 meter separation) cases in Fig. 3.6. The voltage dependance follows a quadratic relationship, and the angular dependance is well approximated by $\sin(2\theta)$. The torque is then curve fit to be:[5]

$$L = \gamma f(\phi) g(\theta) = \gamma \phi |\phi| \sin(2\theta) \tag{3.39}$$

In the near field, γ divides into a larger value for attraction γ_a and a smaller value for repulsion γ_r. At further separations the difference between attraction and repulsion is less evident.

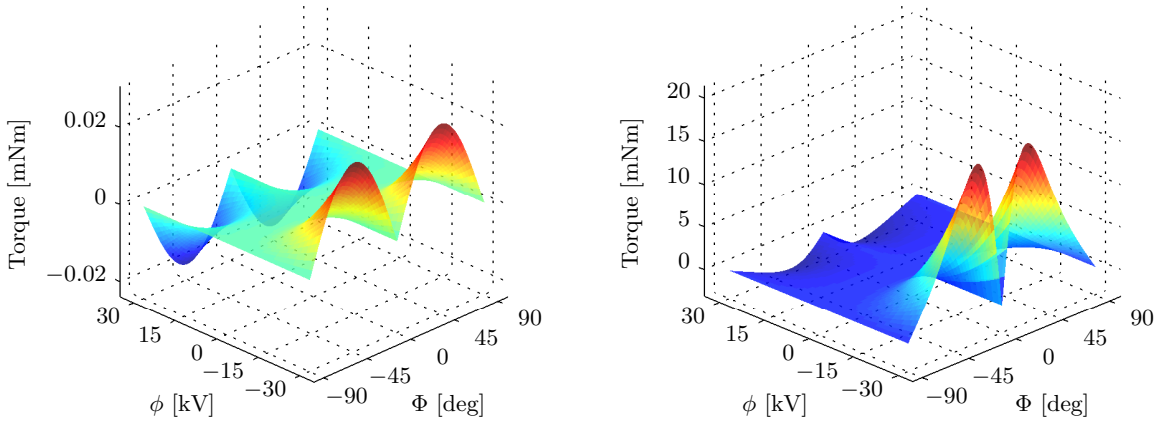

(a) Separation $d = 15$ m

(b) Separation $d = 2.5$ m

Figure 3.6: MSM torque surfaces at a separation distances of $d = 2.5$ m and $d = 15$ m for $V_1 = \phi$ and $V_2 = |\phi|$ [5].

The angular, voltage, and attraction/repulsion trends that have been empirically found using MSM are now derived using AFMs. Referencing Tab. 3.2, the torque on a general body due to a nearby point charge is given by

$$\boldsymbol{L}_2 = \frac{Q_1}{4\pi\epsilon_0 R_c^3}\left[\boldsymbol{q}_2 + \frac{3}{R_c^2}[Q_2]\boldsymbol{R}_c\right] \times \boldsymbol{R}_c \tag{3.40}$$

re-writing this in terms of susceptibilities gives:

$$\boldsymbol{L}_2 = \frac{C_{S1}V_1 + C_M V_2}{4\pi\epsilon_0 R_c^3}\left[(\boldsymbol{\chi}_S + \frac{3}{R_c^2}[\psi_S]\boldsymbol{R}_c)V_2 + (\boldsymbol{\chi}_M + \frac{3}{R_c^2}[\psi_M]\boldsymbol{R}_c)V_1\right] \times \boldsymbol{R}_c \tag{3.41}$$

This equation is grouped into four separate terms

$$\begin{aligned}\boldsymbol{L}_2 = \frac{1}{4\pi\epsilon_0 R_c^3}\Big[&C_M(\boldsymbol{\chi}_S + \frac{3}{R_c^2}[\psi_S]\boldsymbol{R}_c)V_2^2 + C_{S1}(\boldsymbol{\chi}_M + \frac{3}{R_c^2}[\psi_M]\boldsymbol{R}_c)V_1^2 \\ &+ (C_{S1}(\boldsymbol{\chi}_S + \frac{3}{R_c^2}[\psi_S]\boldsymbol{R}_c) + C_M(\boldsymbol{\chi}_M + \frac{3}{R_c^2}[\psi_M]\boldsymbol{R}_c))V_1V_2\Big] \times \boldsymbol{R}_c \\ = \boldsymbol{A}V_1^2 + \boldsymbol{B}V_2^2 + (\boldsymbol{C} + \boldsymbol{D})V_1V_2 \end{aligned} \tag{3.42}$$

In this this 1-D case the torque is purely about the z axis and is written using scalars as

$$L = AV_1^2 + BV_2^2 + (C+D)V_1V_2 \tag{3.43}$$

The terms A and B have one mutual term and are thus 1^{st} order in $(1/R_c)$, C is 0^{th} order, and D is 2^{nd} order. This means that in the far field terms linked to C will persist longer than those linked to A and B, which will persist longer than those linked to D. Because the mutual susceptibilities $(C_M, \boldsymbol{\chi}_M, [\psi_M])$ are negative but the self susceptibilities are positive, A, B and D are negative, but C is positive and larger than D.

Thus the following development switches to the positive variables $F = |A+B|$ and $G = C+D$, and makes use of the definitions $V_1 = \phi, V_2 = |\phi|$ to match prior work [5]. The torque for attractive (L_a) and repulsive (L_r) cases is given by:

$$L_r = (-F+G)\phi^2 = (-F+G)\phi|\phi| \tag{3.44}$$

$$L_a = (-F-G)\phi^2 = (F+G)\phi|\phi| \tag{3.45}$$

In the attractive cases the magnitude of the torque is larger because F and G add rather than subtract. This can be seen in Fig. 3.6a. Additionally, since G has the highest order term, it will matter most in the far field. Since F matters less in the far field, the difference between the attractive and repulsive torque decreases in the far field, which can also be seen by comparing Fig. 3.6a and 3.6b.

In prior work Reference [5] numerically fit the far field parameter γ to a value of $2.234 * 10^{-14}$ for a 3 meter by 1 meter cylinder 15 meters away from a 1 meter diameter sphere. To compute the corresponding value from AFMs, assume that the center of mass is perfectly aligned with the center of charge so that $\boldsymbol{\chi}_S = 0$ and the body axes are aligned so that $[\psi_S]$ is given by $\text{diag}(\psi_B, \psi_s, \psi_B)$, where $\psi_B > \psi_s$. This represents the case of a perfectly axis-symmetric cylinder as shown in Figure 3.5. Ignoring the mutual part of G which decays quickly gives the torque as

$$\begin{aligned} L &= \frac{-3C_{S1}}{4\pi\epsilon_0 R_c^5}\tilde{\boldsymbol{R}}_c[\psi_S]\boldsymbol{R}_c V_1 V_2 \\ &= \frac{3C_{S1}}{8\pi\epsilon_0 R_c^3}(\psi_B - \psi_s)\sin(2\theta)V_1V_2\hat{\boldsymbol{z}} \end{aligned} \tag{3.46}$$

Where G is defined as

$$G = \frac{3C_{S1}}{8\pi\epsilon_0 R_c^3}(\psi_B - \psi_s) \tag{3.47}$$

SMSM is used to find the values of ψ_S and ψ_B which gives $G \approx 2.531 * 10^{-14}$, only a 13% difference with the numerically fit value used in Reference [5]. These two results agree well considering that only a second order AFM model is used and the mutual part of G is ignored, and Reference [5] fits γ to the full MSM solution.

Now consider the same cylinder, but allow the center of mass (CM) to move within the craft by a few centimeters along the y axis ($\boldsymbol{\chi}_S = [0, \chi_S, 0]^T$). The torque is still only about the z axis and is given by

$$\begin{aligned}
\boldsymbol{L}_2 &= \frac{-C_{S1}}{4\pi\epsilon_0 R_c^3}\tilde{\boldsymbol{R}}_c\Big(\boldsymbol{\chi}_S + \frac{3}{R_c^2}[\psi_S]\boldsymbol{R}_c\Big)V_1V_2 \\
&= \frac{-C_{S1}}{8\pi\epsilon_0 R_c^2}\Big[\chi_S\cos(\theta) + \frac{3(\psi_B - \psi_s)}{2R_c}\sin(2\theta)\Big]V_1V_2\hat{\boldsymbol{z}} \qquad (3.48) \\
&= f(V_1, V_2)(g_1(\theta)\gamma_1 + g_2(\theta)\gamma_2) \qquad (3.49)
\end{aligned}$$

Setting $\chi_S = 0$ recovers Eq. (3.46), but even a small CM offset can make the $\cos(\theta)$ term dominate, especially at large separations. As the CM moves away from the geometric center, χ_S grows linearly, and some elements of ψ_S grow quadratically. The torque as a function of θ is shown for a variety of CM offsets in the example of the same cylinder 15 meters away from a 1 μC point charge in Figure 3.7. The different curves are for different values of χ_S – the center of mass offset is shown in the legend.

The torque slowly changes from a perfect $\sin(2\theta)$ to an augmented -$\cos(\theta)$ curve as the CM offset varies. The magnitude of the torque also increases by a factor of 3.38. This factor is even greater at further separations since the $\cos(\theta)$ term has lower order in $1/R_c$. Knowledge of center of mass to center of charge differences are essential for the stability of control laws used for de-spinning of passive space debris. If the center of charge location is not properly accounted for, the sign of the predicted torque can be wrong, leading to instabilities in the closed-loop control discussed in Reference [5].

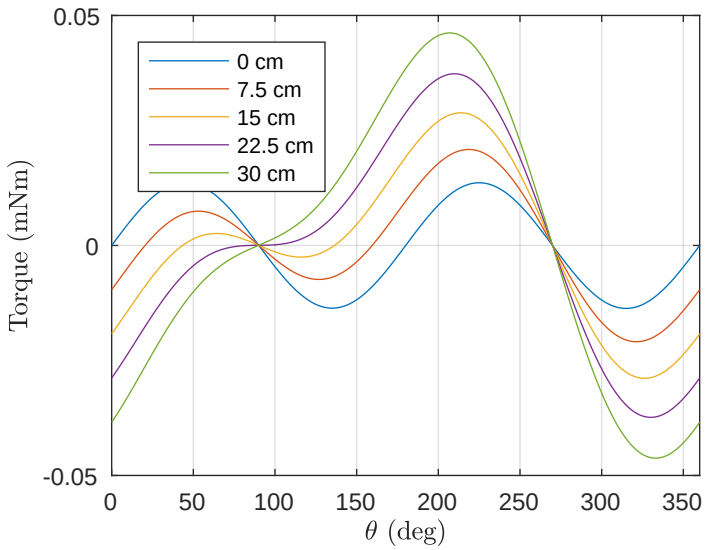

Figure 3.7: Torque on cylinder for a variety of center of mass offsets

3.3 The Method of Moments Foundations for MSM

The next two sections discuss numerical methods for predicting the force and torque on charged spacecraft. This section discusses how the Method of Moments (MoM) relates to the Multi-Sphere Method (MSM) and uses these results to make novel Surface MSM (SMSM) models of general shapes. This is done by first introducing the MSM, and then developing MoM. Next, heterogeneous SMSM models are made from MoM models, a new development. Finally, MoM and SMSM variants are compared in their speed and accuracy.

3.3.1 The Multi-Sphere Method

The Multi-Sphere Method (MSM) was briefly introduced in Sec. 3.2.2, but a more complete description is given here. It is very similar to the MoM, but rather than the elements of the elastance matrix being derived from first principles, they are hand-tuned to match force, torque, or E fields predicted by a higher fidelity model.

As shown in Figure 3.8, MSM approximates a spacecraft as a collection of spheres with variable positions and radii. The voltage on any sphere is a function of both its own charge and

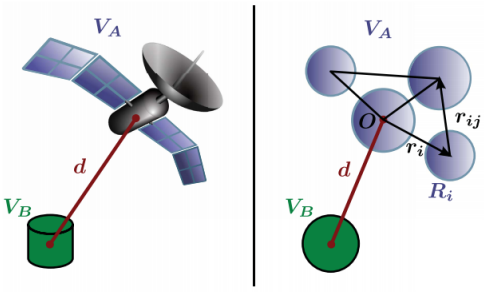

Figure 3.8: Multi-Sphere Method concept

the charge of all nearby spheres. If these spheres are far enough away to be approximated as point charges, the voltage is given by: [67]

$$V_i = \frac{1}{4\pi\epsilon_0}\frac{Q_i}{R_i} + \sum_{j=1,\, j\neq i}^{n} \frac{1}{4\pi\epsilon_0}\frac{Q_j}{r_{i,j}} \tag{3.50}$$

Where q_i and R_i are the charge and radius of the i^{th} sphere, respectively, $r_{i,\,j}$ is the center-to-center distance between spheres i and j, and ϵ_0 is the permittivity of free space constant. If the voltages of each sphere are given by $\boldsymbol{V} = [V_1, V_2, ...V_n]^{\mathrm{T}}$ and the charges are given by $\boldsymbol{Q} = [Q_1, Q_2, ...Q_n]^{\mathrm{T}}$, the relationship between the two is

$$\boldsymbol{V} = [S]\boldsymbol{Q} \tag{3.51}$$

where $[S]$ is the elastance matrix defined below:

$$[S] = \frac{1}{4\pi\epsilon_0}\begin{bmatrix} 1/R_1 & 1/r_{1,2} & \cdots & 1/r_{1,n} \\ 1/r_{2,1} & 1/R_2 & \cdots & 1/r_{2,n} \\ \vdots & \vdots & \ddots & \vdots \\ 1/r_{n,1} & 1/r_{n,2} & \cdots & 1/R_n \end{bmatrix}\begin{bmatrix} Q_1 \\ Q_2 \\ \vdots \\ Q_n \end{bmatrix} \tag{3.52}$$

If the voltage is known, the linear system can be solved for the charges $\boldsymbol{Q}$. In either MSM or MoM, if there are two charged conducting bodies this matrix takes on a block form:

$$\begin{bmatrix} \boldsymbol{V}_1 \\ \boldsymbol{V}_2 \end{bmatrix} = \begin{bmatrix} S_1 & S_M \\ S_M^T & S_2 \end{bmatrix}\begin{bmatrix} \boldsymbol{Q}_1 \\ \boldsymbol{Q}_2 \end{bmatrix} \tag{3.53}$$

where S_M and S_M^T are the mutual blocks of the elastance matrix, and S_1 and S_2 are the diagonal blocks. To find the force and torque on either body apply the Coulomb law between every pair of spheres:

$$\boldsymbol{F}_1 = \frac{1}{4\pi\epsilon_0} \sum_{i=1}^{n} \boldsymbol{Q}_{1_i} \sum_{j=1}^{m} \frac{\boldsymbol{Q}_{2_j} \boldsymbol{r}_{j,i}}{r_{j,i}^3} \tag{3.54}$$

$$\boldsymbol{L}_1 = \frac{1}{4\pi\epsilon_0} \sum_{i=1}^{n} \boldsymbol{Q}_{1_i} \sum_{j=1}^{m} \boldsymbol{r}_i \times \frac{\boldsymbol{Q}_{2_j} \boldsymbol{r}_{i,j}}{r_{i,j}^3} \tag{3.55}$$

where $\boldsymbol{r}_{j,i}$ is a vector that points from sphere j in body 2 to sphere i in body 1 and $\boldsymbol{r}_i$ points from the center of mass of body 1 to sphere i.

3.3.2 The Method of Moments

Although developed independently, SMSM is very close in form to the Boundary Element Method (BEM) [76] and the Method of Moments (MoM). The MoM is a general numerical method that can be used to solve a variety of electromagnetic problems [122]. MoM is similar to SMSM in that it inverts an elastance matrix to solve for the charge distribution, but it differs in how the elastance matrix is formed. In MSM, the elements are formed from the size and location of the spheres, which are tuned to match an externally created truth file. In MoM, they are derived from first principles. Unlike FEA methods, the size of the element is considered which means that each element of the elastance matrix requires a double integral. This nesting of a model within model adds initial complexity, but means that fewer elements are needed than with FEA, since the MoM elements are "smarter". Recently, the MoM is used to estimate the capacitance of geometrically complex spacecraft and their components in [123, 124, 125]. This puts an upper bound on the size of arcs that can occur. This formulation has also been applied to conductors coated with dielectrics as well [126].

The MoM for electrostatics is based on Gauss' law:

$$V(\boldsymbol{r}) = \int \frac{\mathrm{d}q'}{4\pi\epsilon_0 ||\boldsymbol{r} - \boldsymbol{r}'||} \tag{3.56}$$

where $\boldsymbol{r}$ is the observation point and $\boldsymbol{r}'$ is the source point. The source in question is the infinitesimal charge dq and the voltage is being observed. If the source region is discretized into area elements A_i the voltage is

$$V(\boldsymbol{r}) = \frac{1}{4\pi\epsilon_0}\left(\int_{A_1}\frac{\mathrm{d}A'}{|\boldsymbol{r}-\boldsymbol{r}'|}\sigma_1 + \int_{A_2}\frac{\mathrm{d}A'}{|\boldsymbol{r}-\boldsymbol{r}'|}\sigma_2 + \dots\right) \tag{3.57}$$

where σ_i is the surface charge density on the i^{th} area element. Now apply this equation to find the voltage of the centroid of each element to get the following matrix equation:

$$\begin{bmatrix} V_1 \\ V_2 \\ \vdots \\ V_N \end{bmatrix} = \frac{1}{4\pi\epsilon_0}\begin{bmatrix} \int_{A_1}\frac{\mathrm{d}A}{|\boldsymbol{r}_1-\boldsymbol{r}'|} & \cdots & \int_{A_N}\frac{\mathrm{d}A}{|\boldsymbol{r}_1-\boldsymbol{r}'|} \\ \int_{A_1}\frac{\mathrm{d}A}{|\boldsymbol{r}_2-\boldsymbol{r}'|} & \cdots & \int_{A_N}\frac{\mathrm{d}A}{|\boldsymbol{r}_2-\boldsymbol{r}'|} \\ \vdots & & \vdots \\ \int_{A_1}\frac{\mathrm{d}A}{|\boldsymbol{r}_N-\boldsymbol{r}'|} & \cdots & \int_{A_N}\frac{\mathrm{d}A}{|\boldsymbol{r}_N-\boldsymbol{r}'|} \end{bmatrix}\begin{bmatrix} \sigma_1 \\ \vdots \\ \sigma_N \end{bmatrix} \tag{3.58}$$

This large matrix in the center is the elastance matrix $[S]$. In order to match prior work in MSM, each element in $[S]$ is divided by the area of that element to give $[S]$ units of Farads^{-1} and put the charge per element $\boldsymbol{Q}$ on the right hand side rather than the surface charge density to give the expression $\boldsymbol{V} = [S]\boldsymbol{Q}$.

3.3.2.1 Implementation with Square Elements

The first development of MoM in this study was in [17] and used square elements to analyze the specific case of two conducting pieces of aluminized mylar with a thin piece of Dacron netting sandwiched in between. For this basis set, the elements of $[S]$ for two parallel plates perpendicular to the z axis to be:

$$S_{i,j} = \int_{-\Delta y/2}^{\Delta y/2}\int_{-\Delta x/2}^{\Delta x/2}\frac{\mathrm{d}x'\mathrm{d}y'}{\sqrt{(x_c+x')^2+(y_c+y')^2+z_c^2}} \tag{3.59}$$

where x_c, y_c are the center-to-center x and y displacements for the two area elements i and j, and z_c is the displacement in the z direction. If $i = j$, x_c and y_c are both zero. To perform this integration, use the u substitutions $u = x_c + x$, and $v = y_c + y'$:

$$S_{i,j} = \int_{-\Delta y/2+y_c}^{\Delta y/2+y_c}\int_{-\Delta x/2+x_c}^{\Delta x/2+x_c}\frac{\mathrm{d}u\,\mathrm{d}v}{\sqrt{u^2+v^2+z_c^2}} \tag{3.60}$$

Denote the double anti-derivative of this function by s, the elastance entry can be formed from the values of s on the four endpoints of $\mathrm{d}A$:

$$S_{i,j} = s(u_+, v_+) + s(u_-, v_-) - s(u_+, v_-) - s(u_-, v_+) \tag{3.61}$$

Where the $\pm$ subscripts determine the upper or lower limit of that variable. The double anti-derivative s is given below:

$$s(u,v) = \int\int \frac{\mathrm{d}u\,\mathrm{d}v}{\sqrt{u^2+v^2+z_c^2}} \tag{3.62}$$

$$= v\log(\sqrt{u^2+v^2+z^2}+u) + u\log(\sqrt{u^2+v^2+z^2}+v) - z\tan^{-1}\left(\frac{uv}{z\sqrt{u^2+v^2+z^2}}\right) + z_c\tan^{-1}\left(\frac{v}{z}\right) - v \tag{3.63}$$

Where log() is the natural logarithm (base e). Once $[S]$ is known, the charge on each node can be found by solving the linear system. A process for predicting the total charge Q and the dipole $\boldsymbol{q}$ on two nearby conductors is introduced in [127], however that work assumes the distance between the conductors is larger than the conductors themselves. Thus modifications must be made for this case where the plates are 50 cm in length, and only 160 μm apart. To derive the capacitance matrix for two plates, look at the system in block form:

$$\begin{bmatrix} \boldsymbol{Q}_1 \\ \boldsymbol{Q}_2 \end{bmatrix} = \begin{bmatrix} [C_{S_1}] & [C_M] \\ [C_M^T] & [C_{S_2}] \end{bmatrix} \begin{bmatrix} \boldsymbol{V}_1 \\ \boldsymbol{V}_2 \end{bmatrix} \tag{3.64}$$

since both plates are conductors, the voltage is constant across both of them: $\boldsymbol{V}_1 = V_1\mathbb{1}(n_1,1)$ where n_1 is the number of elements used to model plate 1 and $\mathbb{1}(a,b)$ is a matrix consisting only of ones of size $[a,b]$. The total charges on each plate are given by $Q_1 = \sum_i^{n_1}\boldsymbol{Q}_1(i) = \mathbb{1}(1,n_1)\boldsymbol{Q}_1$, thus:

$$Q_1 = \mathbb{1}(1,n_1)[C_{S_1}]\mathbb{1}(n_1,1)V_1 + \mathbb{1}(1,n_2)[C_M]\mathbb{1}(n_1,1)V_2$$

$$= C_{S_1}V_1 + C_MV_2 \tag{3.65}$$

$$Q_2 = \mathbb{1}(1,n_2)[C_M]\mathbb{1}(n_2,1)V_1 + \mathbb{1}(1,n_1)[C_{S_2}]\mathbb{1}(n_2,1)V_2$$

$$= C_MV_1 + C_{S_2}V_2 \tag{3.66}$$

where the model for plate 2 contains n_2 elements. This shows that the elements of the capacitance matrix for two bodies are simply the sum of the elements of the blocks in the large capacitance matrix for every node. Because the two plates are exactly alike except for their relative positions, and because $[S]$ and $[C]$ are symmetric, $C_{S_1} = C_{S_2} = C_S$ and the mutual term C_M is the same. To find the susceptibilities of the dipoles, denote the positions of every node by

$$[R] = \begin{bmatrix} x_1 & x_2 & \dots & x_N \\ y_1 & y_2 & \dots & y_N \\ z_1 & z_2 & \dots & z_N \end{bmatrix} \tag{3.67}$$

for both plates R_1 and R_2. The dipole is given by

$$\boldsymbol{q} = \int_B \boldsymbol{r} \mathrm{d}q = \sum_{i=1}^{N} \boldsymbol{r}_i Q_i = [R]\boldsymbol{Q} \tag{3.68}$$

for a continuous charge and matrix formulation. Now combine with the form for $\boldsymbol{Q}$ from earlier:

$$\begin{aligned} \boldsymbol{q}_1 &= \boldsymbol{\chi}_{1,1} V_1 + \boldsymbol{\chi}_{1,2} V_2 \\ \boldsymbol{q}_2 &= \boldsymbol{\chi}_{2,1} V_1 + \boldsymbol{\chi}_{2,2} V_2 \end{aligned} \tag{3.69}$$

Where the $\boldsymbol{\chi}$ parameters are given by:

$$\boldsymbol{\chi}_{1,1} = [R_1][C_{S_1}]\mathbb{1}(n_1, 1) \quad \boldsymbol{\chi}_{1,2} = [R_1][C_M]\mathbb{1}(n_1, 1) \tag{3.70}$$

$$\boldsymbol{\chi}_{1,2} = [R_2][C_M]\mathbb{1}(n_2, 1) \quad \boldsymbol{\chi}_{2,2} = [R_2][C_{S_2}]\mathbb{1}(n_2, 1) \tag{3.71}$$

For the specific case of two 50 cm plates separated by a 160 μm space, both with their centers of mass displaced by [-2.5, -3.33, 0] cm, the electrostatic parameters are given in Tab. 3.3:

Since the two plates are held together, only the total dipole $\boldsymbol{q} = \boldsymbol{q}_1 + \boldsymbol{q}_2$ and total charge $Q = Q_1 + Q_2$ need to be considered. Finally, the equations for $\boldsymbol{q}$ and Q can be combined to yield the Lorentz force and torque from the voltages only:

$$\begin{aligned} \boldsymbol{F} &= (C_S + C_M)(V_1 + V_2)\boldsymbol{A} \\ \boldsymbol{L} &= \left((\boldsymbol{\chi}_{1,1} + \boldsymbol{\chi}_{2,1})V_1 + (\boldsymbol{\chi}_{1,2} + \boldsymbol{\chi}_{2,2})V_2\right) \times \boldsymbol{A} \end{aligned} \tag{3.72}$$

where $\boldsymbol{A}$ is the total field: $\boldsymbol{A} = \boldsymbol{E} + \boldsymbol{v} \times \boldsymbol{B}$.

Table 3.3: AFM parameters for predicting Lorentz force and torque

Parameter	Value
C_S	20.774 nF
C_M	-20.762 nF
$\boldsymbol{\chi}_{1,1}$	[3.116, 0.692, 0.002] nFm
$\boldsymbol{\chi}_{2,2}$	[3.116, 0.692, -0.002] nFm
$\boldsymbol{\chi}_{1,2}$	[-3.114, -0.692, -0.002] nFm
$\boldsymbol{\chi}_{2,1}$	[-3.114, -0.692, 0.002] nFm

3.3.2.2 Implementation with Triangular Elements

Next, chose triangles as the basis area and parameterize the vector $\mathcal{R} = |\boldsymbol{r}_N - \boldsymbol{r}'|$ as shown in Fig. 3.9. Triangles are chosen as the basis area since they are able to mesh more general shapes than squares. To simplify $\mathcal{R}$, consider two triangles i and j both formed from the corners $[\boldsymbol{A}, \boldsymbol{B}, \boldsymbol{C}]$. The vectors of the form $\boldsymbol{XY}$ point from the point $\boldsymbol{X}$ to the point $\boldsymbol{Y}$. Now it is clear that the separation is given by

$$\mathcal{R} = \boldsymbol{PA} + u\boldsymbol{AB} + u\,v\,\boldsymbol{BC} \tag{3.73}$$

Where $u, v \in [0, 1]$. The u in the $u\,v$ term keeps the $\boldsymbol{BC}$ vector from going its full length near point $\boldsymbol{A}$; without it, one would integrate a parallelogram rather than a triangle. Since the triangles are not necessarily right, $\boldsymbol{AB}$ and $\boldsymbol{BC}$ are not always orthogonal and therefore the set u, v is not orthogonal. The infinitesimal area with this definition for $\mathcal{R}$ is not a square of area $\mathrm{d}u\,\mathrm{d}v$, but rather a trapezoid with

$$\mathrm{d}A = u||\boldsymbol{AB} \times \boldsymbol{BC}||\mathrm{d}u\,\mathrm{d}v \tag{3.74}$$

The elements of $[S]$ in this basis set are then given by

$$S_{i,j} = \frac{1}{4\pi\epsilon_0 A_j}\int_A \frac{\mathrm{d}A}{\mathcal{R}} \quad = \quad \frac{1}{4\pi\epsilon_0 A_j}\int_0^1\int_0^1 \frac{u||\boldsymbol{AB} \times \boldsymbol{BC}||\,\mathrm{d}v\,\mathrm{d}u}{||\boldsymbol{PA} + u\boldsymbol{AB} + uv\boldsymbol{BC}||} \tag{3.75}$$

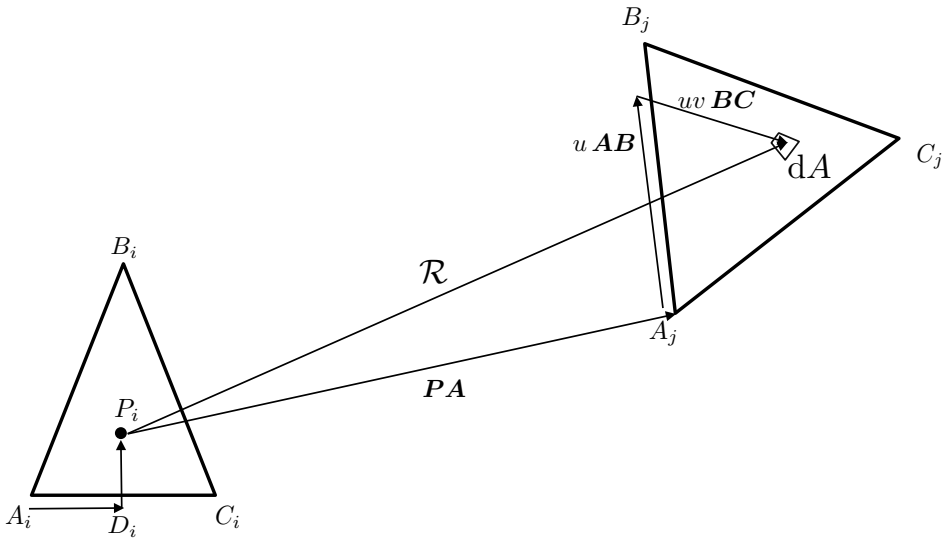

Figure 3.9: Illustration of triangular coordinate system

The denominator is expanded by dotting it with itself and then taking the square root. The first integral over v is

$$S_{i,j} = \frac{||\boldsymbol{AB} \times \boldsymbol{BC}||}{4\pi\epsilon_0 bcA_j} \int_0^1 \log\Big(bc\sqrt{u^2(ab^2 + 2\boldsymbol{AB}\cdot\boldsymbol{BC} + bc^2) + u(2\boldsymbol{PA}\cdot\boldsymbol{AB} + 2\boldsymbol{PA}\cdot\boldsymbol{BC}) + pa^2}$$
$$- \log(bc\sqrt{ab^2u^2 + pa^2 + 2\boldsymbol{PA}\cdot\boldsymbol{AB}u} + \boldsymbol{AB}\cdot\boldsymbol{BC}u + \boldsymbol{PA}\cdot\boldsymbol{BC})\Big)$$
$$+ \boldsymbol{AB}\cdot\boldsymbol{BC}u + bc^2u + \boldsymbol{PA}\cdot\boldsymbol{BC}\ \mathrm{d}u \tag{3.76}$$

where scalars of the form xy are the magnitude of vector $\boldsymbol{XY}$. An analytic solution to the second integral over u has not been found and so this integral is done numerically using an adaptive quadrature algorithm. When $i = j$, there is a special form for $\boldsymbol{PA}$:

$$\boldsymbol{PA} = -\frac{2}{3}\boldsymbol{AB} - \frac{1}{3}\boldsymbol{BC} \tag{3.77}$$

The integral now becomes:

$$S_{i,i} = \frac{1}{4\pi\epsilon_0 A_i}\int_{A_i}\frac{\mathrm{d}A}{\mathcal{R}} \quad = \quad \frac{1}{4\pi\epsilon_0 A_i}\int_0^1\int_0^1 \frac{u\ \boldsymbol{AB}\times\boldsymbol{BC}\,\mathrm{d}v\,\mathrm{d}u}{||(u-2/3)\boldsymbol{AB} + (uv-1/3)\boldsymbol{BC}||} \tag{3.78}$$

The magnitude of $\mathcal{R}$ is once again found by taking the square root of the dot product of the vector with itself. The first integral over v is

$$S(i,i) = \frac{||\boldsymbol{AB} \times \boldsymbol{BC}||}{4\pi\epsilon_0 bcA_i} \int_0^1 \log\left(bc\sqrt{ab^2(2-3u)^2 + (3u-1)(\boldsymbol{AB}\cdot\boldsymbol{BC}(6u-4) + bc^2(3u-1))}\right.$$
$$\left. + (3u-1)bc^2 + \boldsymbol{AB}\cdot\boldsymbol{BC}(3u-2)bc\right) - \log\left(\boldsymbol{AB}\cdot\boldsymbol{BC}(3u-2) - bc^2 + \right.$$
$$\left. bc\sqrt{ab^2(2-3u)^2 - 6\boldsymbol{AB}\cdot\boldsymbol{BC}u + 4\boldsymbol{AB}\cdot\boldsymbol{BC} + bc^2}\right) \tag{3.79}$$

Once again, this integral is done numerically using the adaptive quadrature algorithm. Although the function is singular when $u = 1/3$, the integral is still completed robustly. An alternative method for dealing with this singularity presented in [124] is to divide the triangle into three smaller triangles with the singularity at their common point, and then use a Duffy transformation to remove the singularity. Once this is done the double integral is computed numerically. In contrast, the method presented here does not avoid the singularity as elegantly, but does one of the integrals analytically. In all subsequent computations, a relative error threshold for the adaptive quadrature integrator is 10^{-3}.

These integrals are solved numerically if the basis areas are squares constrained to be parallel to each other as shown in Sec. 3.3.2.1. While this gives nicer analytic solutions, squares do not mesh general shapes as well as triangles do.

To validate this MoM implementation presented here, the self capacitance of a square plate is computed with increasing resolution. The self capacitance is shown as a function of the number of triangles in the mesh in Fig. 3.10a. Beginning with a mesh consisting of only two triangles the self capacitance is near 33 pF, and it increases up to 40.26 pF with 722 triangles for the final run. This is very close to the value from other authors using different methods [128] and involves many fewer elements than would be needed in a FEA scheme. The final charge distribution is shown in Fig. 3.10b. More charge accumulates at the corners of the plate, as expected.

Although the triangular basis does not produce analytical solutions for the elastance like the square basis does, it allows for more general shapes to be modeled. For this reason it is used in the rest of this section.

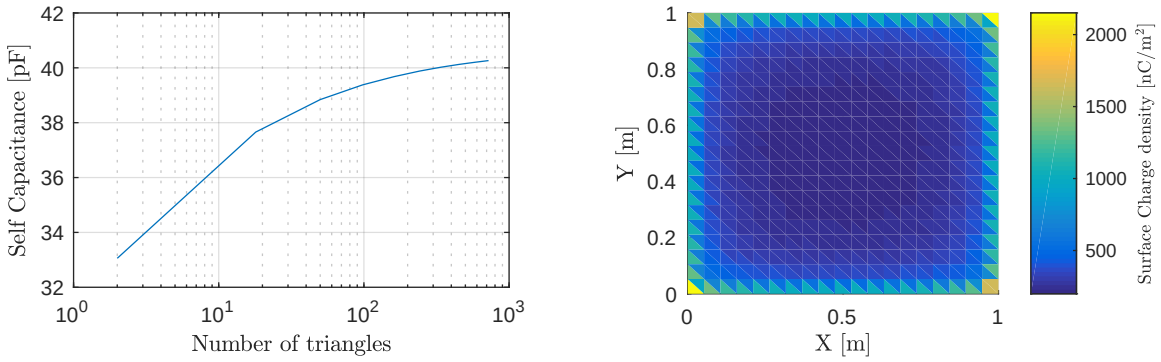

(a) Self Capacitance as a function of number of triangles used

(b) Charge distribution for a square plate charged to 10 kV

Figure 3.10: Validation of MoM implementation on a square plate

3.3.2.3 E field computation

Once the charges on all the triangles have been found, the E field at an arbitrary point $\boldsymbol{P}$ can be found.

$$\boldsymbol{E}(\boldsymbol{P}) = \frac{1}{4\pi\epsilon_0}\left(\int_{A_1}\frac{\sigma_1\boldsymbol{\mathcal{R}}}{\mathcal{R}^3}\mathrm{d}A + \int_{A_2}\frac{\sigma_2\boldsymbol{\mathcal{R}}}{\mathcal{R}^3}\mathrm{d}A + ...\right) \tag{3.80}$$

where $\boldsymbol{\mathcal{R}}$ once again points from the area element to point $\boldsymbol{P}$ and $\mathrm{d}A$ is still $u||\boldsymbol{AB}\times\boldsymbol{BC}||\mathrm{d}u\,\mathrm{d}v$. The E field contribution from each triangle is then:

$$\boldsymbol{E}(\boldsymbol{P}) = \frac{||\boldsymbol{AB}\times\boldsymbol{BC}||Q}{4\pi\epsilon_0 A}\int_0^1\int_0^1 \frac{u^2\boldsymbol{AB} + u^2v\boldsymbol{BC} + u\boldsymbol{PA}\mathrm{d}u\mathrm{d}v}{(u(ab^2u + 2v(\boldsymbol{AB}\cdot\boldsymbol{BC}u + \boldsymbol{PA}\cdot\boldsymbol{BC}) + bc^2uv^2 + 2\boldsymbol{PA}\cdot\boldsymbol{AB}) + pa^2)^{3/2}} \tag{3.81}$$

where A is the area of that triangle. This is integrated over v analytically to give:

$$\begin{aligned}\boldsymbol{E}(\boldsymbol{P}) = \frac{-||\boldsymbol{AB}\times\boldsymbol{BC}||Q}{4\pi\epsilon_0 A}\int_0^1 &\frac{\mathrm{d}u}{((\boldsymbol{AB}\cdot\boldsymbol{BC}u + \boldsymbol{PA}\cdot\boldsymbol{BC})^2 - bc^2\left(u\left(ab^2u + 2\boldsymbol{PA}\cdot\boldsymbol{AB}\right) + pa^2\right))} \\ &\left(\frac{\boldsymbol{BC}\left(u\left(u\left(ab^2 + \boldsymbol{AB}\cdot\boldsymbol{BC}\right) + 2\boldsymbol{PA}\cdot\boldsymbol{AB} + \boldsymbol{PA}\cdot\boldsymbol{BC}\right) + pa^2\right)}{\sqrt{u\left(u\left(ab^2 + 2\boldsymbol{AB}\cdot\boldsymbol{BC} + bc^2\right) + 2(\boldsymbol{PA}\cdot\boldsymbol{AB} + \boldsymbol{PA}\cdot\boldsymbol{BC})\right) + pa^2}}\right. \\ &- \frac{(\boldsymbol{AB}u + \boldsymbol{PA})\left(u\left(\boldsymbol{AB}\cdot\boldsymbol{BC} + bc^2\right) + \boldsymbol{PA}\cdot\boldsymbol{BC}\right)}{\sqrt{u\left(u\left(ab^2 + 2\boldsymbol{AB}\cdot\boldsymbol{BC} + bc^2\right) + 2(\boldsymbol{PA}\cdot\boldsymbol{AB} + \boldsymbol{PA}\cdot\boldsymbol{BC})\right) + pa^2}} \\ &\left. + \frac{(\boldsymbol{AB}u + \boldsymbol{PA})(\boldsymbol{AB}\cdot\boldsymbol{BC}u + \boldsymbol{PA}\cdot\boldsymbol{BC}) - \boldsymbol{BC}\left(u\left(ab^2u + 2\boldsymbol{PA}\cdot\boldsymbol{AB}\right) + pa^2\right)}{\sqrt{u\left(ab^2u + 2\boldsymbol{PA}\cdot\boldsymbol{AB}\right) + pa^2}}\right)\end{aligned} \tag{3.82}$$

This integral over u is computed numerically because an analytic solution was not found. Keep in mind that this is the E field contribution of a single triangle. To compute the E field due to

a full MoM model with many triangles, this expression must be computed for each triangle and summed. To compute the force between two models, the E field due to all triangles in the first model is computed at the centroid of each triangle in the second model and multiplied by the total charge on that triangle.

3.3.3 Comparison of Methods

MSM and MoM both place elements on the surface of the conductor and then use an elastance matrix to solve for the charge distribution. They differ in how they make the elements of the elastance matrix. With MoM, this is done using a double integral of one over the distance from the observation point to a source point in the other element. In MSM, it is one over the distance between the centroids. This is shown schematically in Fig. 3.11.

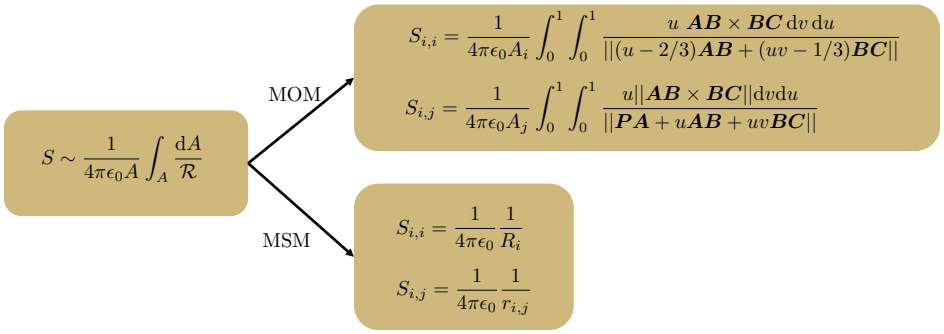

Figure 3.11: Differences between MoM and MSM methods

MSM approximates the integrals of $1/\mathcal{R}$ as either one over the radius of that sphere, or one over the distance to the other sphere. The center to center distance is similar to the vector $\boldsymbol{PA}$, which is the largest term in the denominator. The radius of the sphere is similar to the effective radius of the triangular element. Once again, the MSM spheres are positioned and sized to match force, torque, or E fields computed from a higher fidelity model, so the elements of the elastance matrix have limited physical and geometric significance.

To better understand how the MoM triangular element compares to the MSM sphere, consider a constant area isosceles MoM triangle shown in Fig. 3.12a. When θ is small the triangle is very

tall and skinny, when $\theta = 60°$ the triangle is equilateral, and when θ is near 180° it becomes very obtuse. The self elastance is plotted as a function of θ along with the constant self elastance of a MSM sphere with the same area ($R = \sqrt{A/4\pi}$) in Fig. 3.12b. The assumption of equal area is often a very good assumption, especially for convex shapes [129]. This assumption is used in [63] to calculate the self capacitance of many varied spacecraft shapes. The elastance of the triangle is very small when it is either very obtuse or very acute, and reaches a maximum when the angle is 60°. This is because $\mathcal{R}$ takes on larger values when the triangle is long and skinny in either limit, although the elastance is smaller for a very obtuse triangle than a very acute one. The effective sphere always overestimates the self elastance if computed on the basis of equal area, and this is exaggerated for very acute or obtuse triangles.

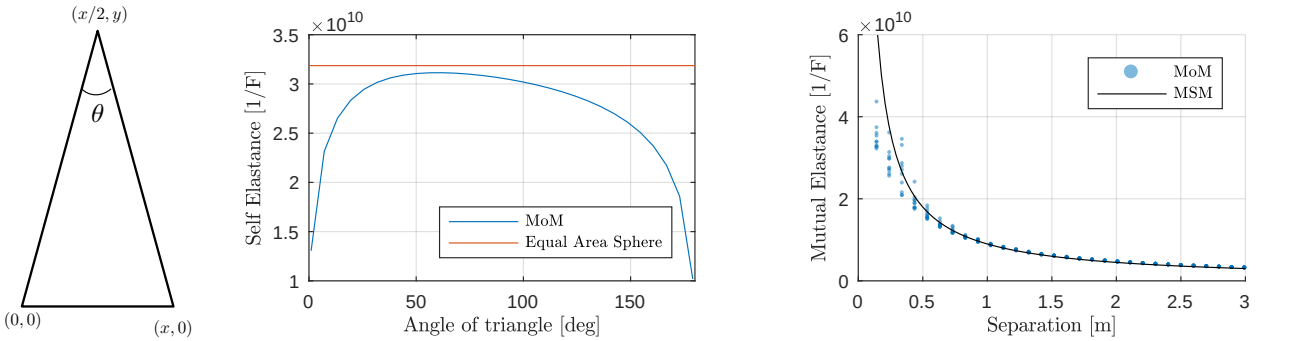

(a) MoM triangle

(b) Self Elastance for a MoM triangle and a MSM sphere

(c) Mutual Elastance for MoM triangles and MSM spheres

Figure 3.12: Comparison of MoM and MSM elements

Next consider the mutual elastance. For two MSM spheres, it is simply given by $1/4\pi\epsilon_0 d$ where d is the separation between the centroids. For two MoM triangles, it is the double integral over the area and is therefore attitude dependent. To investigate this one equilateral triangle is held with its centroid at the origin but has its attitude free while another identical triangle moves along the z axis and stays parallel to the x, y plane. The mutual elastance for this pair of triangles is shown alongside the mutual elastance for a pair of spheres with the same centroid separation in Fig. 3.12c. Special care is taken to ensure that the bottom triangle does not rotate so far that it intersects the upper triangle when the two triangles are close. The triangles both have all side

lengths equal to 1 m and have their centroids on the z axis. For very close separations, the MSM is a little higher than the mean MoM solution but for far distances on the order of the edge length MSM agrees very well with the MoM average, and the MoM variation becomes very small. This is because as the vector $\boldsymbol{PA}$ gets larger and larger, the small u and v terms matter less.

3.3.4 MoM inspired MSM models

To make a MSM model from a MoM model, the mutual terms do not need to be used because the MSM solution matches them quite well using the centroid assumption. However, the radii of the MSM spheres do not match well using the equal area assumption, and there is a lot of sensitivity to the shape of the triangle. Therefore, a mapping is created to find the radius of the MSM sphere that will match the diagonal in the MoM elastance matrix:

$$R_i = \frac{1}{4\pi\epsilon_0 S_{i,i}} \tag{3.83}$$

spheres with this radius are placed at the centroid of each triangle to create the SMSM model. In prior work, all SMSM spheres had the same radius, and it was varied in order to match self capacitance [120]. This approach allows for heterogeneous radius SMSM models to be created. This process is illustrated on a homogeneous case where all MoM triangles (and therefore all SMSM spheres) are the same, and two heterogeneous cases where the MoM triangles are not the same size.

The top row in Fig. 3.13 shows 3 different MoM models for increasingly more complicated geometries. The first model (Fig. 3.13a) is a square plate with 50 identical triangular elements. The resulting SMSM model is shown below in Fig. 3.13d. Although only the diagonal terms in the elastance matrix are matched, the self capacitances only differ by 0.3%. The next plot (Fig. 3.13b) shows a more complex geometry of a cylinder. This mesh is not uniform due to the circular end caps which cause some triangles to have different areas and angles then the others. The area of the elements varies from 0.013 m^2 to 0.024 m^2, with the smallest triangle being at the very center. The resulting heterogeneous SMSM model shown in Fig. 3.13e and the radii in this model vary

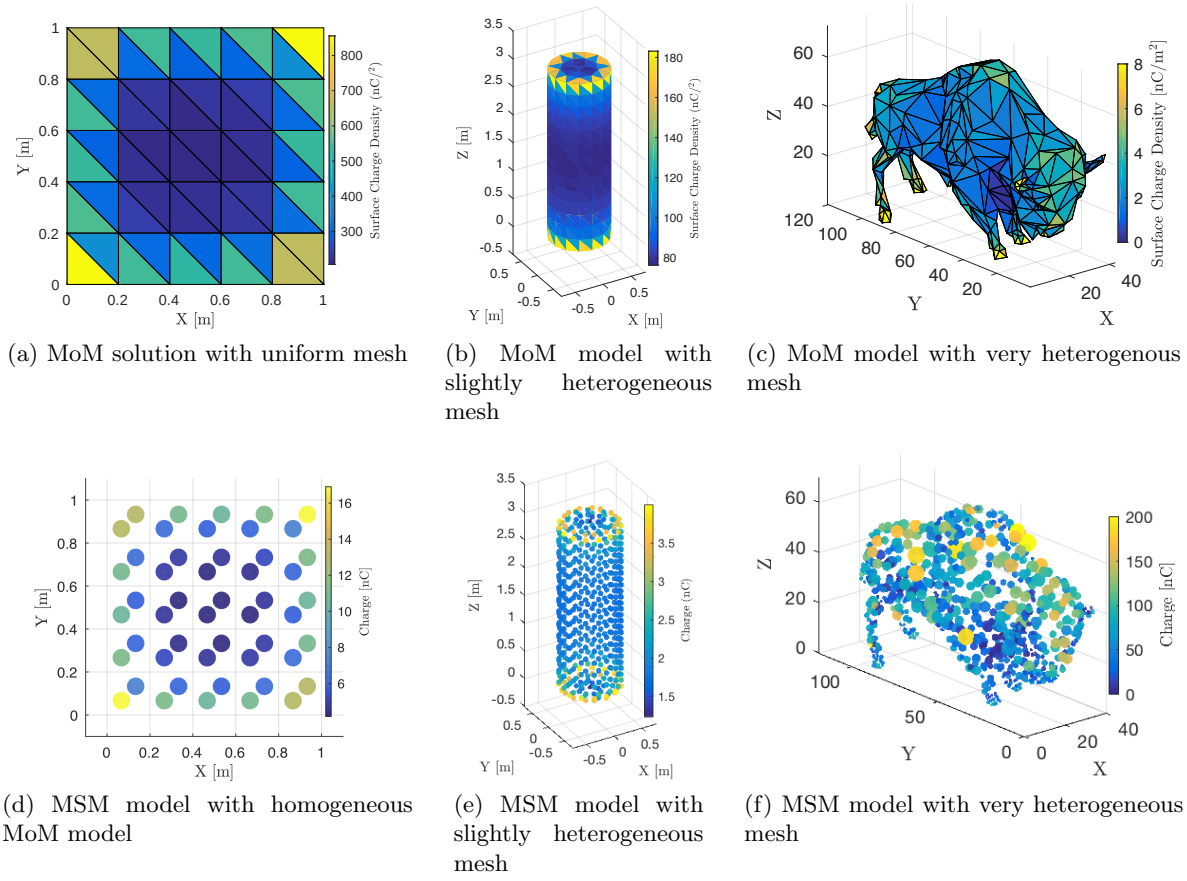

(a) MoM solution with uniform mesh

(b) MoM model with slightly heterogeneous mesh

(c) MoM model with very heterogenous mesh

(d) MSM model with homogeneous MoM model

(e) MSM model with slightly heterogeneous mesh

(f) MSM model with very heterogeneous mesh

Figure 3.13: MSM models created from MoM models. Voltage is 10 kV in all plots

from 3.3 cm to 4.5 cm. These two models only differ by 0.14% percent in self capacitance. The last model, shown in Fig. 3.13c is a STL file of a buffalo[1] that has been down-sampled. This model has 744 triangles with the largest triangle's area is more than 200 times as large as the smallest. The resulting MSM model is shown in Fig. 3.13f and the self capacitances only differ by 0.1%. These three examples show how MSM models can be created from general MoM models. Since this version of MoM uses a triangular basis set, it can be applied to general STL files which allows for a wide array of objects such as the buffalo shown in Fig. 3.13c.

[1] Originally created by abraka_progroup `https://www.thingiverse.com/thing:726062`

3.3.5 Two Body Force and Torque

The self capacitance of simple shapes such as plates and cylinders when computed with MoM and MSM is a good proxy for how the two models compare, but it is not the only pertinent comparison. Close proximity electrostatic tugging is one driver of the need for accurate and fast electrostatic solvers so this section compares MoM to SMSM for the ET. The tug craft is modeled as a 1 m cube with two 2 $\times$ 1 m solar panels charged to +30 kV and is located at $\boldsymbol{r} = [5, 2, 1]^T$ which puts it at a center to center distance of 5.48 m away from the origin, although for some attitudes the solar panels can come much closer. The debris object is a 3 $\times$1 m cylinder model of a spent rocket stage and is held at the origin and charged to -30 kV. In most ET applications, the standoff distance is a more conservative 10-50 m so this case represents one of the harshest electrostatic situations to solve. The truth model for this situation is taken as a very high resolution (10 cm) MoM model which uses 2100 elements for the cylinder and 1656 elements for the tug and is shown in Fig. 3.14. The color scale is capped at 1000 nC/m^2 in this plot, but the actual charge density goes up to almost 4000 nC/m^2 at the corners of the solar panels. Since the electrostatic solution is highly attitude dependent, the force and torque on the cylinder are computed at 16 representative tug attitudes and stored in a master text file. For each of the 16 attitudes, more than 1.7 million numerical integrals are done to make the elastance matrix. Then, this 3756 $\times$ 3756 matrix is inverted to solve for the charge on each element. Finally, almost 3.5 million numeric integrals are done to find the force and torque on both bodies.

Once the truth model is created, the force and torque are computed using lower fidelity MoM and SMSM models while keeping track of the computation time. There are many modifications that can be made to both MoM and SMSM to make them faster and more accurate for the ET that are also analyzed along with the standard ones. Firstly, since both the tug and debris are assumed to be rigid bodies, the two diagonal blocks in the elastance matrix shown in Eq. (3.53) do not change and do not need to be recomputed at each time step. Second, the off diagonal blocks can be computed with SMSM using the centroid assumption even if the diagonal blocks are made

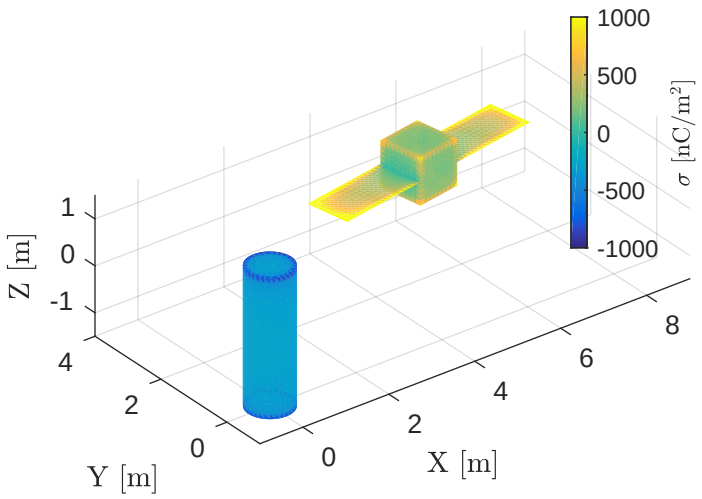

Figure 3.14: High fidelity MoM truth model for close-proximity electrostatic tugging

using MoM. The off diagonal blocks can also not be counted at all which ignores all induced effects. The force and torque can be computed with either MoM of SMSM as well. Finally, a pure SMSM model can have all it's sphere radii varied to match the self capacitance of the truth model rather than from the MoM model that created it. This method works best for the homogeneous and near-homogeneous MoM models since all MSM spheres end up the same size. In all, 7 different MoM/SMSM hybrid models are analyzed for this case. The name of each one and what make it unique is shown in Tab. 3.4.

For each model variant, the mesh is computed with either 258, 500, 830, 1236, or 1730 total elements and then compared to the truth model made with 3756 elements at each of the 16 attitudes. The performance of all 7 model variants is shown in Fig. 3.15. The error is computed as

$$\text{Error} = \frac{1}{2}\left(\frac{||\boldsymbol{F} - \boldsymbol{F}_T||}{||\boldsymbol{F}_T||} + \frac{||\boldsymbol{L} - \boldsymbol{L}_T||}{||\boldsymbol{L}_T||}\right) \tag{3.84}$$

where $\boldsymbol{F}, \boldsymbol{L}$ are the predicted force and torque and $\boldsymbol{F}_T, \boldsymbol{L}_T$ are the true force and torque. The execution time is found using Matlab's tic and toc functions. Despite the same math being performed, the execution time varies considerably. This variance would likely disappear and the overall time would decrease substantially on a more flight-computer-like system. Each dot in Fig. 3.15 repre-

Table 3.4: MoM and SMSM variants used

Name	Diagonal Blocks	Off-Diagonal Blocks	E field	Notes
Full MoM	MoM	MoM	MoM	
Fast MoM	MoM	SMSM	MoM	executes in about 80% of Full MoM time.
Faster MoM	MoM	MoM	SMSM	executes in about 20% of Full MoM time
Fastest MoM	MoM	SMSM	SMSM	executes in less than 1% of Full MoM time
Self MoM	MoM	0	SMSM	no induced effects included
SMSM	SMSM	SMSM	SMSM	
Tuned SMSM	SMSM	SMSM	SMSM	sphere radius tuned to match C_S

sents the error and time for a different model variant with a different number of elements at at different attitude. The model variant is indicated by the color in the figure legend. The number of elements is shown by grouping - each shaded group of points have the same number of elements. Lines of the same color trace the means of both the error and execution time for each model variant. As the number of elements increases, the error drops and and the execution time increases - the groups of points with 258 elements are in the upper left corner of the plot and the groups with 1730 total elements are in the bottom right.

The Full MoM performance is shown in dark blue and is furthest to the right which means it is the slowest. If the number of elements is increased up to 3756, it would have exactly 0% error since that is how the truth model is made. Even with a relatively small (258) number of elements, the error is still below 10% even at this very close separation. The next model variant is the Fast MoM which uses the SMSM approximation for the off diagonal blocks of the elastance matrix. This simplification does not introduce significant errors, but saves a considerable (20%) amount of computation time. The next variant is Faster MoM which uses the SMSM approximation for the E field but not for the off diagonal blocks. This also does not introduce significant errors but saves a lot (80%) of computation time. The next variant is Fastest MoM which uses SMSM for both the off diagonal blocks and the E field. This variant runs very fast when compared to the Full MoM solution and only gives up a very small amount of accuracy. The last MoM variant is the Self MoM which does not include any induced effects. Because of this, there are no mutual terms to compute

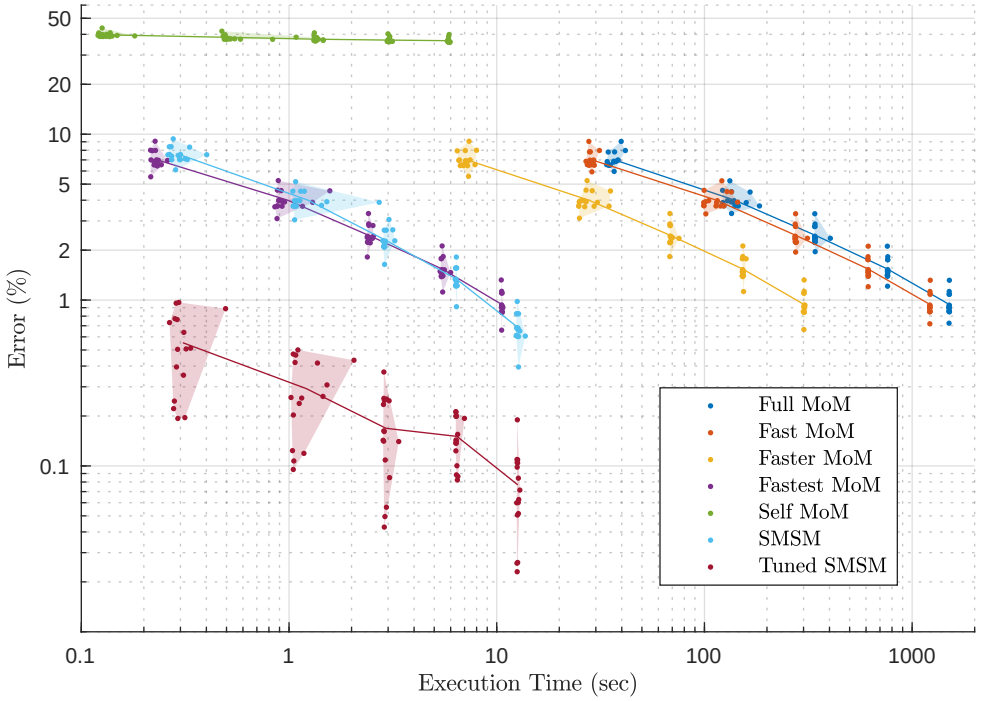

Figure 3.15: Time and error shown for different force and torque prediction schemes

and it runs the fastest of any model. However, it also has the worst errors ($\sim 40\%$) of any model. This shows just how important the mutual interaction is at this close distance. Further away, these errors would drop considerably. The next model is SMSM which is almost identical to Fastest MoM in both time and accuracy. Fastest MoM is slightly faster and more accurate, especially with a small number of elements. The last model variant is tuned SMSM. This model uses the centroids from the MoM model but uniformly sizes all spheres in order to match the self capacitance found from the truth model. The spheres are all the same size even though the triangles are different for the cylinder. This model is by far the most accurate, being almost an order of magnitude more accurate than any other model with the same number of elements.

This section analyzes the relationships between the Method of Moments and the Multi-Sphere Method and uses this information to make better MSM models. This is done by implementing MoM using triangular elements and finding semi-analytic expressions for the elastance matrix elements.

Then, a mapping is created from the diagonal elements of this elastance matrix which sizes the SMSM spheres which are placed at the centroids of the MoM triangles. This mapping allows SMSM models to be made from general STL files which allows for much more general shapes to be modeled. Different SMSM and MoM models are compared in their accuracy and computation time, and a tuned SMSM model with spheres adjusted to match the true self capacitance is found to be the most accurate.

This work shows that MoM and MSM are very closely related methods with different approaches to solving the same integrals, illustrated in Fig. 3.11. A better understanding of how the MoM is formulated lends insight to MSM and allows more complex models to be created. Future work could find faster ways to evaluate the MoM integrals or to tune the self capacitance of heterogeneous SMSM models without making all sphere radii constant.

3.4 MSM Models for Dielectric Spacecraft

Most spacecraft are built to be continuously conducting to avoid differential charging and arcing. However, some of the conducting covering may degrade with time and lose its conductivity. Two scenarios where this may occur is the coverglass coating on the solar panels and the Multi-Layer Insulation (MLI). Solar panels require a glass cover to protect from proton radiation, and there is usually a conductive clear coating over the glass, however, this coating may degrade or flake off and can leave sections of the non-conductive glass exposed. MLI also usually has a gold or aluminum coating, but this may flake off or otherwise degrade. Additionally, some spacecraft are not built fully conducting to begin with, and will have large dielectric portions. In the case of coverglass and MLI, there is a thin layer (10-100 μm) of dielectric sitting directly on top of a conductor connected to spacecraft ground. However, in an effort to save weight, some spacecraft have MLI wrapped around a skeleton frame with very little area of the MLI touching the conducting bus.

This section will investigate two separate questions. First, under what circumstances do dielectrics have to be accounted for to accurately model the force and torque? Second, how can

MSM be modified to account for dielectrics? To answer the first question four different template spacecraft are considered under three different charging scenarios. Once situations that require modeling the dielectric effects are identified, a modification to conducting MSM is presented and tested on the template spacecraft.

3.4.1 Method of Images Analysis

To gain some analytical insight into the first question of when dielectrics need to be accounted for, first consider a much simpler system using the Method of Images (MoI) [80, 113, 81]. If a positive point charge is held a distance z above a grounded infinite conducting plate, a negative induced charge will pool up beneath the point charge due to attraction. For the purposes of calculating the field above the plate, one can assume that there is a negative charge of equal magnitude z below the plate. In this situation, total charge is zero because the conductor "canceled out" the point charge.

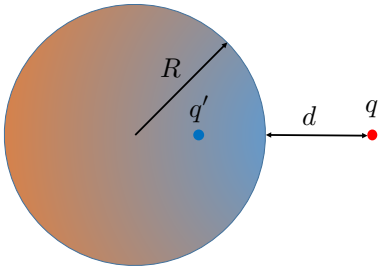

Figure 3.16: Method of Images concept illustration

If a finite sphere is considered rather than an infinite plate, the induced charge q' becomes smaller and moves closer to the surface. For a sphere with radius R, the induced charge is given by

$$q' = -\frac{R}{R+d}q \tag{3.85}$$

where d is the distance between the dielectric charge and the surface of the conductor and q is the point charge as is shown in Fig. 3.16. When d is much smaller than R, the induced charge is nearly equal and opposite to the dielectric charge and the total charge will not be affected by the point

charge. However, when d is comparable to R, the effect of the dielectric charge on the total charge is much more significant.

In a typical laboratory environment, this image charge is supplied by the power supply or the grounding wire to which the conductor is connected. In space, the situation is quite different: consider a sunlit conducting spacecraft bus with an exposed dielectric panel which is shaded. Assume both the conducting bus and dielectric are initially at +10V but then that the dielectric begins to charge negatively due to a large directed flux of electrons and the absence of the photoelectric current. This negative charge on the dielectric lowers the voltage on the conducting bus, which increases the positive currents so that the voltage once again returns to its equilibrium voltage of +10 V. This new charge which forms the image charge comes from the environment due to a biasing of the conducting voltage by the dielectric charge.

There are many differences between the electric field in the vicinity of a point charge and conducting sphere, and the electric field in the vicinity of a charged solar panel and conducting spacecraft bus, but there is still some intuition to gain from this simple analysis. The MOI predicts that when the dielectric is very near the conductor, its charge will be mostly canceled out regardless of how charged it is. Dielectric coatings sitting directly over conductors will likely not cause any significant changes in the E field, force, or torque for this reason. If the dielectric is far from a conductor then the effects are more significant. To understand how this simple principle applies to more complex spacecraft, numerical studies are performed next.

3.4.2 Truth Model Development

The Method of Moments (MoM) is used to create a truth model of the electric field in the vicinity of the spacecraft for a simpler MSM model to match. Prior work [130] has found that MSM models that match the E field also match the force and torque very well, and matching E fields solves a number of other optimization issues as well.

This is done for four spacecraft under three separate charging conditions. The first spacecraft (Fig 3.17a) is a 3 m by 1 m box with a dielectric hovering 25.4 μm ($\sim$1 mil) above the top of the

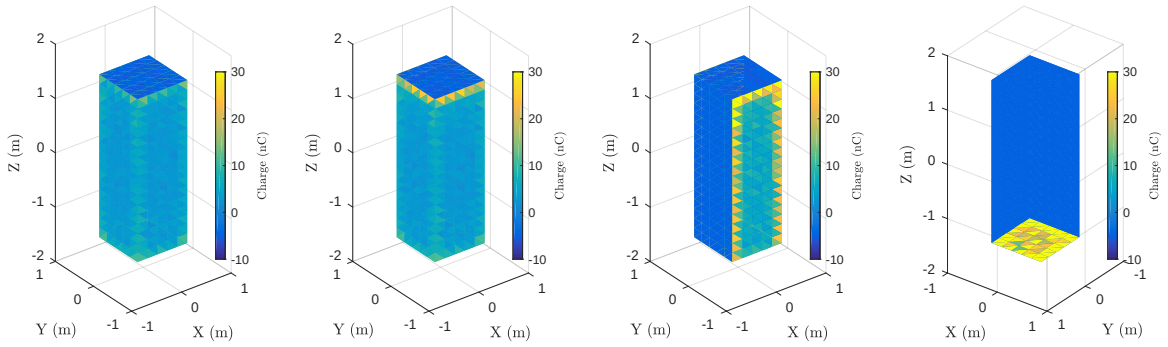

(a) 6 conductor 1 dielectric (b) 5 conductor 1 dielectric (c) 3 conductor 3 dielectric (d) 1 conductor 5 dielectric

Figure 3.17: Four template spacecraft truth models computed using the Method of Moments

spacecraft. This serves as a model of the case where the MLI is stretched over the conducting exterior of the spacecraft. The small displacement off the surface is chosen to be a common thickness for MLI. The second spacecraft (Fig. 3.17b) is almost identical to the first but the top conductor is removed and the dielectric is shifted down to be flush so that it is stretched over the perimeter of the conductor like the surface of a drum. The third spacecraft (Fig. 3.17c) has three panels made of dielectric so that it has equal area of conductor and dielectric. The fourth and final spacecraft (Fig. 3.17d) is composed of 5 dielectric panels and a single conducting panel on the very bottom. All spacecraft are referred to with the shorthand "XcYd" where X is the number of conducting panels and Y is the number of dielectric panels, so the last spacecraft discussed can be indicated by 1c5d. These four spacecraft span the range from a small amount of dielectric completely on top of a conductor to almost all dielectric with very little conductor very far away.

In all subplots in Fig. 3.17 the conductor is charged to +30 kV and the dielectric to -250 nC/m^2. For some models (especially the 1c5d one), the peak charge per element goes up to 94 nC, but the color scale only extends up to 30 nC per element to better show the charge distribution. The positive charge concentrates near the negative dielectric in all cases. Consider the first two cases (Fig. 3.17a and Fig. 3.17b) which differ mainly by the inclusion of a conductor backing behind the dielectric. In the case without the backing, much more charge must accumulate on the

side panels to cancel out the negative charge, while in the case with the backing all the charge accumulates on that backing and is not seen. The other two cases (Fig. 3.17c and Fig. 3.17d) have even more positive charge accumulate to cancel out the large negative panels.

In addition to solving for the charge distribution, the electric field in the vicinity of the spacecraft is also found. The E field is computed at 30 points uniformly spread across each of 12 different spherical shells ranging in radius from 3 to 25 meters. The E field is computed for 3 different cases as well - the first in which only the conductor is charged to +30 kV and the dielectric has no net charge (but has a high voltage due to its proximity to the dielectric), one in which the conductor is charged and the dielectric is additionally charged to -250 nC/m^2, and the last in which the conductor is grounded (0 V) and the dielectric is charged. These 30 points per shell across 12 different shells for 3 different charging scenarios for 4 different spacecraft represent 4320 individual E field computations.

3.4.3 Conductor Solutions

As a first attempt at modeling these spacecraft, the dielectric surfaces are ignored entirely and the optimization is done using a dataset where the dielectric is uncharged. This method has promise for the spacecraft with dielectrics close to conductors such as the 6c1d because of the image charges. A 3 sphere MSM model where all spheres are constrained to stay on the z axis, but can change their height and radius is optimized using only the conducting data for all spacecraft. The cost function is the average percent error of the E field the MSM model produces relative to the truth model. The final solution for the 3c3d spacecraft is shown in Fig. 3.18 with its three spheres constrained along the z axis. Since all three spheres have a tunable radius and height, there are 6 free parameters in this model.

This process of ignoring the dielectrics is applied to all four spacecraft and their performance in both the conducting and mixed charging regimes is shown in Fig. 3.19. All MSM models have only conducting spheres and are optimized using just the conducting dataset (+30 kV and no dielectric charge).

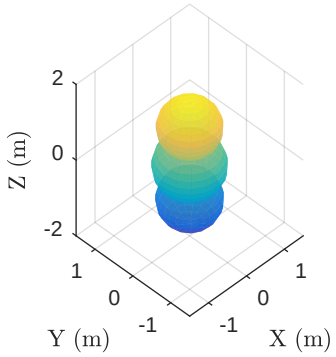

Figure 3.18: Optimal MSM model for 3c3d spacecraft ignoring dielectrics

The performance of the 6c1d model is shown using a violin plot in Fig. 3.19a. Violin plots are a good way to show a lot of data at once; they essentially show multiple histograms rotated by 90°. The width of each bar corresponds to the number of cases in the bin shown on the y axis for the case shown on the x axis. In the following violin plots, the cases correspond to how far away the E field is measured, the bins correspond to the percentage error (with reference to the MoM truth model), and the color corresponds to the charging scenario, with the dark blue being the conductor, (C) and the aqua being the mixed case (M). For the 6c1d spacecraft (Fig. 3.19a), the errors for the C and M case are incredibly similar, and both very good - they are almost always below 1% error, and after 10 m they are always better than 0.1% error. They are similar because the induced charge on the top plate of the conductor almost entirely cancels out the dielectric charge, making it as though the charged dielectric is not even there.

Moving to the 5c1d case (Fig. 3.19b), the conducting regime errors are almost unchanged, but the mixed charging regime errors are larger. This is because the two cases are no longer as similar due to the lack of a top conducting panel to cancel out the dielectric charge. Despite this, the conductor only model has only a few percent error in the M category, which is more than accurate enough for many missions. The 3c3d spacecraft (Fig. 3.19c) is slightly harder to model with mixed regime errors in the 10% range even though conductor errors are still very small. This is because much of the dielectric is much farther away from the conductor. Moving finally to the

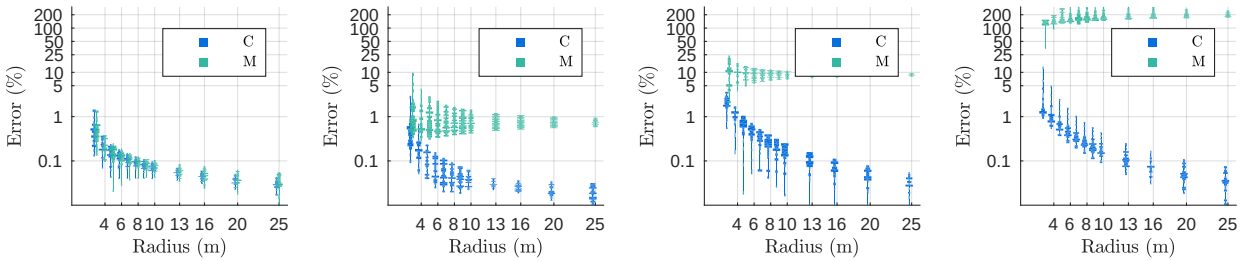

(a) 6c1d (b) 5c1d (c) 3c3d (d) 1c5d

Figure 3.19: Performance of a conductor-only MSM model in pure conducting (C) and mixed (M) charging regimes

1c5d case (Fig. 3.19d), the C errors are still very good, but the M errors have increased up to 200% error.

From this analysis, it seems that one would not bother to model dielectrics for the 6c1d or the 5c1d, but probably the 3c3d and definitely for the 1c5d. To expand this analysis to more continuous charging conditions, the dielectric charge density is swept from 1 - 1000 nC/m and voltage from 10V to 100 kV for each spacecraft. For each charging condition, compute the charge percentage error as $100\,(Q_C - Q_T)/(Q_T)$ where Q_C is the total charge found if the dielectric is ignored and Q_T is the true total charge. This charge error correlates with the percentage error when computing force in the far field, and should be small to ensure accuracy. The charge error is always 100% when the voltage is zero because the conductor only solution will always predict $Q_C = 0$, even if the total charge Q_T is negligible. Thus, this method for judging the charge error can produce misleading results when the voltage is small. The charge errors are shown in Fig. 3.20 where the different colors indicate different spacecraft.

In general, the charge errors grow as the dielectric charge is increased, which makes sense as the ignored charge becomes larger. The charge errors are also large when the voltage is low because they are percentage based. The 1c5d spacecraft has the worst errors, as expected since it is mostly dielectric, and has many panels which do not come close to the conductor. For this template spacecraft, errors will be large for almost all dielectric and conductor charge configurations. For the two intermediate spacecraft - the 3c3d and 5c1d, the performance is very similar. They both have

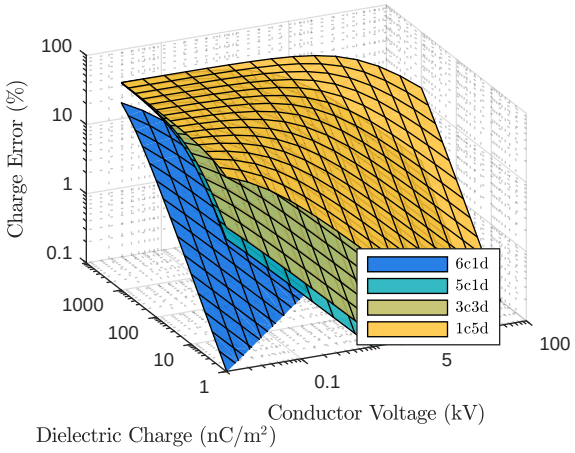

Figure 3.20: Charge error as a function of voltage and dielectric charge density for four spacecraft

charge errors larger than 10% if the dielectric charge is larger than 500 nC/m^2 when the voltage is 5 kV. The 6c1d spacecraft is the bounding case - neglecting dielectrics only introduces errors when the spacecraft is at very low voltages, at which the actual charge and resulting force and torque will be very small.

This manner of analysis can be used to quickly check if dielectrics ought to be considered in an analysis. First the self and mutual dielectric capacitances are found for the spacecraft in question. Next the voltage and dielectric charge ranges are found, and finally the charge error is computed for the voltage and dielectric charge ranges. If the charge error is higher than the acceptable error for that mission, dielectrics must be included. This answers the first question "when ought dielectrics to be considered?" Now, how best to model dielectrics is considered.

3.4.4 Dielectric MSM Methodology

Dielectrics charge on much slower timescales than conductors because of their large mutual capacitance. Because of this, they are treated as known point charges rather than a known voltages. To modify conducting MSM to include dielectrics, the model is broken into two parts for the

conductor and dielectric:

$$\begin{bmatrix} \boldsymbol{V}_C \\ \boldsymbol{V}_D \end{bmatrix} = \begin{bmatrix} S_C & S_M \\ S_M^T & S_D \end{bmatrix} \begin{bmatrix} \boldsymbol{Q}_C \\ \boldsymbol{Q}_D \end{bmatrix} \tag{3.86}$$

where the C and D subscripts denote conductor and dielectric respectively, and the M is for mutual. Since the voltage of the conductor and the charge of the dielectric are assumed known and the charge distribution for the conductor is sought, the top line of this equation is rearranged to give

$$\boldsymbol{Q}_C = [S_C]^{-1}(\boldsymbol{V}_C - [S_M]\boldsymbol{Q}_D) \tag{3.87}$$

Then the total charge $\boldsymbol{Q}$ can be formed as $\boldsymbol{Q} = [\boldsymbol{Q}_C, \boldsymbol{Q}_D]^T$. The force, torque, or E field are then computed as discussed in the earlier section.

When modeling conducting bodies, the MSM optimization problem is fairly simple - change the position and size of the spheres to best match the force, torque, or E field from a truth model. With dielectrics, there are a few changes - now there are both conducting spheres and point charges which may be moved, and there are many different charging scenarios to consider when producing the truth model. With conductors, it does not matter what voltage is chosen for the truth model, as long as it is not zero. With dielectrics included, models that work well for a high voltage case can perform very poorly for a high charge case.

To address the problem of optimizing for just one charging regime, three charging scenarios are included in the truth file; one with just the conductor charged and no charge on the dielectric, one with both conductor and dielectric charged, and one with just the dielectric charged. Because using many point charges does not greatly slow down computation time, and to make the optimization easier, the point charges are uniformly distributed over the dielectric panels. This scheme is shown in Fig. 3.21.

An initial guess for the spheres location and radius is supplied to the optimizer. The optimizer uses the points model along with the spheres model to compute the E field at all 30 points in all of the 12 shells for all 3 charging scenarios. The cost is computed from the average percentage error

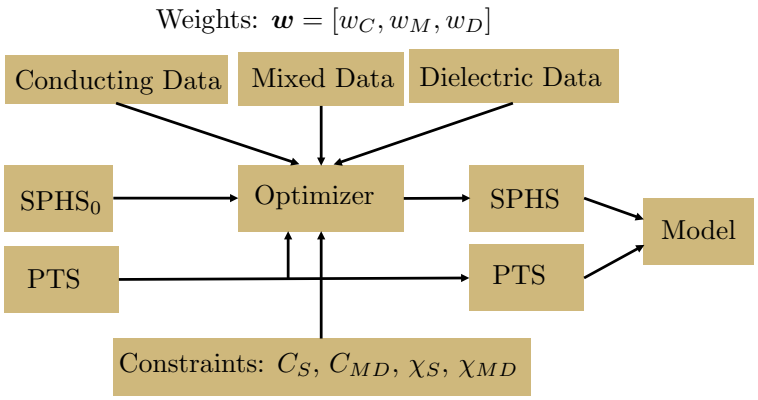

Figure 3.21: Optimization scheme for dielectric MSM

for all three charging scenarios and the weights. A selection of constrains, discussed later, can also be used to ensure behavior in the far field. The final spheres model is combined with the prescribed points model to make the full model for that spacecraft.

3.4.5 Optimization Constraints

Prior work in optimizing MSM models for conductors [131, 130] has shown that enforcing that the MSM model have the same self capacitance as the object being modeled can make the optimization more robust and also provides a guarantee of correctly modeling the force in the far field. The self capacitance is a scalar parameter that determines how much charge is present at a given voltage. For a spacecraft with both dielectric and conducting components, the total charge is a function of both the conductor voltage and the dielectric charge. The total charge is the sum of the dielectric charge and the conductor charge:

$$Q = \mathbb{1}_{n_C}^T \boldsymbol{Q}_C + \mathbb{1}_{n_D}^T \boldsymbol{Q}_D \tag{3.88}$$

where the notation $\mathbb{1}_n$ indicates a column vector of ones with n elements and n_C and n_D denote the number of conducting and dielectric elements. Now substitute in Eq. (3.87) for $\boldsymbol{Q}_C$ and rearrange:

$$\begin{aligned} Q &= \mathbb{1}_{n_C}^T [S_C]^{-1} (\boldsymbol{V}_C - [S_M]\boldsymbol{Q}_D) + \mathbb{1}_{n_D}^T \boldsymbol{Q}_D \\ &= C_S V_C + C_{MD} Q_D \end{aligned} \tag{3.89}$$

where the self capacitance C_S and mutual dielectric capacitance C_{MD} are defined as

$$C_S \equiv \mathbb{1}_{n_C}^T [S_C]^{-1} \mathbb{1}_{n_C} \tag{3.90}$$

$$C_{MD} \equiv (1 - \mathbb{1}_{n_C}^T [S_C]^{-1} [S_M] \mathbb{1}_{n_D}^T / n_D) \tag{3.91}$$

The self capacitance determines how sensitive the total charge is to the voltage on the conductor, and the mutual dielectric capacitance determines how sensitive the total charge is to the dielectric charge. If $C_{MD} = 1$, then adding charge to the dielectric adds exactly that much to the total charge. If $C_{MD} = 0$, then adding charge to the dielectric adds no charge at all to the total charge because the induced charge cancels it out. Referencing back to the MOI solution $C_{MD} \approx 1 - R/(R+d)$. So when the dielectric is close to the conductor ($d \ll R$), C_{MD} will be close to zero, and the dielectrics will have minimal effects. When the dielectric is far from the conductor ($d \sim R$), C_{MD} will be close to one and dielectrics will play a larger role. Unlike the self capacitance which has units of Farads, C_{MD} is dimensionless and is always between 0 and 1.

The total charge is 0^{th} order moment of the charge distribution. The first order moment of the charge distribution is the dipole ($\boldsymbol{q}$). The dipole is a 3×1 vector formed by multiplying the total charge by a vector pointing from the center of the coordinate system (usually at the center of mass) to the center of the charge and is discussed in greater detail in the section on Appropriate Fidelity Measures. MSM models that match the total charge and the dipole will correctly predict the torque as well as the force in the far field.

For a MSM model with both dielectric and conducting parts, the dipole is a combination of the dipole from both the dielectric and conducting portions:

$$\boldsymbol{q} = \boldsymbol{\chi}_S V + \boldsymbol{\chi}_{MD} Q_D \tag{3.92}$$

where the parameters $\boldsymbol{\chi}_S$ and $\boldsymbol{\chi}_{MD}$ are the self and mutual susceptibilities defined by:

$$\boldsymbol{\chi}_S \equiv [R_C][S_C]^{-1} \mathbb{1}_{n_C} \tag{3.93}$$

$$\boldsymbol{\chi}_{MD} \equiv \frac{[R_D]\mathbb{1}_{n_D}}{n_D} - \frac{[R_C][S_C]^{-1}[S_M]\mathbb{1}_{n_D}}{n_D} \tag{3.94}$$

where $[R_C]$ and $[R_D]$ are matrices containing the location of every sphere/point in an MSM model or the centroid of every triangle in a MoM model for both the conductor and dielectric:

$$[R] = \begin{bmatrix} x_1 & \dots & x_N \\ y_1 & \dots & y_N \\ z_1 & \dots & z_N \end{bmatrix} \tag{3.95}$$

The self susceptibility determines how sensitive the total dipole is to the conductor voltage, and the mutual susceptibility determines how sensitive it is to the dielectric charge. If the mutual susceptibility is small, the charge on the dielectric will not influence the dipole strongly. Once again the units differ because the two susceptibilities multiply different quantities.

These four parameters, C_S, C_{MD}, χ_S, and χ_{MD}, are all intrinsic and unchanging properties of a given spacecraft geometry. These constraints are enforced during optimization to understand how they affect the performance. Since these four constrains can be enforced in groups, there are 16 different unique sets of constraints that can be used. For each constraint set, the MSM solution is optimized for the 3c3d spacecraft using a prescribed points model for the dielectric which uses 36 points and a seven sphere MSM model which has 3 spheres on each of the conductor panels and one along the central axis.

The results are shown in Fig. 3.22. The MSM solution for one of the 16 cases is shown in Fig. 3.22a. This particular optimization was constrained to match the self capacitance and self susceptibility, but not either of the mutual terms. The performance of this model is shown as a triple violin plot in Fig. 3.22b. The errors for all three scenarios decreases with distance, dropping below 1% at around 10 m for the dielectric case and near 7 m for the conductor and mixed case. The maximum error is near 10% but that is only for the dielectric only case at the closest distance. Since it would be tedious to show a triple violin plot for each of the 16 different constrain cases, the performance is reduced to two scalar values - first the cost function which is the mean of the errors for each field point at each radius and each charging condition. This value is shown for all of the 16 constraint cases in Fig. 3.22c.

The first thing to notice is that the errors are all very good regardless of the constraints used.

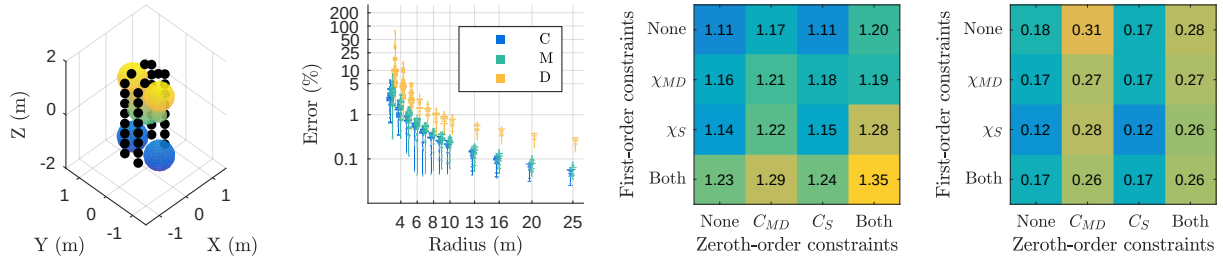

(a) MSM solution matching C_S and $\boldsymbol{\chi}_S$ (b) MSM solution perfomance (c) Mean Error (d) Final Error

Figure 3.22: Effects of enforcing constraints

The maximum mean error is 1.35%, which is less than other uncertainties in the system are likely to be. The lowest error is found with no constrains at all, which is expected as the optimizer has access to more solutions than the constrained solutions. In general, the leftmost and third-from-left columns are similar to each other and darker than the rest, indicating that the optimizer picks MSM models that match self capacitance even if that constraint is not enforced. The first and third rows also have lower error than the other rows, especially when combined with the first and third columns. This indicates that C_S and $\boldsymbol{\chi}_S$ are the most important parameters to match. Looking at the outside edge near the upper left corner shows the effects of including just one constraint at a time. No constraints at all gives a mean error of 1.11 %, just $\boldsymbol{\chi}_S$ gives 1.14 %, $\boldsymbol{\chi}_{MD}$ gives 1.16 %, C_{MD} gives 1.17 %, and C_S gives the same 1.11%. This analysis of looking at the constraints one at a time supports the idea that C_S and $\boldsymbol{\chi}_S$ are the most important parameters to match.

The second scalar value to draw from the violin plots is the mean error for all charging conditions at 25 meters. This final error should be more sensitive to enforcing constraints due to its distance and is shown in Fig. 3.22d. The first and third column are even more dramatically better than the rest than in the mean error, as is the third row. Here, the lowest error comes from enforcing the self susceptibility constraint either with or without the self capacitance. The mean and final error analysis both show that C_S and $\boldsymbol{\chi}_S$ are the most important constraints to enforce for this spacecraft. Enforcing both only hurts the mean error by 0.04%, and provides a guarantee of performance in the far field.

This particular seven sphere, 36 point model has 8 free parameters, which makes it possible to enforce any combination of constraints and still have many free parameters to tune for optimality. Despite this, it is still a very difficult optimization requiring very precise initial conditions. For more simple MSM models with fewer free parameters, it is not possible to enforce all of these constraints depending on the number of free parameters. It is also possible that the constrains are not compliant for some MSM models — for example a MSM model that had all spheres constrained on the z axis would never be able to match any non-zero x and y components of $\boldsymbol{\chi}_S$. For this model, constraints aid the solution since they are compliant. For other models, they are detrimental or impossible to enforce.

3.4.6 Performance and Time Analysis

The earlier section investigated the effect of constraints while keeping the model (3c3d spacecraft with 7 spheres and 36 points) constant. This section uses no constraints, but investigates the E field fitting performance while changing the spacecraft and its sphere and points model. For all spacecraft, the points are distributed equidistantly across the dielectric panels as shown in Fig. 3.22a. This model has two rows which results in 36 points, one row gives in 11 points while 3 rows will give 75 points. For dielectric-heavy spacecraft (such as the 1c5d) there are naturally many more points than for conductor-heavy spacecraft (such as the 6c1d).

For all spacecraft, the spheres model uses a few spheres placed either along the z axis or in the plane of the conducting panels. The simplest model uses two spheres where both spheres have variable radii and position along the z axis. The next most complicated model has 3 spheres with variable radii and height for 6 total parameters. More advanced models have one sphere free to move along the z axis and a few rings of spheres centered on the panels that can change height and radius. Fig. 3.22a shows a model for the 3c3d spacecraft with three rings of spheres along the vertical panels and one central sphere along the z axis for a total of seven spheres. For the 1c5d spacecraft, none of the above models work well, so 1, 4, and 5 sphere models are made which keep all spheres in the $z = -1.5$m plane. In total, 10 separate sphere and 9 separate point models are

considered for a total of 53 optimizations which are shown in Fig. 3.23. If no points are used, the dielectric dataset is ignored because it will always give 100% error.

(a) 6c1d (b) 5c1d (c) 3c3d (d) 1c5d

Figure 3.23: Mean error of E field fitting for different sphere and point models

The first plot (Fig. 3.23a) shows how well different designs model the E field surrounding the 6c1d spacecraft. Earlier analysis found that dielectrics did not need to be modeled, and this analysis confirms that and additionally finds that that adding points actually hurts the solution. If no points are used, the mean errors are all less than 0.2%, but if points are added they jump up to at least 20% and sometimes almost 100%. Among the conductor-only solutions, there is very little variation, with more spheres helping in general except for the 5 sphere model.

Moving to the 5c1d spacecraft (Fig. 3.23b), adding points still makes the solution worse but not by as much as the 6c1d. Ignoring the dielectric gets errors near 0.5%, but including them gets errors near 5%. In general, more spheres helps, with the exception of the 5 sphere model, which appears to be an all-around bad model regardless of the number of points used on both the 6c1d and 5c1d spacecraft. For both of these spacecraft, one ought to ignore the dielectrics entirely.

The 3c3d spacecraft (Fig. 3.23c) has equal area of conductor and dielectric and has slightly smoother behavior. Ignoring dielectrics results in mean errors near 4%, and including them can either help or hurt this solution. For instance, including points makes the solution nearly 3 times worse for a two sphere model, but nearly 3 times better for a 7 sphere model. For any models with more than 3 spheres, dielectrics ought to be included. Except for the first row, more spheres and points both help the solution. Since the columns are more distinct than the rows, one can conclude

that the number of spheres is more important than the number of points, although the jump from 0 to 11 and 11 to 36 points is significant.

Finally, the 1c5d spacecraft mean error is shown in Fig. 3.23d. Since this spacecraft is virtually all dielectric, a points only solution is also considered. Both the points and only spheres cases preform poorly with errors near 100%. For the cases with both spheres and points, the errors are much better, and decreases as spheres and points are added. In contrast to the 3c3d spacecraft, the rows are just as distinct as the columns, which indicates that adding points for this spacecraft is more valuable than on the 3c3d, which makes sense since the dielectric is larger and plays a larger part in the E field.

Overall, the two spacecraft for which dielectrics ought not be included are the easiest to model with errors always less than 0.5%. The 3c3d spacecraft provides an intermediate case where the number of spheres being used determines whether points ought to be used. For all spacecraft, a model exists which keeps the average error below 1.5%, which is likely lower than other errors expected in the system.

Many of the proposed applications of electrostatic force modeling must evaluate quickly as well as accurately. To investigate the trade space between accuracy and time, the number of arithmetic operations needed is found. For an MSM model with n conducting spheres and m dielectric point charges, the number of operations N required to find the charge at each node (using Eqn. (3.87)) is

$$N = \frac{2}{3}n^3 + \frac{11}{2}n^2 - \frac{25}{6}n + 2mn \tag{3.96}$$

if using Gauss-Jordan elimination for the matrix inverse.

This measure is not the full number of computations that must occur to compute the electrostatic force or torque, but is the most time-intensive step. All other steps will involve the number of points and spheres in both models and are therefore more difficult to include without introducing unnecessary complexity.

The mean error function is plotted in Fig. 3.24 for all spacecraft and all models as a function

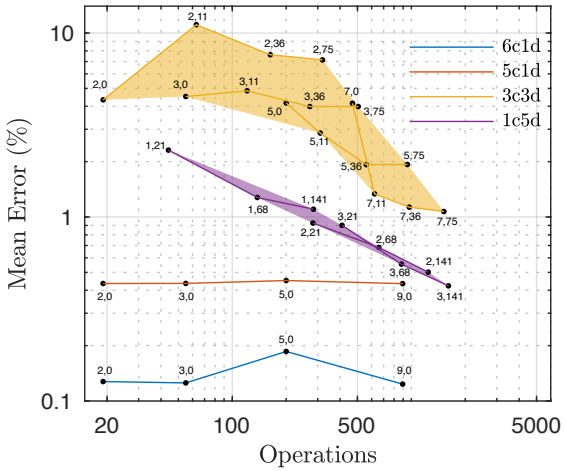

Figure 3.24: Mean error for all spacecraft as a function of arithmetic operations

of operations, which are a proxy of computer time. The small pairs of numbers indicate which model is used – a pair of i, j indicates a model with i spheres and j points, and the color indicates the spacecraft. For the 6c1d and 5c1d spacecraft, only the conductor-only solution is shown since the others have poor performance. For the other two spacecraft, all the designs are shown with lines indicating models with the same number of spheres. Additionally, a boundary line and shading is used to indicate the likely Pareto front.

It is now clear that the 3c3d spacecraft is the least accurate, but still has mean error below 10% for all but one design. The 1c5d spacecraft follows a much tighter boundary and is more accurate while requiring roughly the same computational effort. Lastly, the two conductor only spacecraft are not strong functions of the computational effort but are very accurate no matter which model is used. This plot, or others like it, could be used to decide which model to use for a particular mission with known accuracy and speed constraints.

This section seeks to answer two question: first, "when ought dielectrics be modeled?" and second, "how can dielectrics be modeled in MSM?". The first question is answered through an analysis of the mutual dielectric capacitance, and by including and neglecting dielectrics for certain models. For the four spacecraft analyzed, two of them do not need to have their dielectric components modeled. In fact, including them makes the solution worse. For the other two, ignoring

dielectrics can lead to errors in the E field of 100s of percent. The mutual dielectric capacitance analysis provides the tools to extend this to other spacecraft than the four analyzed.

The second question is answered by using a point charge model for the dielectric portions of the spacecraft. When optimizing the full model, the points are included, but not allowed to be varied and 3 datasets that include a conductor only, mixed, and dielectric only case are included. Constraints can help enforce the far-field behavior without hurting the overall performance for some models, but the constraints are not always compliant for all models and all spacecraft. When optimized without any constraints, the predicted E field only differs from the truth model by less than 10%, often less than 1%. The conductor solutions are the most accurate, with the 1c5d and 3c3d following behind. Overall, modeling dielectrics using MSM is feasible and the errors for the cases considered here are less than other errors expected in the system.

Chapter 4

Orbital Effects of Electromagnetic Perturbations

This chapter uses the voltages, force, and torques of the previous chapters to study the effects of these charging-induced forces and torques on spacecraft orbits. Once again, these effects are for either the electrostatic tractor and for uncontrolled HAMR debris.

4.1 Charged Debris Effects

Früh et al. were the first to model the electrostatic charging effects on HAMR objects [2] such as shown in Fig. 4.1. This initial work adds the Lorentz force and eddy torque to the more standard list of perturbations for an HAMR plate. Including these two new effects changes the orbit by nearly a tenth of a degree in inclination and 0.002 in eccentricity after only 12 hours. Paul et al. [15] modeled a sphere for which torques are not included and found much less dramatic results.

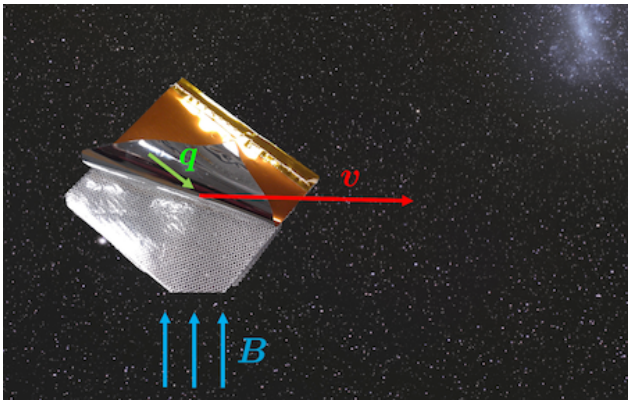

Figure 4.1: Sheets of Multi-Layer Insulation can be perturbed by electromagnetic effects

The first published work in this study is [16] which investigates under what conditions electromagnetic effects need to be considered, and how they impact the orbital motion. This is done by first analytically analyzing the magnitudes of different perturbations for a charged sphere, then using different propagators for a geometrically complex object and analyzing the dynamics. Then a Monte Carlo analysis over attitude is performed to investigate how significant these electromagnetic perturbations are in comparison to the natural spread over attitude. Lastly, the objects and orbit scenarios are found for which electrostatic torques are the most significant. The key result from this paper is that electrostatics influence the orbit not through the Lorentz force, but rather through the Lorentz and Eddy torques which change the attitude. The attitude modulates SRP, which is strong enough to change the orbit significantly.

The next development in charged debris perturbations is [17] which uses a higher fidelity charging model built from empirical fluxes to better estimate the voltage as a function of Local Time (LT) and Planetary K index (K_P). It also includes the convective E field which has been ignored in prior work. From a dynamics perspective, this is a significant change because the voltage–and therefore all voltage-induced force and torques–are functions of time. Further, a much more rigorous Monte Carlo analysis is performed which compares the relative effects of attitude uncertainty with electromagnetic effects on the final position. Because this Monte Carlo analysis is more informative to that in [16], only the later one is presented here.

4.1.1 Orbital Impact Considering Only Charging

Charging combines with Earth's magnetic field to create an electrostatic force and torque. In this section, only the electrostatic force (Lorentz force) is considered from the perspective of orbital element changes and the maximum magnitude of acceleration, as torques have no direct effect on the orbital motion. Prior work has postulated if such Lorentz forces on their own could cause significant perturbations [19]. Thus, this subsection estimates the maximum perturbations that can be expected from natural charging. In this analysis a constant voltage of -30 kV is used, even though it will likely change with local time due to changing plasma conditions.

Consider the example case of a charged aluminum sphere in geosynchronous orbit inclined by 16° subjected only to the point mass gravity of the Earth, SRP, and the Lorentz force. For SRP, assume the cannonball model with full absorption. For the calculation of the Lorentz force, assume the magnetic field points due north with a strength of 100 nT, and that the inclined orbit gives a relative velocity of 1 km/sec and that the sphere is charged to -30 kV. 100 nT is a good ballpark number for the strength of the magnetic field at GEO, -30 kV is a worst case number, and the relative velocity comes from the inclined orbit having velocity components different than the co-rotation velocity ($\Delta v = v\sin(i) = 3.2$ km/sec $\sin(16°) \approx 1$ km/sec). As the sphere changes size, its area to mass ratio changes as do the acceleration due to Lorentz forces.

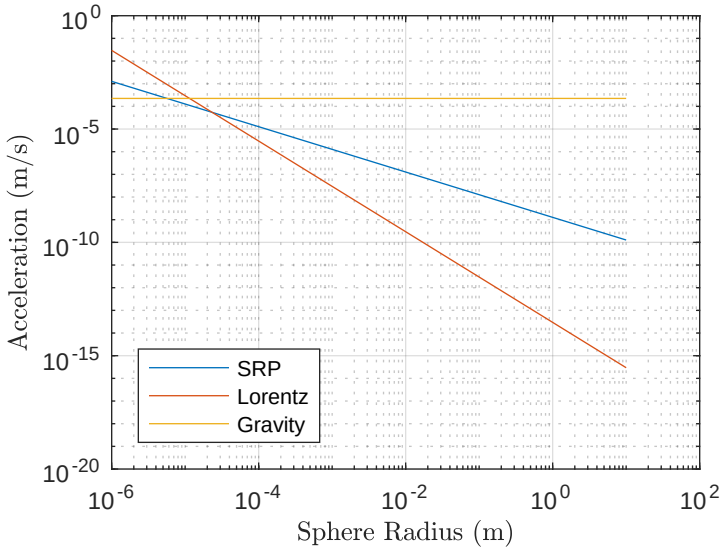

Figure 4.2: Accelerations of an aluminum sphere as a function of size

The acceleration of the aluminum sphere due to these three perturbations as a function of its size is shown in Fig. 4.2. As expected, the acceleration due to gravity is constant with respect to the object size. The force from SRP grows with the square of the radius, and the Lorentz force grows linearly with the radius, but the mass grows as the cube of the radius. This means that the SRP acceleration decays as $1/r$ while the Lorentz acceleration decays as $1/r^2$. Because of this, Lorentz forces are more significant when the object is small, as can be seen in Fig. 4.2.

For the situation modeled here, charging is as significant as SRP for sphere with $r \sim 20\mu$m and charging is the dominant acceleration for spheres smaller than 10 μm. For larger spacecraft with $r \sim 1 - 10$m, gravity dwarfs SRP, which dwarfs charging. For more conservative charging levels, the sphere must be even smaller for charging to matter. This analysis shows that Lorentz forces only impact dust-sized object in a significant manner. For larger objects as spacecraft or spacecraft components such as torn-off Mylar these electromagnetic forces are exceeding small and have a negligible impact. However, the impact of electromagnetic perturbations does not end here. The next section investigates the impact of electromagnetic torques along with other perturbations.

4.1.2 Numerical Propagation of Nominal Case Including Charging

4.1.2.1 Perturbations Considered

Numerous perturbations due to Earth, moon, sun, solar pressure, electrostatics and Eddy current influence the orbits of HAMR objects at GEO. Each perturbation considered is detailed in Tab. 4.1 with either the exact equation or a short description.

Table 4.1: Forces and Torques acting on Space Debris

Perturbation	Force	Torque
Earth gravity	Spherical Harmonics up to 4th order	$\boldsymbol{L} = \frac{3\mu}{R_c^5}\boldsymbol{R}_c \times [I]\boldsymbol{R}_c$
Lunar gravity	point-mass gravity	0
Solar gravity	point-mass gravity	0
SRP	Absorptive, specular, and diffuse reflection	$\boldsymbol{L} = \boldsymbol{r}_{\text{sep}} \times \boldsymbol{F}_{\text{SRP}}$
Electrostatic	$\boldsymbol{F} = Q\boldsymbol{v} \times \boldsymbol{B}$	$\boldsymbol{L} = \boldsymbol{q}_{\text{sep}} \times (\boldsymbol{v} \times \boldsymbol{B})$
Eddy Currents	0	$\boldsymbol{L} = ([M](\boldsymbol{\omega} \times \boldsymbol{B})) \times \boldsymbol{B}$

Eddy current torque is included as well. When a conductor spins in a magnetic field, the mobile electrons move in loops because of induction. No net force is felt because the current path is closed, but an eddy current torque is felt. Gomez recently developed a general method for calculating this torque [56] through

$$\boldsymbol{L} = ([M](\boldsymbol{\omega} \times \boldsymbol{B})) \times \boldsymbol{B} \tag{4.1}$$

where $[M]$ is the magnetic tensor. For a flat plate, the matrix $[M]$ is given by

$$[M] = C_T \frac{\sigma e}{4} \boldsymbol{n}\boldsymbol{n}^T \tag{4.2}$$

where σ is the conductivity, C_T is a constant dependent on shape and size, and $\boldsymbol{n}$ is a unit vector normal to the plane. For a rectangle with length l greater than width w, C_T is found using St. Venant beam theory:

$$C_T \approx \frac{lw^3}{3(1 + 1.38(\frac{w^2}{l^2})^{1.6})} \tag{4.3}$$

in the cases considered, the normal axis of the plate is $\hat{\boldsymbol{z}}$ which makes the torque equal to

$$\boldsymbol{L} = ([M](\boldsymbol{\omega} \times \boldsymbol{B})) \times \boldsymbol{B} = C_T \frac{\sigma e}{4} (\omega_1 B_2 - \omega_2 B_1) \begin{bmatrix} B_2 \\ B_1 \\ 0 \end{bmatrix} \tag{4.4}$$

It is interesting to note that if the plate is spinning about its axis of maximum inertia, ω_3 will be large and ω_1 and ω_2 will be small or zero. The eddy torque will also be small, and the object's spin will be relatively unaffected. If the object is tumbling, only the spin rates about the body 1 and 2 axes are removed and it will eventually fall into a stable spin about its axis of major inertia.

The magnitude of the SRP force is determined by the solar flux and the illuminated area. The direction is governed by the amount of light that is absorbed and reflected specularly and diffusely. The SRP force is given by [132]:

$$\boldsymbol{F} = p_{SRP} A \cos(\theta) \left[\rho_A \hat{\boldsymbol{s}} + 2\rho_s \cos(\theta) \hat{\boldsymbol{n}} + \rho_d (\hat{\boldsymbol{s}} + \frac{2}{3} \hat{\boldsymbol{n}}) \right] \tag{4.5}$$

Where θ is the angle between the sun-pointing line and the face normal, $\hat{\boldsymbol{s}}$ is the sun-pointing vector, $\hat{\boldsymbol{n}}$ is normal to the plane, and $\rho_A, \rho_S,$ and ρ_D are the absorptive, specular, and diffuse coefficients, respectively, which must sum to unity.

4.1.2.2 Magnetic Field Models

Earth's magnetic field at low altitudes is well approximated by the IGRF model, which takes many factors affecting Earth's geodynamo into account. Outside Earth's magnetosphere, the

magnetic field is purely a function of space weather and has little to no dependence on Earth's own magnetic field. At GEO, these two effects combine to make a complex function of time and space weather parameters. The current state of the art for modeling this field is the Tsyganenko model [133]. There have been many versions and updates to this model, but in this analysis the 2001 version is used with GEOPACK 2008[1] for coordinate transforms.

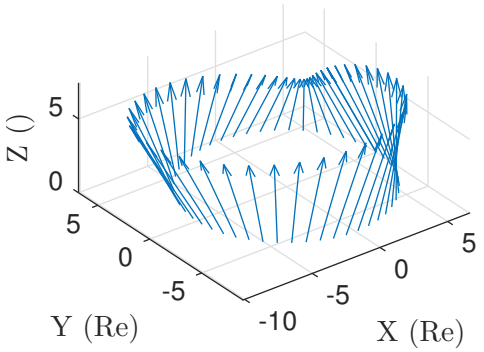

Figure 4.3: ECI Magnetic field used in this study, Z axis is arbitrary

Since the magnetic field is position dependent, the model is run at each timestep. The time is assumed to be January 1, 2002, midnight, for all runs. The space weather parameters used are shown in Tab. 4.2, and are representative values that are used by the Community Coordinated Modeling Center (CCMC) on their single-run website[2]

This produces a magnetic field model that accounts for the solar wind and Earth's geodynamo and is shown in Fig. 4.3 for January 1, 2002 with the parameters shown above. The field is not well-modeled by a tilted dipole, but is dented and kinked due to the solar wind. The x and y axes are in earth radii, and the z axis is arbitrary. Space weather will have a dramatic effect on the charging and the magnetic field strength and direction.

The voltage of a conducting sheet is perhaps one of the easier spacecraft charging problems one could pose, nonetheless it is a still a hard problem. The voltage was modeled under very harsh charging conditions by Früh et al. in [2] for a sheet with one side conducting and one of different dielectrics such as Kapton and Mylar. The most extreme voltage found was slightly more

[1] http://ccmc.gsfc.nasa.gov/modelweb/magnetos/tsygan.html
[2] http://ccmc.gsfc.nasa.gov/requests/instant/tsyganenko.php

Table 4.2: Space weather parameters used for Tsyganenko model

Parameter	Value
Solar Wind Dynamic Pressure	4 nPa
Solar Wind Velocity	400 km/s
IMF B_y	6 nT
IMF B_z	-5 nT
DST	-30 nT

negative than -30 kV and occurred when using the very high ATS-6 flux. In this analysis, a simple and constant value of -30 kV is used to give a rough maximum for the charge level. In many circumstances, the voltage would be much less extreme.

4.1.2.3 Self Capacitance Estimation for Rectangular Plates

Calculating the self capacitance of a square plate is a well-studied problem. J.C. Maxwell himself estimated it to be 0.40 pF for a 1 cm square [112], and current computation methods now estimate it at 0.4019 pF [134]. The self capacitance of two geometrically similar objects, will scale linearly with any dimension. For instance, the self capacitance of a sphere is given by $C = 4\pi\epsilon_0 R$. For a flat plate, capacitance can be expressed as $c = C/B$ where C is the true capacitance of the plate in Farads, and B is the length of the bigger side of the plate in meters. For a square plate B is just the edge length.

Reitan and Higgins [128] produced a very useful curve from which c can be extrapolated from the aspect ratio of the big to small side B/S. Ten points are read off this curve, and a power law is used to fit it with good accuracy ($r^2 = 0.9995$). The power law is shown below.

$$c = \left(0.402 * 10^{-10} \frac{\mathrm{F}}{\mathrm{m}}\right)\left(\frac{B}{S}\right)^{-0.4733} \tag{4.6}$$

The capacitance is used to convert the voltage, which can often be estimated from space weather parameters and is assumed to not depend on size or shape, to the charge. The amount of charge will dictate the magnitude of the force.

4.1.2.4 Numerical Propagation of Nominal Case

A nominal case of a thin rigid square of mylar is considered first. The material parameters are shown in Tab. 4.3. The inertia tensor is computed assuming constant density. The center of charge is separated from the center of mass by $\boldsymbol{r}_{\mathrm{CC}}$ while the center of pressure, which is used for SRP, is separated from the center of mass by $\boldsymbol{r}_{\mathrm{CP}}$. Any matrix values not explicitly defined are zero. The initial state of the plate are that its initial attitude is aligned with the ECI frame, and it's initial rate is zero. The initial orbit elements are $a = 42164$ km, $e = 0.001, i = 16°, \Omega = 0, \omega = 242.3213°, \nu = 0$.

Table 4.3: Nominal HAMR propagation values [1, 2]

Parameter	Value
thickness	1/4 mil (6.35 μm)
density	1.39 g/cm^3
L_x	10 cm
L_y	10 cm
C	4.02 pF
$\boldsymbol{r}_{\mathrm{CC}}$	$[2, 2, 0]^T$ cm
$\boldsymbol{r}_{\mathrm{CP}}$	$[2, 2, 0]^T$ mm
$\boldsymbol{\chi}_S$	$80.43 * [1, 1, 0]^T$ fF m
$\chi_A(1,1)$	$5.393 * 10^{-11}$ F m^2
$\chi_A(2,1), \psi_A(1,2)$	$1.711 * 10^{-14}$ F m^2
$\chi_A(2,2)$	$1.613 * 10^{-12}$ F m^2
ρ_A	0.5
ρ_S	0.2
ρ_D	0.3
σ_C	3.5*10^7 S/m
$M_{3,3}$	333.12 Sm^4

Four different models are used to propagate the orbit of the plate. The longitude and altitude departure over time are shown in Fig. 4.4. Model 1 is the full model, model 2 neglects electrostatic force and torque, model 3 additionally neglects eddy torques, and model 4 additionally neglects attitude-dependent SRP and uses a cannonball model. The orbits for each of these propagators all start at the same place, with no altitude departure and 241° longitude. By the end of the 48 hour propagation, the full model predicts a location that is 1441 km away from the model that neglected

only statics, 2351 km away from the model that neglected statics and eddy torques, and 3354 km away from the model that neglected all electromagnetic effects and used cannonball SRP.

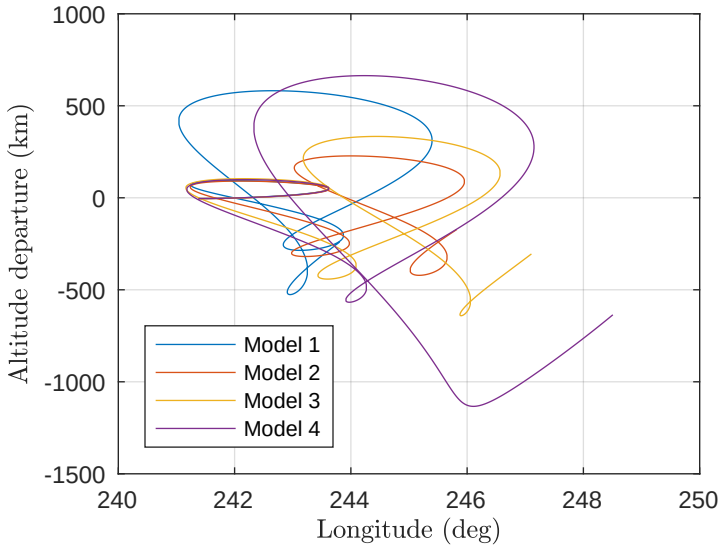

Figure 4.4: Longitude and altitude for plates with different propagation models

The analysis considering only charging predicted very small displacements from electrostatic effects, but Fig. 4.4 shows thousands of kilometer departures caused by including electrostatic and eddy effects. To investigate how such small forces and torques can cause such a drastic change in the orbital position, the magnitudes of the linear and rotational accelerations are now investigated. For the full propagator model, the norm of the linear and rotational accelerations are shown in Fig. 4.5.

As is expected for a circular orbit, the linear acceleration from Earth's gravity stays constant. The SRP acceleration is heavily attitude dependent and changes magnitude quickly as the plate tumbles, but is still by far the largest perturbation. Solar and Lunar gravity change slowly as the distance to the plate changes. The electrostatic force is the smallest by many orders of magnitude.

As for the torques SRP is still the largest, but is followed more closely by electrostatic and eddy torques while the gravity gravity gradient torque is many orders of magnitude smaller. Electrostatic and eddy torques cause rotational accelerations near 1 Radian per hour^2, which means

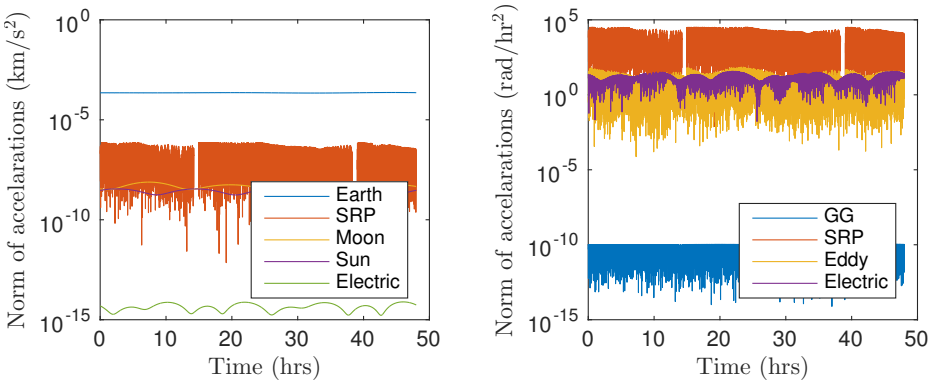

(a) Linear Accelerations (b) Angular Accelerations

Figure 4.5: Accelerations for charged HAMR object during propagation

that in one hour they could change the attitude by 1/2 a radian if they acted in the same direction using $\Delta\theta = \frac{1}{2}\ddot{\theta}\Delta t^2$. This is the key to how electrostatic and eddy effects can change an orbit so drastically — over time periods longer than a few hours, electrostatic and eddy torques can significantly change the attitude of a HAMR object, which changes SRP, which changes the orbit.

This matches the findings of other authors as well. Früh et al [2] found that including eddy torques for a thin HAMR object caused major orbital differences, but Paul et al. [15] modeled a sphere for which torques do not act and found minimal orbital differences. The Lorentz force cannot change the orbits of objects large enough to be observable. However electrostatic and eddy torques can change the attitude, and if the attitude influences SRP, the orbit can be measurably changed.

4.1.3 Comparison of Torques for General Objects

SRP is the driver for HAMR objects, but it can be steered by electromagnetic torques. This subsection investigates what objects are susceptible to such electromagnetic torques. First consider the same 10 cm square plate considered in previous analysis, but allow the voltage to vary. If the plate is uncharged electrostatics will no longer act, and earlier analysis shows that at -30 kV it does matter, but is there a charging threshold where electrostatics begin to contribute? To answer this question, the voltage of the plate is varied logarithmically from 10 Volts, which is a normal floating

potential, to 100 kV, which is slightly higher than the worst case charging ever modeled. [135]. The plate's orbit is propagated for 24 hours, and the torques are recorded. The angular acceleration that the plate experiences due to each perturbation is shown in the log-log plot in Fig. 4.6. The linear accelerations are not shown because the orbit change comes from electromagnetic torques reorienting the plate which changes SRP.

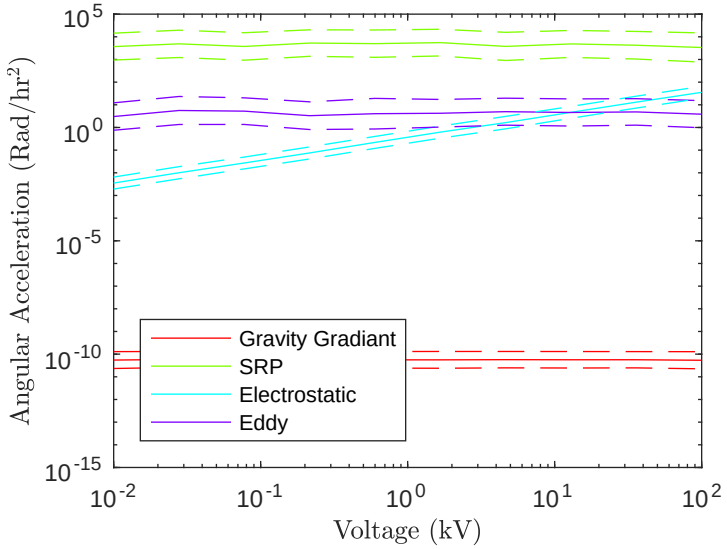

Figure 4.6: Angular accelerations due to various perturbations at different voltages

Since all of the torques are attitude dependent, they vary quickly through time as the plate tumbles. To give a sense of the normal variation, the mean and 1-σ bounds are shown. Because many of the torques are logarithmically distributed, the standard deviation is larger than the mean, and does not apply for a non-symmetric distribution. Rather, the logarithms or the angular accelerations are used to make the statistics, then exponentiated for plotting. This is shown below:

$$x' = \log(x) \rightarrow \quad \bar{x} = 10^{\bar{x'}} \tag{4.7}$$

$$\rightarrow \bar{x} \pm \sigma_x = 10^{\bar{x'} \pm \sigma_{x'}} \tag{4.8}$$

The torques from gravity gradients, SRP, and eddy currents are all relatively constant with voltage, which would be expected. However, the torque from electrostatics rises steadily. If 1 radian is used as an arbitrary marker of a significant attitude change, the time scales on which electrostatics will

act can be investigated. For 10 Volts, the mean angular acceleration is 3.5e-3 Rad/hr^2. Using $\Delta\theta = \frac{1}{2}\ddot{\theta}\Delta t^2$ gives a time scale of 23.8 hours. At 600 Volts, the time needed for significant attitude perturbations is 3 hours, and at 100 kV it only takes 14 minutes. Of course this assumes the torque is always about the same body axis, which is not always true but gives a convenient upper bound.

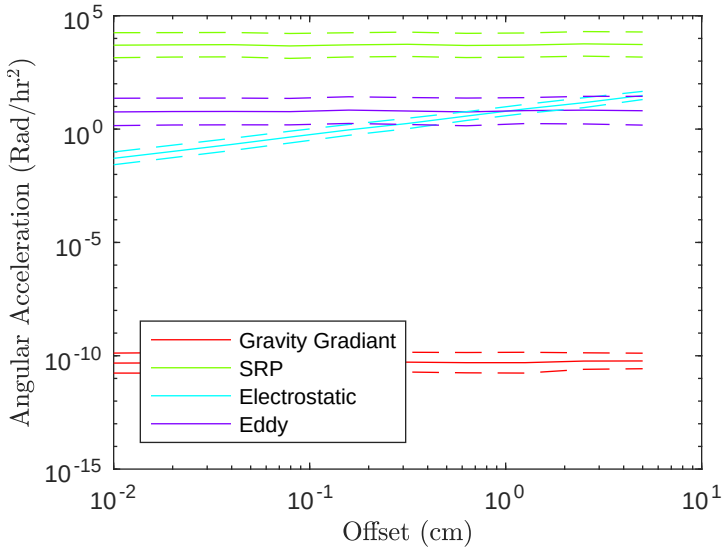

Figure 4.7: Angular accelerations due to various perturbations at different CM offsets

This same analysis is repeated varying not voltage but the separation between center of charge and center of mass while the voltage is fixed at 30 kV in Fig. 4.7. Once again all perturbations except electrostatics are relatively constant, while electrostatic torques grow with the separation, as this lengthens the moment arm. Electrostatics become larger than eddy currents for all offsets larger than 1 cm on this 10 cm square plate, although the variance associated with eddy currents is much larger. Once again using 1 radian as a threshold for significant attitude perturbations that could influence the orbit gives timescales on which charging can act. At 0.1 mm of offset, electrostatic torques will take nearly 6 hours to significantly change the attitude, at 1.5 mm, the timescale is 1.5 hours, and at 5 cm (half the length of the plate), electrostatics have a timescale of only 16 minutes.

Next consider the same thin 10 cm sheet but hold the voltage, separation of center of charge

and center of mass, and thickness constant, but allow the initial spin to vary. The initial spin in all prior work is set to zero, but in this section the stability of spinning about an axis of maximum inertia is considered. Intuitively, a frisbee or football will be less susceptible to small torques that would otherwise cause it to tumble if it were spinning faster. Likewise, the thin plate will be less susceptible to small electromagnetic torques if it were spinning stably about its axis of maximum inertia, which is the body z axis.

To study this, consider a plate spinning like a frisbee about its z axis at a rate of ω_0. Apply a torque about the body x axis of $L_x = \chi_S V B \Delta v = (1.1376 * 10^{-13}$ C m)(30kV)(100nT)(1km/s) = $3.4127 * 10^{-13}$ Nm for one hour, then propagate normally for another hour. The angle between the body z axis and the inertial z axis (which are aligned at the beginning of the simulation) is plotted below in Fig. 4.8 for a fast initial spin ($\omega_0 = 2°/s$) and a slow initial spin ($\omega_0 = 0.1°/s$). Keep in mind that with no initial spin, this problem becomes 1 dimensional, and after one hour of torque the place should have rotated by $\Delta\theta = \frac{1}{2}\frac{L_x}{I_x}\Delta t^2 = 1723°$, nearly 5 entire rotations.

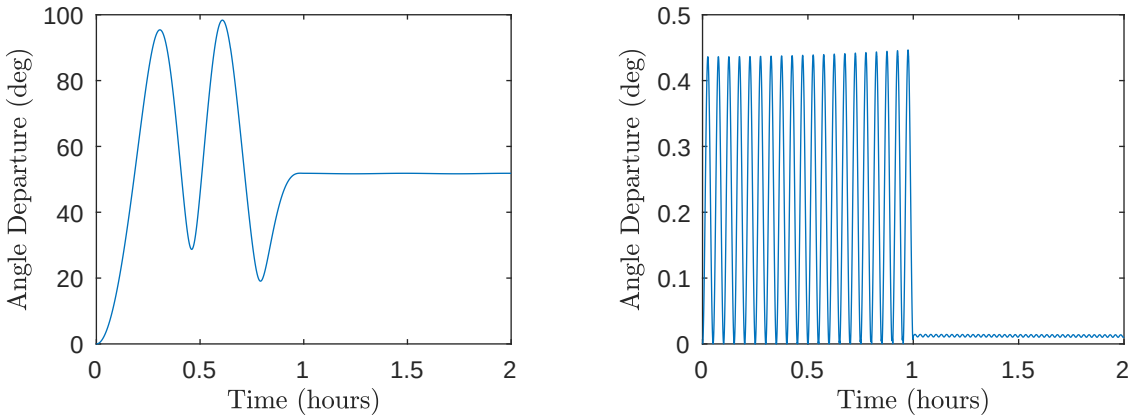

(a) Slow initial spin – $\omega_0 = 0.1°/s$

(b) Fast initial spin $\omega_0 = 2°/s$

Figure 4.8: Departure from initial sun-pointing angle due to electrostatic torques

From this simple example the importance of initial spin can be seen dramatically. If the initial spin is a slow 0.1 degrees per second, one hour of electrostatics can change the body attitude, which changes SRP, by 50 degrees. If the initial spin is increased to 2° per second, the same electrostatic torque only changes the sun pointing angle by a mere 0.01 degrees. Clearly objects spinning stably

about the axis of maximum inertia are less susceptible to small electrostatic or eddy torques. As an aside, eddy torques never act about the z axis for plates of vanishing thickness, so they are not able to change the attitude, and therefore the orbits, of thin plates spinning about their maximum inertia axis.

To further investigate the trend illustrated above where objects spinning stably are less susceptible to small torques, vary the initial spin logarithmically from 0.01 to 10 degrees per second and monitor the attitude departure. The attitude is monitored by computing the mean and standard deviation of the angle between the body and inertial z axis in the second hour, after the electrostatic torque has been turned off. This is shown in Fig. 4.9

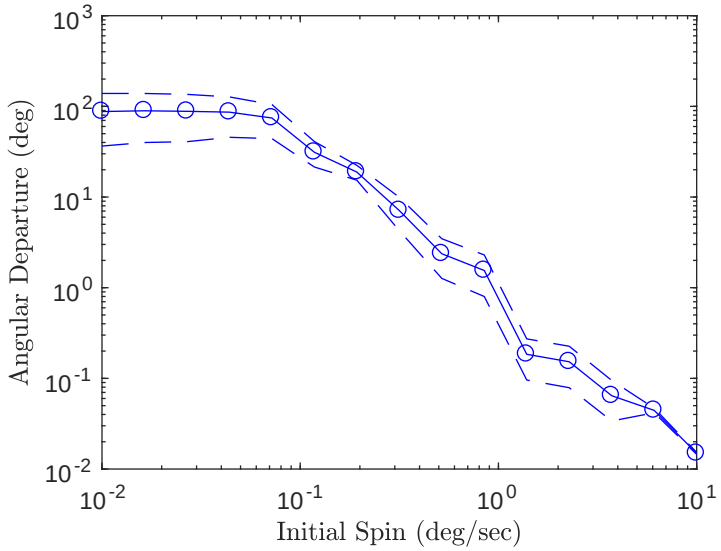

Figure 4.9: Influence of initial spin on attitude departure

The mean attitude departure in the second hour is shown as the solid line with the circles and the dashed lines show the 1-σ bounds. When the plate has a low initial spin, (0.01 - 0.1 °/s per second), the departure is a nearly flat line, because the body z axis can never be more than 180° from the inertial z axis. For higher initial spin rates ($\omega_0 > 0.1$ °/s per second), the departure angle drops quickly. Choosing again the arbitrary marker for significant attitude change of 1 radian ($\sim$ 57°) gives a cutoff spin rate past which electrostatic torques may not have as much influence on

the orbit of 0.085 °/s per second.

Keep in mind that in this simulation the electrostatic torque is assumed to act completely in the body x axis and be constant. This is not likely in the full coupled problem. Additionally, these results hold only for the 10 cm by 10 cm by 1/4 mil sheet of mylar charged to 30 kV. Heavier and less dramatically charged objects will require smaller stable initial spins to overwhelm the electrostatic torques.

For the thin cases considered earlier, SRP is very sensitive to attitude – if the plate is directly facing the sun the acceleration is thousands of times larger than if the plate faces orthogonal to the sun. For a cube, the attitude only changes the exposed area by a factor of 2 or 3. This shows that objects like plates with highly attitude-dependent cross-sectional are more susceptible to the small torques caused by electrostatics and eddy currents. Additionally this heavier object will be less susceptible to non-gravitational perturbations like electrostatics and SRP.

To explore this, consider the same 10 cm square of Mylar, but allow the thickness to vary from the very thin 1/4 mil (6.35 μm) to 10 cm which turns the sheet into a solid cube of Mylar. As this 10 cm cube weighs 1.39 kg, this is a good approximation of a cubesat. Each of the sheets are propagated for 24 hours, and the linear and angular accelerations are recorded at each time, much like the results shown in Fig. 4.5. The mean and standard deviation are computed for the time-series of the accelerations for each plate thickness and are plotted in Fig. 4.10. The means are plotted as solid lines, and the $1-\sigma$ bounds are shown as dashed lines. In some cases the standard deviation is larger than the mean, and the lower bound of the norm is negative and does not appear on this log plot.

There are many interesting trends in both plots. Considering linear accelerations, the gravitational accelerations are constant with object size. This is expected as mass divides out of the gravitational formula. The non-gravitational accelerations (Lorentz force and SRP) decrease as the plate gets thicker because the force stays roughly constant (the full 3-dimensional SRP calculation is performed, but the self capacitance is assumed to stay constant even though the plate becomes thicker). The Lorentz force is consistently the smallest perturbation, and is nearly 10,000 times

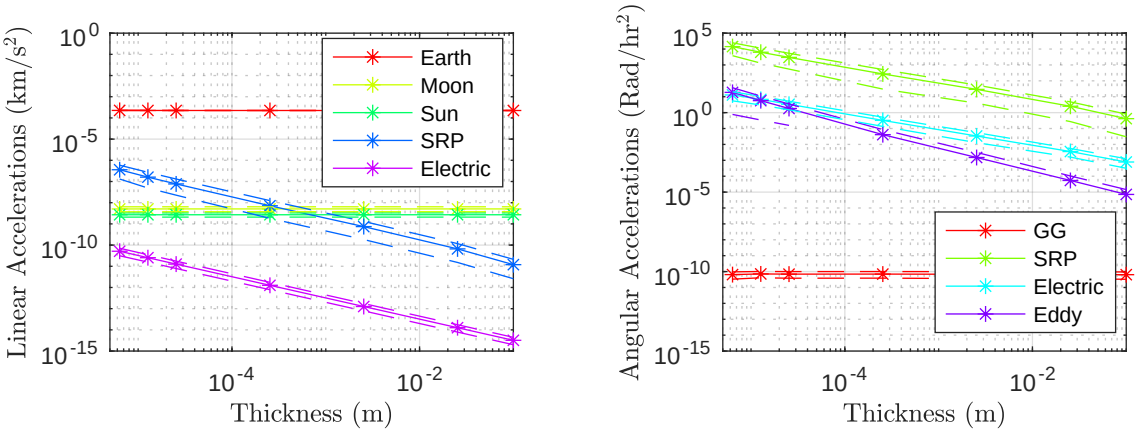

(a) Linear Accelerations

(b) Angular Accelerations

Figure 4.10: Acceleration on plates of varying thickness from different perturbations

smaller than SRP. This will not have a large effect on propagation. For the angular accelerations, gravity gradient accelerations remain constant, as both the torques and the inertia increase as the plate gets thicker. All other accelerations become smaller because of the increasing inertia. SRP is the largest torque, but is followed by electrostatics and eddy torques. Eddy torques have a more negative slope than electrostatics – this is an indirect effect due to the thicker plates spinning up to lower rates, which causes the eddy torques to decrease.

For large heavy objects, the torques will take much longer to change the attitude and "steer" SRP. Furthermore, these objects will not change their exposed areas as much due to rotations, which further suppresses the orbital effects of electromagnetic torques. For small lightweight objects, the small electromagnetic torques can drastically change the orbit by changing the attitude.

4.1.4 Section Conclusion

There are many perturbations which influence the orbit of GEO objects. This section develops the models needed to include electrostatic perturbations for GEO objects, investigates how these perturbations change the orbit, and analyzes the objects and orbit scenarios where electrostatic and eddy perturbations will be the most significant and ought to be considered.

For a spherical object, the Lorentz force is insignificant for objects larger than 100 μm

in diameter, as gravity and SRP dominate. For non-spherical objects, the weak torques from electrostatic and eddy effects can change the attitude, which changes the strong perturbation of SRP. This allows the weak electromagnetic perturbations to steer the strong SRP perturbation and change the orbits of objects large enough to be observed. Including these electromagnetic effects can change the final position after 2 orbits by thousands of kilometers, and cause significant differences in a 24 hour Monte Carlo over initial attitude.

The objects that are the most susceptible to these small electromagnetic torques are investigated by comparing to a nominal HAMR sheet of Mylar charged to 30 kV, having a 2.82 cm offset between the center of mass and center of charge, and no initial spin. Holding all else constant, electrostatics will begin to significantly contribute for voltages higher than a kilovolt, or separations larger than a millimeter. Even if these small electromagnetic torques can change the attitude in a short time, this will only translate to large orbit changes if the area exposed to SRP changes dramatically because of this attitude change as it does for a thin plate. The inertia and mass also change as the thickness of a plate grows, and increase the time needed for electromagnetic torques to take effect. Lastly the initial spin rate about a stable axis is found to reduce the effect of electrostatics. For the object considered here, spins faster than 0.1 °/s per second are found to overwhelm electrostatics on the time period of an hour.

From this, it is concluded that electrostatics can significantly impact the orbits of some objects. Likely candidates for which charging will matter are either tiny objects for which the Lorentz force will contribute, or thin sheets where small electrostatic and electromagnetic torques can "steer" SRP. For these small torques to matter, the object must be highly charged, have its center of charge offset from its center of mass, and not be spinning quickly about a stable axis.

4.2 Statistical Charged Debris Effects

The prior section showed that the objects most likely to be affected by electromagnetic effects are thin sheets with very attitude-dependent SRP force and torque. However, for these objects, almost *any* perturbation or initial attitude uncertainty is very significant. This section compares

initial attitude uncertainty with electromagnetic perturbations. Rather than assuming a constant voltage of -30 kV, the voltage is computed using statistical fluxes at both $K_P = 2-$ and $K_P = 8$ and are shown in Chapter 2.4.2. Another change from [16] is the inclusion of the electric field.

4.2.1 Electric Field Models

The co-rotation and convection electric field both contribute to electric perturbations. The co-rotation field uses the Tsyganenko model discussed above for the magnetic field and the Volland-Stern [136, 137] model for the convection E field as presented in [138] which gives the voltage of a point in space as:

$$V = -bL^{\gamma}\sin(\phi) \tag{4.9}$$

Where b is a constant, γ is a constant, and $L = \frac{r/Re}{\sin^2(\theta)}$ is the magnetic L shell and ϕ is the magnetic local time referred to noon rather than midnight. The angle θ is the magnetic colatitude, which is measured downwards from the magnetic north pole. In this work $\gamma = 2$, and $b = 45$ V$/(1 - 0.159K_P + 0.0093 * K_P^2)^3$ is the overall strength as a function of K_P index [139]. To find the colatitude, first transform into the geomagnetic frame [140] which has it's 3rd axis aligned with Earth's north magnetic pole, then take the inverse cosine of $r(3)/||r||$. To find ϕ, project the satellite and sun position into the geomagnetic $x - y$ plane and find the angle with respect the the x axis for both and subtract them to find ϕ.

To find the E field, take the gradient in spherical coordinates $\boldsymbol{E} = -\nabla V$:

$$\boldsymbol{E} = -\nabla V = -\frac{\partial V}{\partial r}\hat{\boldsymbol{r}} - \frac{1}{r}\frac{\partial V}{\partial \theta}\hat{\boldsymbol{\theta}} - \frac{1}{r\sin(\theta)}\frac{\partial V}{\partial \phi}\hat{\boldsymbol{\phi}} \tag{4.10}$$

$$= \frac{V}{r}\bigg(- \gamma\hat{\boldsymbol{r}} + 2\gamma\cot(\theta)\hat{\boldsymbol{\theta}} - \csc(\theta)\cot(\phi)\hat{\boldsymbol{\phi}}\bigg) \tag{4.11}$$

Where $\hat{\boldsymbol{r}}$ points outward, $\hat{\boldsymbol{\theta}}$ points southward (magnetically, not geographically), and $\hat{\boldsymbol{\phi}} = \hat{\boldsymbol{r}} \times \hat{\boldsymbol{\theta}}$.

This potential and the electric field are shown in GSM coordinates below in Fig. 4.11a for $K_P = 3$. In the figure, the length of the arrow represents the field strength with 1 axis unit

representing 2 mV/m. The field is points from dawn to dusk as expected. At this low K_P level the average field strength is 0.434 mV/m, but if K_P increases to 8 it grows to 2.87 mV/m. Figure 4.11b shows both the Lorentz field ($\boldsymbol{v} \times \boldsymbol{B}$) and the convection E field in the ECI $x - y$ plane for a geosynchronous orbit inclined to 16°. The sun is nearly directly below (negative Y direction) in this figure. Keep in mind that the $\boldsymbol{v}$ is the velocity relative to the magnetic field, which co-rotates with earth and is not aligned with the orbit, thus the Lorentz field is not perpendicular to the orbit. The length of the arrow once again represents the strength of the field at that point, with one axis unit corresponding to 0.1 mV/m for the convection E field or 0.01 mV/m for the Lorentz field.

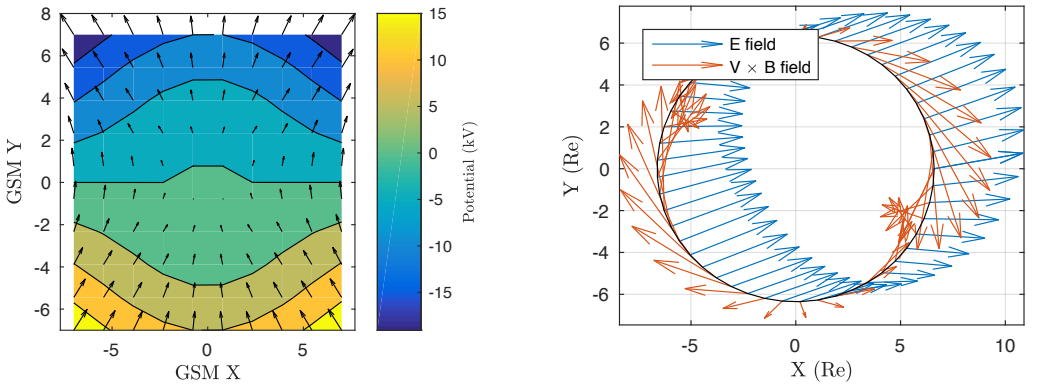

(a) Convection E field in GSM

(b) E and V × B field for inclined GEO orbit

Figure 4.11: Convection E field and Lorentz field comparison for $K_P = 3$

The first thing to notice is that since the length of the vectors are similar, the magnitude of the E field for this orbit is about 10 times stronger than the Lorentz field even at $K_P = 3$ (average magnitude for this orbit of 0.431 mV/m vs 0.036 mV/m), at $K_P = 8$ the difference is even greater since the average E field strength grows to 2.85 mV/m. In all prior work by [2], [15] and [141, 142], the convection E field has been completely ignored in favor of the B field, but it is actually the stronger of the two. In different orbits, specifically one in which there is greater velocity relative to the magnetic field and is closer to Earth, the $\boldsymbol{v} \times \boldsymbol{B}$ field is stronger.

4.2.2 Propagation Model

Consider a small piece of torn off MLI 50 cm by 50 cm like that shown in Fig. 4.12. It is composed of just 3 layers: 2 layers of aluminized mylar 1/4 mil thick with a non-conducting piece of Dacron netting 0.16 mm thick in between. The total mass of this thin sheet is just 6.225 grams, but it's large surface area of 0.25 m^2 gives it an area to mass ratio (AMR) of 40.16 m^2/kg. All MLI parameters are taken from [143]. The center of mass is assumed to be offset from the center of pressure by [2.5, 2.5, 0] cm due to some wrinkling or other imperfection. The center of charge is assumed to be offset from the center of mass by [-2.5, -3.33, 0] cm. The inertia tensor is computed assuming constant density.

Figure 4.12: Multi-Layer Insulation with layers shown

The primary force for macro sized objects in Earth orbit is the Earth's gravity. There are several small forces and torques which perturb the orbits of many small objects such as Solar Radiation Pressure (SRP), Earth's non point mass gravity, and the gravitational pull of the sun and moon. This work includes three new electromagnetic perturbations - the Lorentz force, the Lorentz torque, and Eddy current torques. All perturbations are listed in Table 4.1 with either the exact equation or a short description. This propagation model is the same as the one used in [16] except that it also includes the E field and the voltages change with local time and sun

facing angle. Since the two plates are not electrically connected, one of them is always in the shade and can charge. If there was only one plate, or the two aluminized mylar sheets were electrically connected, it would never charge more than a few volts in the plasma environments considered here.

4.2.3 Propagation Model Results

This HAMR object has an area to mass ratio of 40.16 m^2/kg and is put in an initial orbit with $a = 42,164$ km, $e = 0.0001, i = 16°, \Omega = 0°, \omega = 242.3213°,$ and $\nu = 85.05°$. The true anomaly ν is chosen so that the propagation begins at a local time of 4 hours, which subjects the plate to the most dramatic charging. The initial angular rates are set to zero, and its initial attitude is aligned with the ECI frame ($\boldsymbol{\sigma} = [0, 0, 0]^T$) where $\boldsymbol{\sigma}$ is a Modified Rodriguez Parameter (MRP) to describe the attitude [117]. The orbit is propagated for 24 hours with a 3 second time step using a RK4 integrator, and the resulting altitude departure and longitude are shown in Fig. 4.13a

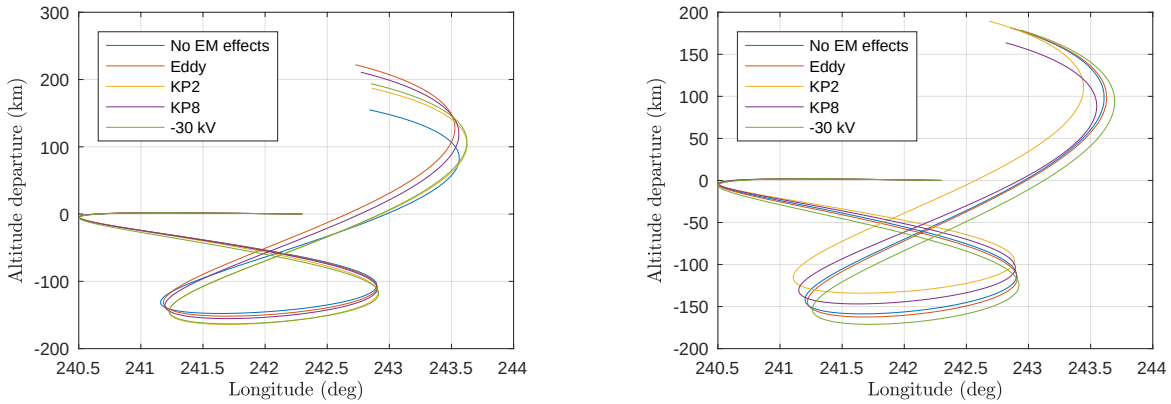

(a) Initial attitude $\boldsymbol{\sigma} = \begin{bmatrix} 0 & 0 & 0 \end{bmatrix}^T$

(b) Initial attitude $\boldsymbol{\sigma} = \begin{bmatrix} 0.2 & 0 & 0 \end{bmatrix}^T$

Figure 4.13: Longitude and altitude departure caused by neglecting perturbations

In an unperturbed orbit, all the tracks would end in the same place as they began. However, they all are a few hundred kilometers higher in altitude, and have traversed over more than three degrees of longitude. For reference, the typical longitude spacing between satellites in GEO is $\sim 0.5°$. At the end of the propagation, all 5 models predict different final positions. Using the

model which only includes gravitational effects and SRP as a reference, including eddy torques gives a final position 109.48 km away. Including just electrostatics at $K_P = 2-$ and $K_P = 8$ gives final position differences of 35.98 and 77.32 km, respectively. Including just electrostatics with a worst case constant voltage of -30 kV yields a final position difference of 40.23 km. These final positions are small numbers when compared to the orbit radius, but correspond to a few tenths of a degree which matters for telescope pointing.

Using these differences in final positions, it would seem that including eddy torques is the most important, since it leads to the largest position difference. Next would be electrostatics at $K_P = 8$, then a constant voltage of -30 kV, then $K_P = 2$. This is quite surprising since the electric disturbances are strongest at -30 kV, not at $K_P = 8$. To further investigate which perturbations cause the largest differences in position, the same propagation is repeated, only changing the initial attitude to $\boldsymbol{\sigma} = [0.2, 0, 0]^T$. Again the altitude departure and the longitude are shown in Fig. 4.13b.

Here the object again follows a curving "figure 8" path, and changes altitude by ∼400 km and longitude by $\sim 3°$. However, the orbits are drastically different from those computed with the first attitude - for instance, the model that ignores all electromagnetic perturbations predicts a final altitude departure of more than 200 km with the first attitude, but less than 200 km with the second attitude. Additionally, the ordering of the relative impacts of the different perturbations is different. Choosing the model which ignores all electromagnetic effects as the reference, including eddy torques leads to a 14.58 km difference after 24 hours, electrostatics at $K_P = 2-$ and 8 lead to differences of 130.38 and 33.85 km, and a constant voltage of -30 kV leads to a final position difference of 62.26 km. While eddy current torque is the most significant at the first attitude, it is the *least* at this attitude. $K_P = 2-$ and $K_P = 8$ switch places, and the constant -30 kV case is now less significant than electrostatics at $K_P = 2-$.

These simulations results illustrate that the initial attitude *and* the propagation model used both have a strong influence on the orbit. Because even the relative ordering of how significant different electromagnetic perturbations are gets re-shuffled, it would appear that the initial attitude and the propagation model are coupled. This is not completely surprising, since the significant part

of the electromagnetic perturbations is the torque, which changes the attitude and "steers" SRP. Either a small torque (such as from electromagnetics) integrated over time, or a different initial attitude results in a different attitude, which changes SRP, which changes the orbit. It is prudent to remember that this behavior is due in most part to the strongly attitude-dependent cross sectional area of this flat plate. A sphere with the same area to mass ratio is nowhere near as sensitive [15].

4.2.4 Statistical Analysis

This subsection looks at hundreds of initial attitudes to find which perturbations are the most significant. Additionally, the effect of including different electromagnetic perturbations is compared to initial uncertainty in attitude. To do this, the same 50 cm plate is propagated either with an initial attitude perturbation, or including electromagnetic perturbations and then compared to a plate that had neither an initial attitude perturbation or electromagnetic perturbations. This is shown schematically in Fig. 4.14.

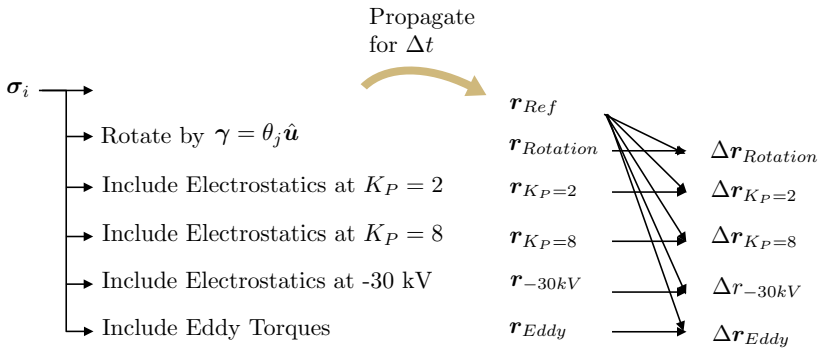

Figure 4.14: Scheme for investigating relative effect of electromagnetic disturbances with randomized initial attitude

For all cases, a plate is put into orbit with the initial orbit elements of $a = 42,164$ km, $e = 0.0001, i = 16°, \Omega = 0°, \omega = 242.3213°$, and $\nu = 85.05°$. The true anomaly ν is chosen so that the propagation begins at a local time of 4 hours, which subjects the plate to the most dramatic charging. A random initial attitude $\boldsymbol{\sigma}_i$ is generated from three uniformly distributed Euler angles. A plate with this attitude is propagated neglecting all electromagnetic effects for a period of time Δt and its final position $\boldsymbol{r}_{Ref}$ is recorded. Next, a perturbation or initial attitude difference is

added. For the attitude difference, a rotation of magnitude θ_j about a randomly selected axis $\hat{\boldsymbol{u}}$ where $\boldsymbol{\theta} = [0.0001°, 0.001°, 0.01°, 0.1°, 1°]$ using the principle rotation vector $\boldsymbol{\gamma} = \theta_j \hat{\boldsymbol{u}}$ and the final position $\boldsymbol{r}_{\text{Rotation}}$ after Δt is recorded. For the perturbations, the plate is not rotated but either eddy torques, electrostatics at $K_P = 2-, K_P = 8$, or a worst-case constant voltage of -30 kV are included in the propagation and the final positions $(\boldsymbol{r}_{K_P=2}, \boldsymbol{r}_{K_P=8}, \boldsymbol{r}_{-30kV}, \boldsymbol{r}_{Eddy})$ are recorded. The electrostatic cases are run without eddy torques included. Finally the difference in final positions between the reference $\boldsymbol{r}_{Ref}$ and the cases that include electromagnetic perturbations or have a different initial attitude are computed $(\Delta r_{\text{Rotation}}, \Delta r_{K_P=2}, \Delta r_{K_P=8}, \Delta r_{\text{Eddy}})$. This process is repeated 500 times varying the initial attitude $\boldsymbol{\sigma}_i$ each time recording the Δr every 15 minutes for 3 hours in a master text file. The 10 cases, run for 3 hours of simulation time, for 500 different initial attitudes gives 15,000 hours of propagation time. The results of this propagation are shown in Fig. 4.15.

The statistics for the effect of an initial attitude difference or including an electromagnetic perturbation are shown using violin plots. Violin plots are a way of looking at multiple histograms at once - the width of the bar represents how many counts are observed in the bin given by the position on the y axis. Violin plots can be thought of as a collection of histograms all rotated by 90°. The different ticks on the x axis represent different cases. For example, consider the 0.0001° case after 3 hours of propagation shown in Fig. 4.15c. The position difference from this initial attitude change is either less than 1 cm, or in the hundreds of meters. Simply reporting the mean or median (shown in red and green, respectively) would lead one to believe that most of the initial attitudes lead to final position differences of ∼1 m, when in reality almost none of them are.

At the 1 hour mark (Fig. 4.15a), including electrostatics with $K_P = 2-$ only causes position differences greater than a meter for very few initial attitudes, furthermore, it is *less* significant than a 0.0001° uncertainty in initial attitude, which is nearly impossible to get from a ground observation for a non-cooperative object. If $K_P = 8$, a significant fraction of the initial attitudes lead to position difference of dozens of meters after only an hour, and including or neglecting electrostatics is equivalent to a little less than 0.001° uncertainty in initial attitude. If the worst

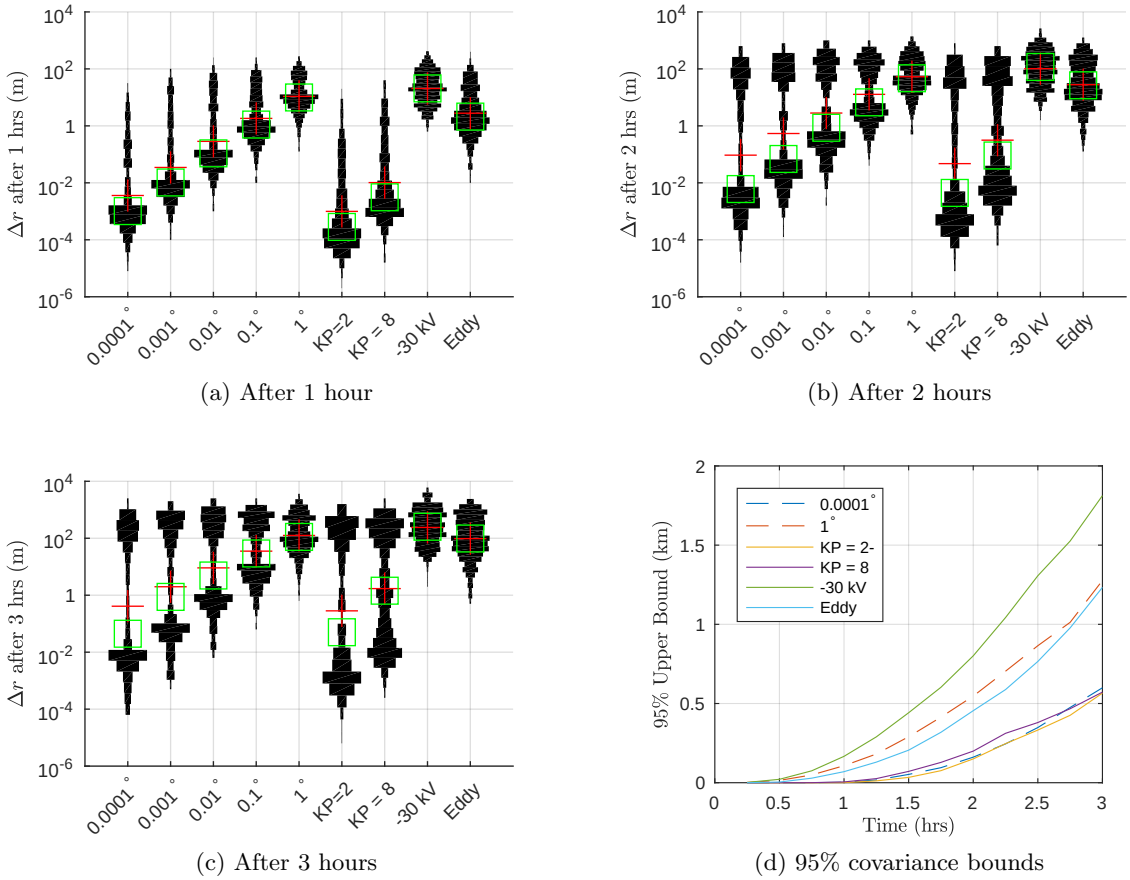

(a) After 1 hour

(b) After 2 hours

(c) After 3 hours

(d) 95% covariance bounds

Figure 4.15: Results of propagation with varied initial attitude or perturbations

case is observed and both sides of the plate are charged to -30 kV, almost all the initial attitudes lead to position differences greater than a meter after only an hour with a few exceeding 100 m. This is more significant than 1° of attitude uncertainty. Including eddy torques also causes a large spread and is comparable to 1° of uncertainty.

Moving to the 2 hour mark of simulated orbit time, the distributions begin to look bi-modal. One population of initial attitudes leads to large position differences greater than 10 meters, while the other leads to much smaller position differences. This may be because some attitudes lead to "runaway" differences while others lead to stable spins about the axis of maximum inertia which are much harder to perturb and change the attitude in a way that affects SRP as discussed in the previous section . It is still the case that electrostatics at $K_P = 2-$ are less significant than

0.0001° of attitude uncertainty, at $K_P = 8$ including electrostatics is roughly equivalent to 0.001° of attitude uncertainty, the worst case is more significant than 1° of uncertainty, and that including eddy torques is similar to 1° of uncertainty.

Moving finally to 3 hours of simulated orbit time, now a very significant portion of all initial attitudes with all perturbations lead to position differences of more than 100 meters. The split between the runaway cases and the others is even more dramatic, causing many of the plots to take on a "dog-bone" shape. Surprisingly, including eddy torques, the -30 kV, and the 1° rotation nearly always causes at least a 1 meter position change, which removes the lower lobe. It is still the case that electrostatics at $K_P = 2-$ are less significant than 0.0001° of attitude uncertainty, at $K_P = 8$ including electrostatics is roughly equivalent to 0.001° of attitude uncertainty, the worst case is more significant than 1° of uncertainty, and that including eddy torques is similar to 1° of uncertainty. The maximum position difference is observed for the worst case -30 kV and is 5.77 km.

It is interesting to look at how the spread from including or neglecting a certain perturbation or attitude uncertainty changes with time. To do this, the 95% upper bound is found for each perturbation/attitude uncertainty at each time. This is done by sorting the Δr, and taking the 475^{th} element since there are 500 entries. This gives an empirical estimate to the 2σ covariance bound that should be associated with the initial attitude uncertainty or the un-modeled perturbations. This covariance bound is plotted in Fig. 4.15d for all the perturbations and the limiting attitude uncertainties of 1° and 0.0001°.

The worst case constant voltage of -30 kV causes the largest covariance, followed by the 1° attitude uncertainty, then eddy torques, then $K_P = 8$, then $K_P = 2-$ and the 0.0001° attitude uncertainty which are similar. All of the perturbations/attitude uncertainties lead to between 0.5 and 2 km covariance after 3 hours, and seem to be accelerating. In the case of a solar storm at $K_P = 8$, the covariance bounds do not need to be drastically changed from the normal ones associated with attitude uncertainty. However, if the worst case charging is maintained, the covariance bounds need to be expanded beyond their normal values. Eddy torques, which act no matter what K_P is,

always cause large covariances.

4.2.5 Section Conclusions

The dynamical motion prediction of a charged HAMR plate with center of pressure offset from center of mass is a very sensitive problem. Without very precise knowledge of all torques on it, and a very precise measurement of the initial attitude, it is difficult to model its motion accurately - including or neglecting these effects can lead to 5.77 km displacements after only 3 hours. It is found that at $K_P = 2-$ electrostatics are less important than 0.0001° of attitude uncertainty, at K_P=8 it's about the same as 0.001°, a constant voltage of -30 kV more significant than 1° and Eddy torques are about equal to 1° of uncertainty. Additionally, the covariance bounds for neglecting these perturbations or attitude uncertainty are between 200 m and 900 m after only 2 hours, and between 0.5 and 2 km km after 3 hours.

This shows that: 1) HAMR objects with highly attitude-dependent area-to-mass ratios are very sensitive. Any un-modeled disturbances or initial attitude uncertainty can lead to 5 km departures after only a few hours. 2) Even in a relatively benign ($K_P = 2-$) charging environment, the covariance bounds for such objects ought to be enlarged significantly to account for Eddy torques in order to track them accurately. 3) If an object charges to a very negative voltage and holds that voltage, the covariance bounds need to be enlarged to account for this un-modeled disturbance. Although the electromagnetic perturbations considered here do not change the orbits in predictable ways because of the attitude and Solar Radiation Pressure coupling, they do change the orbits significantly. Accounting for such perturbations in the form of inflating the covariance is important for tracking such objects.

4.3 Time-Varying Electrostatic Tractor Analysis

The first analysis of the ET in this study is [96]. In this paper, the prospects and challenges of using a pulsed rather than steady state electron beam are investigated. Pulsing the beam introduces many new complexities and a Monte Carlo analysis is performed to investigate which

beams produce the most force. Next, a deterministic equal power analysis is performed at different power levels.

The next study performed is [99] which uses the empirical flux model rather than assuming Maxwellian currents to compute the voltages. Additionally, this analysis moves to slower pulse periods on the order of 100s of milliseconds so that equilibrium solutions can be used. This greatly simplifies the analysis and allows all the charging calculations to be done once and then interpolated for a variety of cases. The time-varying analysis is presented first.

While prior work on the electrostatic tractor performance focuses on a continuous charge emission from the tug, [93, 74, 73] this work augments the ET concept by using a pulsed electron beam rather than a continuous one. Of interest is under what conditions the pulsed charging leads to tractor forces levels that are comparable or greater than the continuous charging case.

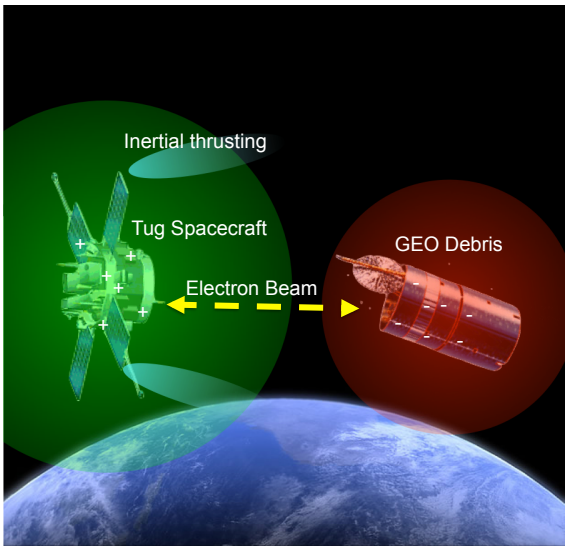

Figure 4.16: The Electrostatic Tractor (ET) allows spacecraft to touchlessly exert forces and torques on passive space objects

The physical explanation of the average pulsed force being higher than the continuous force for equal power is that the average pulsed force is decreased linearly by the duty cycle but increased quadratically. As an example consider two equal power beams applied in a vacuum, one continuous and one pulsed at a 50% duty cycle. Since the pulsed beam is only running half the time, it can

draw twice the power in the time that it is on. If it uses this extra power to double the voltage, it can double the charge stored on each craft. Since the force is roughly proportional to the product of the two charges, it will increase by a factor of four while the beam is on, and decay to zero in other half of the time. This results in an average force that is twice the continuous force in this simple vacuum case. However, in a plasma the situation is more complex. The current required to achieve a potential is increased at higher voltages to offset the increased current from the plasma. Further, it takes some time for the large space objects to charge to their steady-state values. In contrast to the earlier continuous beam ET studies, the time-varying charging equations must be considered. The result is a complex set of competing conditions which are investigated in this work.

To investigate the entire search space, a Monte Carlo analysis is first used varying a broad range or spacecraft and electron beam parameters. This numerical analysis tool provides broad insights into the electrostatic force and re-orbiting behavior avoiding assumptions about optimality. A fixed set of nominal GEO space weather conditions are modeled. Of interest is under what conditions pulsing can lead to interesting solutions where the objects are only charged for part of the time while retaining or even improving the tugging performance. Next a deterministic equal power analysis are performed about a nominal continuous case. This analysis is then repeated at different power levels.

4.3.1 Pulsed Beaming Monte Carlo Analysis

In this analysis, the pulsed beam is modeled by a square wave which has four parameters: Voltage (V_b), Current (I_b), Period (T_p), and Duty Cycle (d). Varying the tug (R_T) and debris (R_D) radii increases the search space to six independent parameters. The four parameters that apply to both pulsed and continuous beams ($R_T, R_D, I_\mathrm{b}, V_\mathrm{b}$) are chosen randomly within the bounds shown in Table 4.4. This parameter set is enough to specify the continuous beam properties. For the pulsed beam, two additional beam parameters are required to be chosen: T_p and d. Both the continuous and pulsed parameter sets are then fed into the integrator described in Chapter 2. The average force in the case of the pulsed beams and the force at the final timestep, where both craft

have achieved their steady-state voltages for the continuous cases is computed for each run and stored in a master file along with the parameters that produced it.

Table 4.4: Monte Carlo bounds

Parameter	Lower Limit	Upper Limit
R_T	1.5 m	5m
R_D	1.5 m	5m
V_b	5 kV	100 kV
I_b	0.1 mA	20 mA
T_p	0.1 s	1 s
d	0.01	0.99

The radii range has been chosen to match the self capacitance of typical GEO spacecraft [63] (100-600 pF). The beam voltage extends up to 100 kV, which is higher than currently flown spacecraft electron guns of 20-40 kV. However, the Beam Experiment Aboard Rocket (BEAR) mission demonstrated a 1 MeV accelerator for ions in space [144, 145]. With a 100 kV beam, each spacecraft would ideally charge to $\pm$ 50 kV in a vacuum and neglecting SEE and backscattering. With these kilo-Volts of potentials it is critical that all outer surfaces of the tug are electrically connected to avoid differential charging and arcing. Additionally, the high energy electrons may cause harmful bremsstrahlung radiation [146], which could damage spacecraft electronics [70]. In these simulation scenarios the beam current is designed to overwhelm environmental currents, and the pulse period is chosen to be longer than typical spacecraft charging times. The duty cycle ranges from 1% to 99%.

A center-to-center distance r of $5(R_T + R_D)$ is used. This gives 4 craft diameters of standoff distance (12 m to 40 m). Since many GEO spacecraft have large solar panels and may be rotating, even this distance will require very careful autonomous formation flying. This is not outside the realm of feasibility considering the evolving structured light and LIDAR based relative motion sensing systems being developed [147]. The PRISMA mission demonstrated cooperative controlled formation flying as close as 5 meters [148]. The ANGELS mission also demonstrated close non-

cooperative formation flying, but has not publicly released a minimum distance.

The simulation integration time is constrained to be the larger of 10 pulse periods or 0.1 seconds. The time step is chosen so that either there are 50 steps in the "on" segment of the period, or that the norm of the largest possible currents cannot change either craft voltage by more than 5 kV during one time step. Twenty thousand runs were computed, ten thousand for the pulsed ET and ten thousand for the continuous ET.

4.3.2 Monte-Carlo Based Force Analysis

This section presents the results of a Monte-Carlo analysis of the simulation parameters discussed in the prior section. This numerical approach has the advantage that no a-priori assumption is made of what constituted a good set of simulation examples. The results provide a broad overview of the ET force behavior.

The average force produced by a pulsed beam is plotted against the steady state force of a continuous beam in Fig. 4.17 as black dots. Points below the solid line with slope equal to 1 represent parameter sets ($R_{\mathrm{T}}, R_{\mathrm{D}}, V_{\mathrm{b}}, I_{\mathrm{b}}, T_{\mathrm{p}}$, and d) where the average force was higher for the continuous beam (setting d equal to 1). In this plot, the continuous beams always use more power, and typically produce more force.

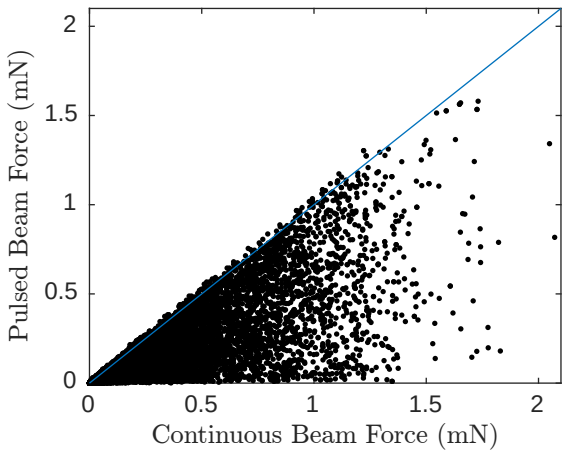

Figure 4.17: Comparison of forces produced by continuous and pulsed beams with all other parameters equal

There are far more points below the line than above it, which is expected since the pulsed beam is expected to increase force efficiency, not pure force. However, many of these pulsed cases open up large (100s of milisecond) windows where both spacecraft are not charged and the beam is off during which measurements and thrusting can happen without interference. As for the magnitude of the continuous forces, there are improvements over prior work. There are multiple parameter sets that produced forces larger than 1.5 mN, in contrast Hogan et al [93] found forces less than 1 mN, but used a more conservative beam voltage and a different charging model.

The pulsed ET begins to show force increases compared to a continuous ET if a power-limited tug is considered. The power in the beam can be expressed as $P = V_\mathrm{b} I_\mathrm{b}$ for the continuous case, and $P = d I_\mathrm{b} V_\mathrm{b}$ for the pulsed beam. In reality, the electrical load on the spacecraft will exceed this value. Many components of a pulsed electron beam require constant power, so the efficiency for the pulsed beams is likely lower than this analysis shows.

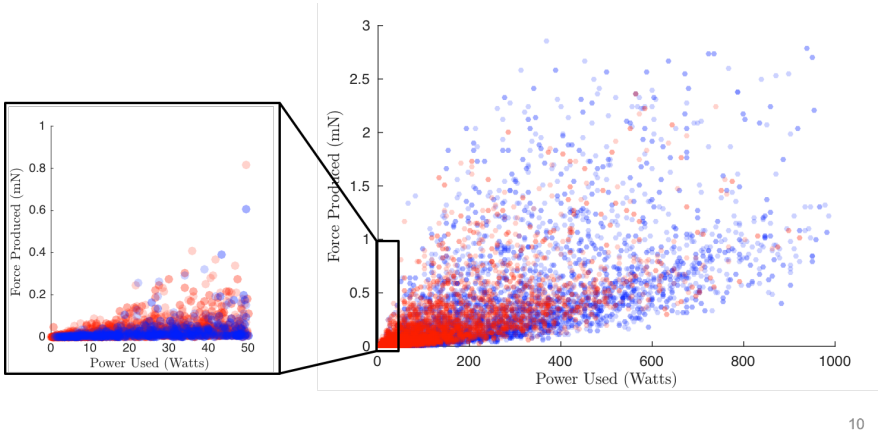

Figure 4.18: Comparison of force produced by continuous (blue) and pulsed (red) beams plotted againts the power in the beam

Both the average force (for the pulsed cases) and the steady-state force (for a continuous cases) are plotted against the power in the beam in Fig. 4.18. The blue points represent continuous beam cases, and the red points represent pulsed cases. This plot shows the force efficiency increases of a pulsed ET. The efficiency is found by taking the ratio of the force (y axis) to the power in the beam (x axis). Points at the top of the scatter cloud represent the most force produced at that

power level. As can be seen in the zoomed-in figure, the highest points are red more often than they are blue which means that a pulsed beam produces more force for a given power inside the power band of 10 to 50 Watts. This trend disappears for high powers due to the 100 kV cap on beam voltage.

Some tug spacecraft may have limited electron beam voltage rather than electron beam power. At sufficiently high voltages, sharp corners on either spacecraft may arc into the ambient plasma through coronal discharge. A high energy beam may also cause Bremsstrahlung, where the deceleration of an electron releases X-rays that could seriously damage spacecraft electronics. Fig. 4.19 shows the force produced by a beam of a given voltage. Blue once again represents continuous cases while red represents pulsed cases.

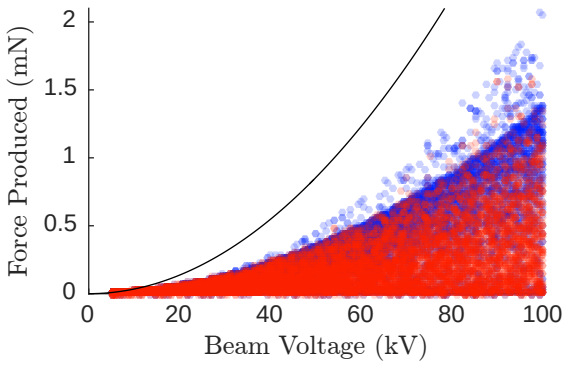

Figure 4.19: Comparison of force produced by continuous (blue) and pulsed (red) beams plotted agains the voltage of the beam. The theoretical max is shown as a solid black line

This voltage-limited case contrasts the power-limited case of Fig. 4.18 in that the continuous beam always produces more force. This can be seen by the higher concentration of blue points near the upper maximum line. Figs. 4.18 and 4.19 show how pulsed beams produce more force in some power-limited situations while continuous beams produce more force in voltage-limited situations.

There is a very strong quadratic limit in the maximum force that can be produced for a given voltage. This matches the findings of Schaub et al. [73] that the maximum force between two equal-radius charged spherical spacecraft in vacuum that employ an electron gun with accelerating

voltage of V is

$$F_{\max} = \frac{4\pi\epsilon_0 R_{\mathrm{T}} R_{\mathrm{D}}}{(r - R_{\mathrm{T}})(r - R_{\mathrm{D}})} \frac{V^2}{4} \tag{4.12}$$

Where the spacecraft are separated by r. For our analysis the center-to-center separation $r = 5(R_{\mathrm{D}} + R_{\mathrm{T}})$ is used. Inserting this yields:

$$F_{\max} = \frac{4\pi\epsilon_0 R_{\mathrm{T}} R_{\mathrm{D}}}{80R_{\mathrm{T}}^2 + 164R_{\mathrm{T}}R_{\mathrm{D}} + 80R_{\mathrm{D}}^2} V^2 \tag{4.13}$$

The maximum of this force occurs when the craft are equally sized, but is independent of the actual sizes. This is only because small craft are closer together. Using equally sized spacecraft yields:

$$F < \frac{4\pi\epsilon_0}{324} V^2 \tag{4.14}$$

$$F < \left(3.434 * 10^{-4} \frac{\mathrm{mN}}{\mathrm{kV}^2}\right) V^2 \tag{4.15}$$

For a 100 kV beam, the theoretical maximum is 3.43 mN. This theoretical maximum is also shown in Fig. 4.19 as a solid black line that bounds all data points. The data points seem to be bounded by an even shallower parabola. The electron beam will cease to achieve charge transfer when $\delta + \eta > 1$, which will happen when the landing energy is low. This is one of many effects that prohibit achieving the theoretical maximum force.

4.3.3 Re-Orbiting Analysis

An end objective of the ET includes re-orbiting debris to a graveyard orbit some 250 to 300 km above GEO. This process is mathematically modeled as a perturbation in the along-track direction which slowly changes the semi-major axis of the debris orbit. Schaub and Jasper [63] approximated the change in semi-major axis over 1 day as:

$$\Delta a = \frac{4\pi}{n^2} \frac{F}{m} \tag{4.16}$$

where n is the mean motion of the orbit [radians/second]. They went on to find this linear relationship between the effective radius (for capacitance matching) and launch mass.

$$m = \frac{R - 1.152\mathrm{m}}{\left(0.00066350 \frac{\mathrm{m}}{\mathrm{kg}}\right)} \tag{4.17}$$

where the radius is between 1 and 6 meters, where it predicts masses between 1000 and 6000 kg. The launch mass is a conservative estimate of the actual mass as all of the station-keeping propellant is likely exhausted. The tug is assumed to be able to keep up with the maximum acceleration of the debris using thrusters. The SMA rate is then found by using the debris mass. The SMA rate is plotted against the power in the beam for both the pulsed and continuous beam cases in Fig. 4.20 where red points are pulsed and blue points are continuous. Again, red points outnumber blue

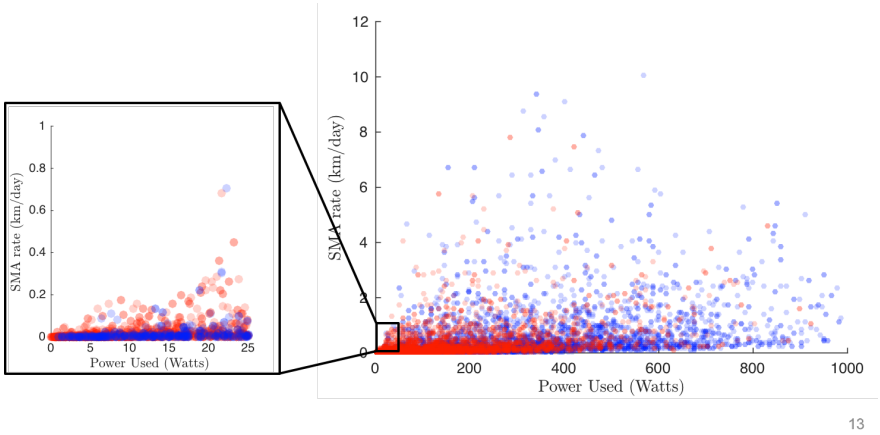

Figure 4.20: Comparison of SMA rate produced by continuous (blue) and pulsed (red) beams plotted agains the power in the beam

points at the upper edge of the scatter cloud in the lower zoomed-in plot. This means that in power-limited cases, a pulsed beam will achieve higher force. This trend disappears in the upper plot due to the 100 kV beam voltage cap. As a comparison to prior work, the fastest SMA rate is near 6 km/day, which translates to re-orbit times less than 2 months rather than the 2-4 month estimates in earlier work. As with the force analysis, the pulsed cases are consistently more efficient between 10 and 50 Watts. To investigate a voltage-limited craft, the SMA rate is plotted against the beam voltage in Fig. 4.21. The data once again has a quadratic bound, but this is not as striking a trend as the plot of force vs. voltage in Fig. 4.19. This bound can be analytically predicted by combining the SMA rate equation, Eq. (4.16), the mass-to-radius relationship, Eq. (4.17), and the force optimum found earlier, Eq. (4.13). When this is done the following SMA rate maximum is

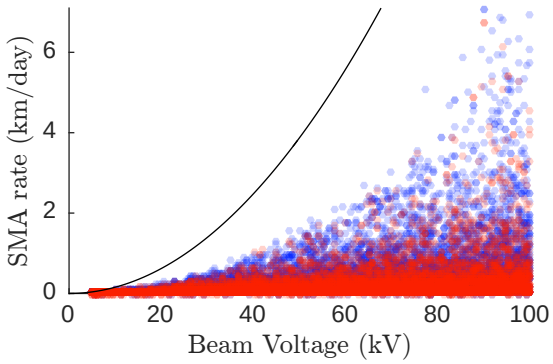

Figure 4.21: Comparison of SMA rate produced by continuous (blue) and pulsed (red) electron beams. Theoretical maximum rate is shown as a solid black line

found:

$$\begin{aligned}\frac{\Delta a}{\text{day}} &< \frac{4\pi}{n^2}\frac{F}{m} \\ &< \frac{4\pi}{n^2}\frac{0.00066350\frac{\text{m}}{\text{kg}}}{(R_\text{D}-1.152)}\frac{4\pi\epsilon_0 R_\text{T} R_\text{D}}{80R_\text{T}^2+164R_\text{T}R_\text{D}+80R_\text{D}^2}V^2\end{aligned} \tag{4.18}$$

The SMA rate is maximized when the deputy mass is low and the force is high. This is done by making the deputy as small as possible and making the tug and deputy the same size, which gives both of them a radius of 1.5 m. This explains why the quadratic boundary was not seen as clearly – the force maximum is found when both radii are equal while the SMA rate maximum requires both radii be equal *and* small. The quadratic boundary would likely become more evident if the number of Monte Carlo runs is increased. Inserting radii of 1.5 meters for both craft yields the following theoretical bound for the SMA rate.

$$\frac{\Delta a}{\text{day}} < \left(1.5558 * 10^{-3}\frac{\text{km}}{\text{day kV}^2}\right) V^2 \tag{4.19}$$

For a beam of 100 kV, the maximum SMA rate is 15.58 km/day. This analytic maximum is shown as a black line in Fig. 4.21 and clearly bounds all data points.

4.3.4 Equal Power Analysis

The Monte Carlo results show that if the beam voltage is limited and power is not, continuous beams always produce more force. However, if the beam power is limited and the voltage is not,

pulsed beams can achieve higher forces if the power is low. This section uses deterministic equal power analysis to investigate the regions where pulsed beams produce more force than continuous beams.

4.3.5 Single Power Level

If the analysis is constrained to a certain power and tug and debris sizes it changes the problem from six-dimensional to three-dimensional, two of which are non-physical for continuous beams. To investigate the highest force produced at a single power level, small departures from optimal continuous beam cases are considered. The power in a beam for a continuous and pulsed beam is given by,

$$P = I_{\mathrm{b}_0} V_{\mathrm{b}_0} = I_{\mathrm{b}} V_{\mathrm{b}}\, d \tag{4.20}$$

respectively, where a sub-subscript of 0 indicates the continuous case. If both beams are constrained to have the same power, the pulsed voltage and current must rise since $d < 1$. A way to raise both the voltage and the current equally is:

$$I_{\mathrm{b}} = \frac{I_{\mathrm{b}_0}}{\sqrt{d}} \qquad V_{\mathrm{b}} = \frac{V_{\mathrm{b}_0}}{\sqrt{d}} \tag{4.21}$$

This deterministically allows for the effect of pulsing to be investigated in a one-dimensional manner. A degree of freedom is added to allow optimal tuning of the voltage and current:

$$I_{\mathrm{b}} = \frac{\gamma I_{\mathrm{b}_0}}{\sqrt{d}} \qquad V_{\mathrm{b}} = \frac{V_{\mathrm{b}_0}}{\gamma\sqrt{d}} \tag{4.22}$$

A γ value greater than 1.0 indicates that current increases more than voltage, and a value below 1.0 indicates that voltage increases more than current. The pulse period does not make a large difference in the range of 0.1 to 1 sec, so it is randomized and only the maximum force case is considered. This allows the problem to be analyzed deterministically in two dimensions.

In the following analysis a 2 meter tug and a 1.5 meter deputy in nominal GEO space weather conditions separated by $\rho = 5(R_{\mathrm{T}} + Rd) = 17$m and a power of 16 Watts were considered. Continuous beam parameters are taken from Hogan et al. [93] as $V_{\mathrm{b}} = 37$ kV and $I_{\mathrm{b}} = 432$ μA and

produces a force of 0.2103 mN. Since the charging model used in this paper differs slightly, a 16 Watt optimum for continuous force is achieved at 23.9 kV and 670 μA. To expand this, duty cycles of 10%, 25%, 50%, 75% and the continuous case, 100% are investigated. The voltage/current ratio tuning parameter γ varies logarithmically from 0.4 to 2.5 which gives equal space to look at high voltage cases as high current cases. A plot of the max force subject to the the two deterministic parameters d and γ is shown in Fig. 4.22: Each row of this plot has the same duty cycle – the top

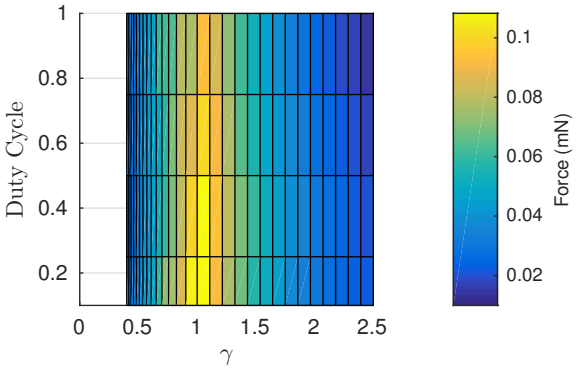

Figure 4.22: Force produced at 16 Watts subject to changing voltage, current, and duty cycle.

row represents a continuous beam and the bottom row represents a pulsed beam with a 10% duty cycle. The columns of the plot have the same γ value, meaning that the relative scaling of voltage and current is the same, although both increase by $1/d$ as one travels up a column.

Eq. (4.22) shows that current will be constant when $d \propto \gamma^2$. Since d is along the y axis and γ is along the x axis, parabolas are level curves in current in Fig. 4.22. Current is minimized in the bottom right corner, maximized in the upper left corner, and steps up along ever-steepening parabolas between them. Level curves in voltage are given by $\gamma \propto \frac{1}{\sqrt{d}}$ which in this plot translates to $y \propto 1/x^2$. Voltage is minimized in the bottom left corner and maximized in the upper right.

The top row of Fig. 4.22 has a maximum at $\gamma = 1$ which confirms that the new values of 23.9 kV and 670 μA are optimal. The max force at lower duty cycles is also found with γ near 1, which gives a good starting point for optimizing the force. At this power level, the maximum average force produced by the pulsed beam is 23.8% larger than the maximum continuous force.

Additionally, a 10% duty cycle beam opens up 900 ms windows where both craft are uncharged and the beam is not operating. This would allow for small micro-thrust control maneuvers and measurements to be made without interference from the electron beam.

4.3.5.1 Power Level Range

To investigate whether the force increase persists at different power levels for these particular tug and debris object dimensions, this analysis is repeated at 2, 4, 8, 16, 32, 64 and 128 Watts. The baseline parameters (for the continuous case) are hand-tuned to find beam voltages within 1 kV of the optimal and are given in Tab. 4.5. These baseline continuous voltages serve as starting points to ensure that the actual force maxima will lie within the γ range as is shown in Fig. 4.22.

Table 4.5: Baseline Continuous Beam Parameters

Power (W)	V_{b0} (kV)	I_{b0} (mA)
2	7.9	0.253
4	11.4	0.351
8	17	0.471
16	29	0.552
32	41	0.781
64	57	1.123
128	79	1.620

If the maximum continuous force is treated as a baseline, the maximum average pulsed force can be compared by dividing the pulsed force by the continuous force. Values greater than 1 indicate situations where pulsing provides force benefits as well as windows of opportunity. This normalized force is shown as a function of the duty cycle in Figure 4.23a. Different power beams are shown as different color lines. For all powers above 8 Watts there is a clear force benefit to pulsing – the average pulsed force is higher than than the steady state continuous force. The force increases are highest for 16 and 32 Watts, which is where previous work for the continuous ET has focused. This means that pulsing the beam provides force efficiency increases as well as windows of opportunity in a relevant regime.

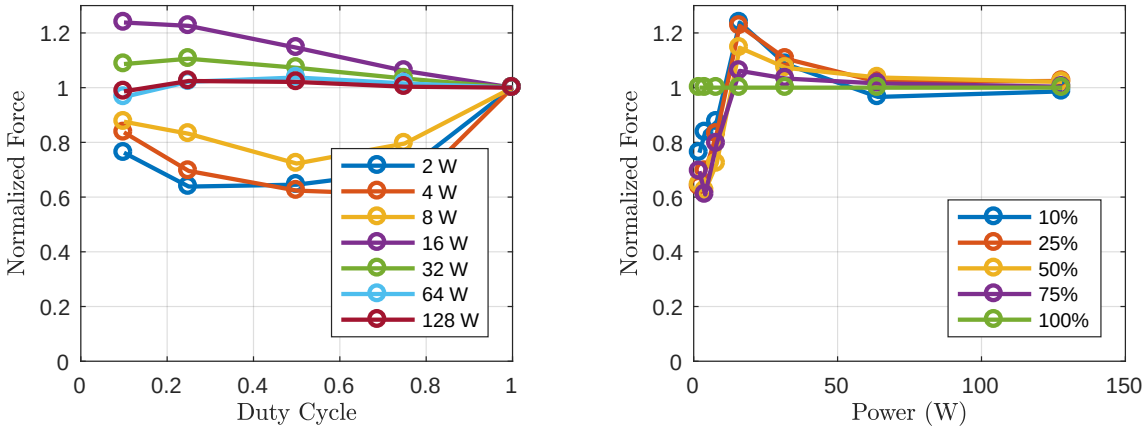

(a) As a function of Duty Cycle

(b) As a function of Power

Figure 4.23: Normalized force at different duty cycles for different power levels.

Note that the power levels at which the pulsed ET force magnitude advantages over the continuous ET solution are specific to the spacecraft dimensions assumed in this section. Differently sized objects would show a similar trend, but have distinct critical power levels.

This data can be visualized in a different way as well – plotting the normalized force against the power and using different lines for different duty cycles shows the power regime where pulsing is most beneficial. Each color in the plot in Figure 4.23b represents a different duty cycle, with green being a continuous beam and blue being a 10% duty cycle. For the 2, 4, and 8 Watt beams, pulsing the beam actually decreases performance by between 10 and 40%. However, for all powers larger than 8 Watts, the average force with pulsing is higher. The largest gains occur at 16 Watts, and slowly drop to only a few percent improvement. The 10% duty cycle beam, although it has the greatest force increase at 16 Watts, performs worse than the continuous beam at 64 and 128 Watts. Additionally, in all of these regimes, a pulsed beam offers 250 - 900 ms windows where both craft are discharged and the beam is not operating during which control maneuvers can be executed and measurements can be taken without beam interference.

4.3.6 Section Conclusions

This section introduces the pulsed electrostatic tractor and performs preliminary analysis to find regimes where it provides force increases. Six parameters ($R_{\mathrm{T}}, R_{\mathrm{D}}, V_{\mathrm{b}}, I_{\mathrm{b}}, T_{\mathrm{p}}, d$) are selected to vary in a Monte Carlo analysis. An analytic upper bound for the force between two spacecraft as a function of beam voltage is found, and has good agreement with the Monte Carlo results. In a voltage-limited case, continuous beams give more force. In a power-limited case, pulsed beams sometimes give more force. In this analysis, they can give up to 23% more force than continuous beams of the same power as long as the power is less than around 50 Watts. The results are then applied to orbit raising for both power and voltage-limited spacecraft. The pulsed ET is also more efficient for semi-major axis raising at low power levels. A similar analytic upper bound for the semi major axis rate as a function of beam voltage is found. This limit also has good agreement with the Monte Carlo results.

A deterministic equal power analysis is performed for continuous and pulsed beams at 2, 4, 8, 16, 32, 64, and 128 Watts for this particular spacecraft size and distance scenario. Force increases for a pulsed beam are found for all powers greater than 8 Watts, with the highest increases occurring at 16 Watts. Pulsing also opens up windows of opportunity to perform thrusting and take measurements at all power levels.

Pulsing the electron beam in the Electrostatic Tractor offers force increases for the same power in a certain power regime, and creates windows of opportunity during which control maneuvers can be executed and measurements can be taken without interference from the electron beam. This allows for faster re-orbiting of GEO debris objects that are currently increasing the risk of collision in a very valuable orbital region.

4.4 Equilibrium Electrostatic Tractor Analysis

This section analyzes the ET concept with a high-fidelity charging model and under equilibrium conditions. The first analysis of the charging aspect of the ET [73] included electron and ion

thermal currents using a nominal Maxwellian current model, the photoelectric current, and Secondary Electron Emission (SEE) from the beam electrons, but neglected SEE and backscattering from the thermal currents. Hogan and Schaub in [74] further develop the ET charging model by considering the Maxwellian thermal currents at planetary K-indices of $K_P = 1.5$ and 6. Additionally, they account for SEE and photoelectrons from the debris that provide an additional negative current to the tug. Reference [75] also investigates the performance of the ET with normal variations in the plasma parameters throughout an orbit using single Maxwellian populations based on work by Denton et al. [149]. More force is produced in the early morning sector (Local Times between 1 and 6) due to the high temperature electron plasma in that region. Reference [96] investigates a pulsed electron beam with the same Maxwellian-based model as [74] but solve the equations with respect to time to account for the charge-up and discharging behavior. Reference [107] uses the same model as [75] but changes the density and temperature throughout the orbit.

This section does not use Maxwellian currents at all but rather uses an empirical model presented in Chapter 2 to predict the flux as a function of energy, local time (LT) and Planetary K index (K_P). This flux distribution is numerically integrated to give the current to the spacecraft as well as the SEE and backscattering yield at a given spacecraft potential. Additionally, all yields except that from the electron beam are assumed to be isotropic as opposed to prior work which used normal incidence. The ET force is studied for candidate mission scenarios for multiple beam currents and voltages as a function of local time for both a calm space weather condition ($K_P = 2-$) and a stormy space weather condition ($K_P = 8$). Then, the optimal orbit-averaged forces are investigated for many different power and tug-to-debris size levels. Next, pulsing is re-examined for long pulse periods as a function of power and size ratios.

To find the force between two spacecraft, the tug and debris radius must be chosen along with the beam current and energy. Using the tug radius and beam current along with local time, the tug potential can be found by directly interpolating the top sheet of Fig. 2.7. Finding the debris potential is unfortunately more difficult. The yield from the electron beam reduces the net current and is a function of the landing energy of the beam. Thus, to find the net electron beam current

and interpolate the debris potential, one would need to already know the debris potential in order to compute the yield. To solve this problem, a function is written which takes a candidate debris voltage, then computes the actual beam current as well as the needed beam current to support that voltage. The debris voltage is varied so that these two numbers are identical. Using this procedure, the equilibrium voltages of two spacecraft can be found easily as a function of their sizes, beam energy and current, and the local time.

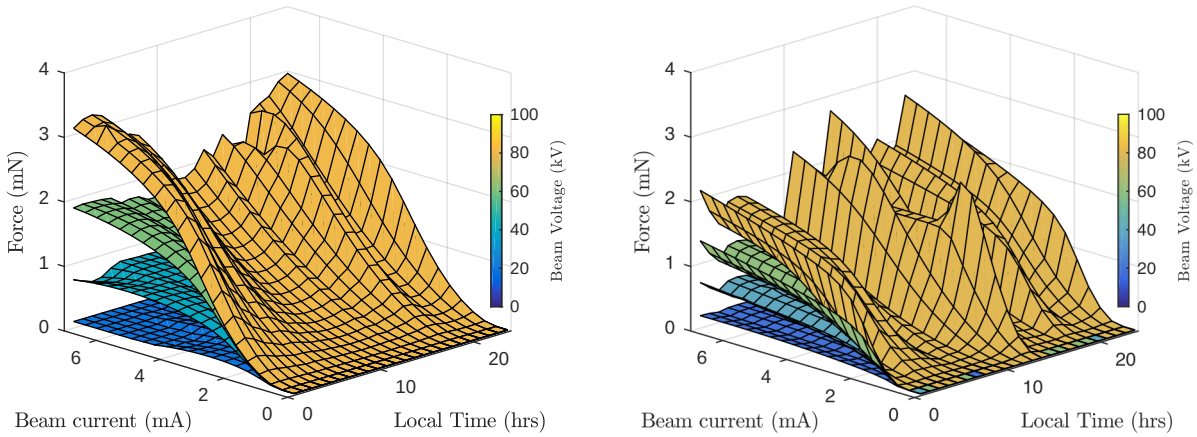

(a) $K_P = 2-$ (b) $K_P = 8$

Figure 4.24: Force between a 3 m tug and 2 m debris separated by 20 m as a function of beam current, voltage, and local time

Consider the example case of a 3 m tug and a 2 m debris separated by $\rho = 4(R_T + R_D) = 20$ m. The attractive force between them is shown in Fig. 4.24 at $K_P = 2-$ and $K_P = 8$. The force generally increases with a higher voltage and current, and has a decent amount of texture with respect to local time. The highest force is near local midnight for the calm space weather condition when it is easiest for the debris to charge very negative. The force grows quickly with current when the current is low, but seems to saturate at higher currents. During storm time there is a lot more variation in force throughout the orbit, and the force actually decreases with current for some local times.

4.4.1 Average Force Analysis

The total re-orbiting time will be better related the orbit-averaged force than the instantaneous force. The orbit averaged force is computed by averaging the forces across local time. These forces are shown in Fig. 4.25 for a 20, 40, 60, and 80 kV beam assuming the same 3 m tug and 2 m debris separated by 20 m. The continuous lines represent $K_P = 2-$ and the dashed lines represent $K_P = 8$.

The 20 kV beam performs just as well as the higher energy beams until about 1 mA where the higher energy beams split. The 40 kV beam stays with the others until about 2 mA, and the 60 kV stays with the 80 kV until 3 mA. The reason for this behavior is that the extra beam voltage doesn't really help until the debris and tug are charged so differently that the extra accelerating voltage is needed for the beam to reach the debris. These departure currents must be the currents at which the potential difference between the two craft is either 40, 60, or 80 kV. The SEE current is also a function of the landing energy, which is why the curves are not quite identical below the departure currents.

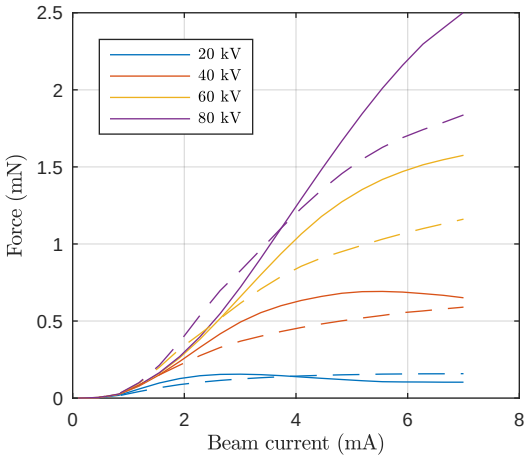

Figure 4.25: Orbit averaged force as a function of beam current, voltage, and local time. Dashed lines represent $K_P = 8$, and continuous lines represent $K_P = 2-$

The orbit averaged storm forces are slightly lower than the calm forces except for low current for the 80 kV beam and high current for the 20 kV beam. This differs from prior work [74, 107]

which always found higher forces during a storm. This difference is due to the very different charging and environmental models used, which only share the model for the photoelectric current.

4.4.2 Relative Sizing Analysis

In prior work, Hogan et al [93] found that small tug vehicles would have a hard time charging a much larger debris object. This is because while for the small tug the beam current is enough to cause significant charging, it will barely overcome the photoelectric current on the large debris. This analysis is repeated here, but from a force rather than charging perspective. Because of the induced charge, there is an attractive force even if there is no change in the debris voltage. The force as a function of beam power between a 3 m tug and different debris sizes is shown in Fig. 4.26a. The separation distance for all cases is 20 m.

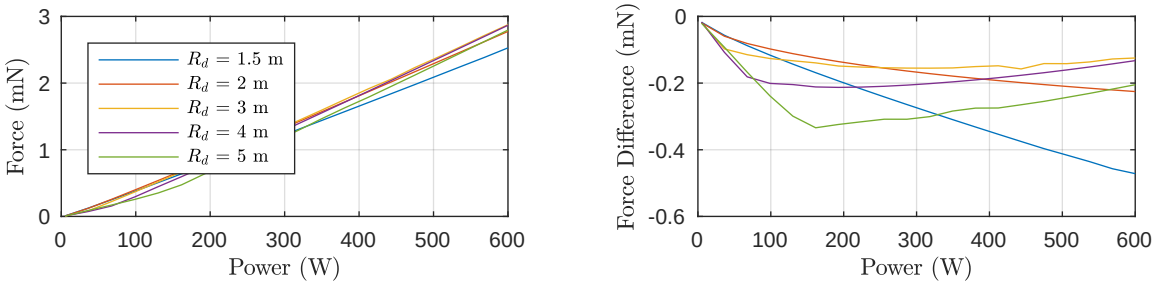

(a) Force

(b) Force difference

Figure 4.26: Best possible force at different powers for different tug to debris size ratios at $K_P = 2-$

The maximum force is found as a function of power for a variety of different debris sizes - the tug size is fixed at 3 m so the ratio of tug to debris radius spans from 0.5 up to almost 2. The force is very linear with power with a slope of roughly 1/2 a mN per 100 Watts of power regardless of debris size. Because it is difficult to see departures from this trend at this scale, the difference in force from this linear fit is shown in in Fig. 4.26b. The highest force (or least negative in this plot) is when $R_D = R_T = 3$m at most powers with $R_D = 2$ and 4 m very near. The extreme ends of the spectrum where R_D is 1.5 or 5 meters produce less force. This is because the beam can be close to optimal for both craft when they are the same size, but not when they are different sizes.

4.4.3 Pulsing Analysis

Prior work has considered a pulsed electron beam rather a constant-current beam [96, 107]. The benefits to pulsing are twofold - first it introduces windows where both spacecraft are discharged and the beam is off which can be used for communications, thrusting, or measurements to be taken that might be interfered with by the beam. Secondly, pulsing the beam can increase the force at a given power level. In this analysis, the optimal force at different power levels shown in Fig. 4.26 will be re-used. If the pulse period is large compared to the charge up time, the force that a pulsed beam produces can be approximated as the equilibrium force for the duration of the pulse period. Since the capacitance of the objects considered here are around $4\pi\epsilon_0 R \approx 10^{-10}$ Farads, a 1 mA beam could change the voltage by 1 kV in approximately 0.1 ms, this assumption of steady state forces will be valid for all pulse periods larger than 1 second.

With this assumption the charge-up and charge-down behavior is ignored and the average force produced by a pulsed beam is given by

$$F_P(P, d) = d\, F_M(P/d) \tag{4.23}$$

where $F_M(x)$ is the maximum force at a power level of x, F_P is the average force from a pulsed beam at power P with a duty cycle of d, which is the fraction of time that the beam is on. During the "on" part of the cycle, the power can be raised to P/d without changing the average power since it is not operating while the beam is off. Multiplying the force by d accounts for it being on only d of the time.

If the maximum force is directly proportional to power, there is no benefit at all to pulsing because the ds would cancel each other out. However, if the force increases quadratically, or is linear with an offset, there can be an increase in force. The increase in force from moving from a continuous beam to a pulsed beam of the same power is shown in Fig. 4.27a for the case of the tug and debris both having a radius of 3 m.

A pulsed beam almost always increases the force for a given power level, with the largest gains found for low power and low duty cycles. For very low powers, the pulsed force can be more

than 2 times larger than the continuous force, and even at 100 W a pulsed beam can improve the force by 25%. Because the max beam voltage is set at 100 kV, the low duty cycle beams are infeasible at high power levels because they require too high of a beam voltage while the beam is on. The increases are larger during stormy conditions especially near 25 Watts.

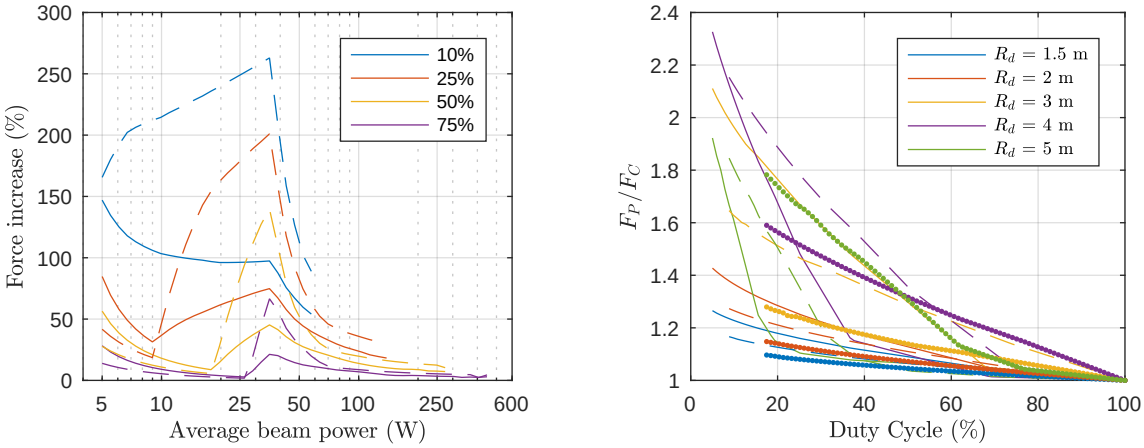

(a) Force increase as a function of duty cycle and power. Continuous lines represent $K_P = 2-$ and dashed lines represent $K_P = 8$.

(b) Force ratio as a function of tug and debris sizes and duty cycle at $K_P = 2-$ with continuous lines representing 25 W, dashed lines representing 50 W, and dots representing 100 W of power.

Figure 4.27: Pulsing force analysis

Now consider varying the tug to debris size ratio as well as pulsing. Referring again to Fig. 4.26, the force is more convex when the debris is larger than the tug. This would indicate that pulsing would be more advantageous when the tug is smaller than the debris since the gain from the force at the higher power level $F_M(P/d)$ would outweigh the loss from only being on d of the time. The ratio of the pulsed to continuous force is shown below in Fig. 4.27b

The force ratio is shown for the power levels of 25 W (continuous lines), 50 W (dashed lines), and 100 W (dots). The lines end at low duty cycles when the beam voltage required is larger than 100 kV, which happens sooner for the high power cases than the low power ones. The force ratio is by definition 1 at a 100% duty cycle, and either increases or decreases for different debris sizes. All debris sizes benefit from pulsing at these power levels, but the biggest gains are for the larger debris (green and purple lines). The smallest debris object additionally start to trend downward

for very low duty cycles.

4.4.4 Orbit Raising

If the forces as a function of local time are used as a purely along-track acceleration in Gauss' variational equations, the change in the orbit can be found. The acceleration is found by estimating the mass from the relationship originally presented in [63] and dividing to find the acceleration.

$$M(kg) = 1507\,(R(m) - 1.152) \tag{4.24}$$

First the semi-major axis (SMA) change per orbit equation [63] for a purely along track acceleration is

$$\Delta a = \frac{4\pi}{n^2}\frac{F}{m} \tag{4.25}$$

where n is the mean motion of the orbit. Then, for each debris radius and power level, calculate the time it would take to raise the SMA by 250 km using the mean motion at it's initial orbit radius. This is shown in Fig. 4.28.

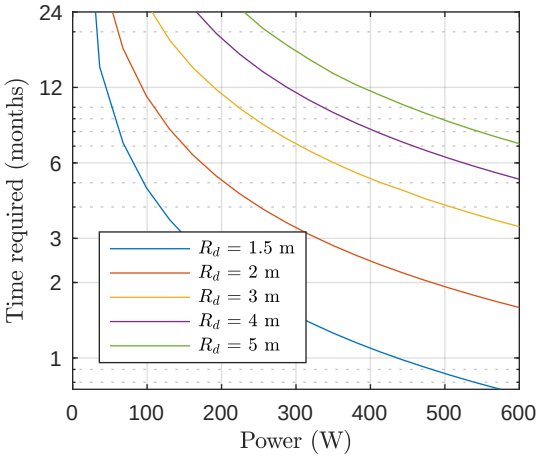

Figure 4.28: Time to move GEO debris to a graveyard orbit for a 3 m tug

In general using more power reduces the time it takes to move the debris to the graveyard orbit, but the gains are greater at lower powers. It takes the 3 m tug a little more than 3 months to tug another 3 m object to the graveyard orbit. In contrast it only takes 22 days if tugging a

1.5 m debris, and 7 months if tugging a 5 m object. Clearly the ratio between the debris and tug sizes is very important for tugging. Keeping in mind that the tug size is purely for self capacitance and current collection; with sufficiently large deployable structures, the tug could be a lightweight cubesat.

Next, consider a higher fidelity orbital analysis but only for one scenario. The rates of the classical orbit elements are found due to the acceleration which changes with local time and integrated with an RK4 integrator. The only rates of interest that have a sensitivity to an along track acceleration are the semi-major axis, the eccentricity, and the argument of perigee.

This analysis can show how long it will take a tractor to pull a debris object into the graveyard orbit, and also what happens to the other orbital parameters during this operation. Consider a 3 meter tug and 2 m debris object separated by 20 m at nominal altitude inclined by 1°. The change in the perigee radius is shown in Fig. 4.29. The perigee radius is shown rather than the semi-major axis because that is the parameter that needs to be increased in order to prevent future collisions.

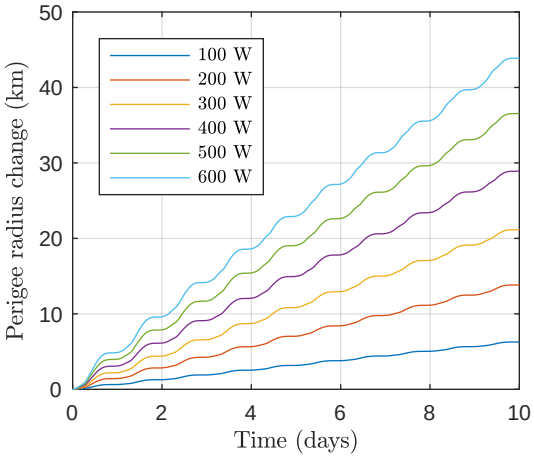

Figure 4.29: Change in perigee radius over 1 week of operation

If the tractor can use 600 Watts of power, it can tug this debris object into the graveyard orbit in 57 days using this average rate. The beam voltage required is 77 kV and the current is 7.8 mA. If if can only use 100 W of power it will take 398 days, or 13 months. These estimates predict slightly larger times to the graveyard orbit then Fig. 4.28, but are still in the same ballpark. This is

expected since the analytical method does not account for the changing eccentricity or the coupled nature of the rates.

4.4.5 Section Conclusions

A new charging model for the Electrostatic Tractor is developed which uses an empirical model for the electron and ion fluxes which is used to compute the thermal electron and ion currents as well as the SEE and backscattering yields as well as accounting for isotropic incidence in the yields. The major impact of this new model relative to prior work is that it is much harder for an object to charge negative due to the higher yields. This model is used to predict the forces for a variety of beam currents and voltage as well as tug and debris sizes at both $K_P = 2-$ and $K_P = 8$. It is found that the force is highest near local midnight, and that the orbit averaged forces only depend on the beam voltage past a current threshold. The forces are mostly linear with power with a slope of around 1/2 a mN per 100 Watts for a 3 m tug

Pulsing is the most effective for large debris objects at low powers, but pulsing still provides force increases for all scenarios evaluated as well as opening windows for controls and sensing to take place without interference from the beam. Orbit raising is considered next, the ET is most effective when tugging small debris, but that is only because they are assumed to be light. A tug spacecraft could also deploy large conducting surfaces to increase its effective radius without significantly changing its mass. For many scenarios, a tug could pull a debris object from the operational GEO ring to a graveyard orbit in a few months. Overall, the higher fidelity charging model finds that more current and power is required to operate the ET but it is still a feasible mission concept for touchlessly tugging space debris to the graveyard orbit.

Chapter 5

Conclusions

This dissertation investigates how spacecraft charge, what forces and torques this charging causes, and what the effects of these forces and torques are. Spacecraft charging is studied using both Maxwellian and empirical flux to investigate the coupling between flux distributions and SEE. Force and torque prediction is studied both analytically and numerically for both conductors and dielectrics. Lastly, the effects of this charging is studied for both charged debris and the ET.

Spacecraft charging is studied in both a equilibrium and time varying case using both Maxwellian and empirical flux distributions. If the total yield is greater than 1, a spacecraft cannot charge negative no matter how much flux the environment provides since every incident electron will create even more secondaries. For many materials, especially if isotropic rather than normally incident flux is used, the energy range where the yield is greater than 1 can be very large. Since the empirical flux model predicts more flux in this intermediate energy range, negative charging is limited for both the ET and for charged debris.

This energy range is a strong function of material properties which vary considerably even for the same material. For instance, Aluminum has more than a factor of 2 of variation in the literature in the most significant parameter for SEE. These parameters are also a strong function of temperature and surface preparation and may change due to aging. Because of the inherent uncertainty in the material properties as well as the electron and ion flux, it is very difficult to predict the voltages accurately, especially without direct measurements for a specific spacecraft.

Nonetheless, material parameters and fluxes are assumed and trends are studied. For the ET,

the new SEE and flux model amounts to more electron beam current being needed to charge the debris spacecraft but the concept is still feasible. As an example, prior work that used Maxwellians used a few hundred μA of beam current to charge the debris. This work predicts that a few mA are needed. For charged debris, this change to empirical flux makes the predicted voltages much lower. Prior work assumed voltages near -30 kV, but this work finds a maximum voltage slightly less than -2 kV in the shade at $K_P = 8$.

Given the uncertainties in the voltage, the ET ought to have some method to measure its own voltage and the debris voltage. If charged debris were being tracked, the voltage would need a large covariance in voltage to account for this uncertainty.

Electrostatic force and torque prediction is studied using both analytic and numeric methods. The analytic approach yields an infinite series from a binomial expansion that can be truncated at appropriate order. This approach gives useful insights that would not be apparent if using only numeric methods – for instance, the center of mass location is vital when predicting the torque. If this is mis-modeled, the torque can actually be in the opposite direction as predicted which could drive a controller unstable.

The numerical methods used are the Multi-Sphere Method (MSM) and the Method of Moments (MoM). The MoM uses "smarter" elements that take the size of the element into account than traditional finite element methods. This allows for the creation of heterogenous Surface MSM (SMSM) models for general objects. This is particularly relevant for modeling the forces and torques during very close proximity operations such as docking. When the spacecraft come very close, the surfaces most near to each other could be sub-divided for greater spatial charge resolution and therefore better force and torque prediction.

The MSM is modified to account for both dielectrics and conductors by using static point charges as well as conducting spheres. Although including dielectrics greatly complicates the optimization process by including three different charging regime datasets and twice the number of constraints as can be enforced with conducting bodies, the mean errors are still almost always below 1%. This force and torque prediction is only as good as the predicted or measured voltage

and surface charge distribution, which will likely be the dominant source of error, not the force modeling. Fortunately, dielectrics can be ignored for most spacecraft since the image charge will cancel out the dielectric charge.

The orbital effects of charging for charged debris are shown to be very significant, leading to multi-kilometer spreads in position after a few hours or hundreds of kilometers after a few orbits, for certain lightweight debris objects. Contrary to prior speculation, it is the electrostatic *torque*, not the Lorentz force which changes the orbit. The mechanism for this is that the torque changes the attitude which influences SRP, which changes the orbit. For the lightweight HAMR plates, including or neglecting electrostatics can lead to hundreds of kilometers of displacement after a few orbits. Although these displacements are large, they are not in any coherent direction and so cannot be predicted with any certainty. Rather, the covariance must be increased to capture the effect of this perturbation. While electrostatics are a significant perturbation for these objects, these objects are so unstable because their center of pressure is not coincident with their center of mass that virtually *any* perturbation will cause significant perturbations. Additionally, electrostatics perturbations, even in the most dramatic charging scenario, are similar in effect to 1° of attitude uncertainty. Since getting *any* estimate of attitude, let alone 1°, is very unlikely for a small non-cooperative object at GEO, it is doubtful that electrostatics will be useful to account for outside of enlarging the covariance.

The ET concept is proposed to tug debris into a graveyard orbit to reduce the collision probability in GEO. For it to be useful, the force between the tug and debris should be as strong as possible to allows for faster tugging. The maximum force is studied in both a power-limited and voltage limited case and it is found that a pulsed electron beam produces more force for the same average power than a continuous beam. Pulsing the beam also creates windows of opportunity where measurements can be taken and maneuvers can be performed without the craft being charged. However, this assumes that the electron beam has the same power efficiency at low voltage as high voltage which is not true in general. It also would necessitate a more complex power delivery and storage system than a continuous beam which may have negative mission-level consequences.

5.1 Future Work

The problem of electrostatic dynamical effects on orbit is far from solved. There are many questions still to be answered in both applications. A few that seem to be the lowest hanging or most necessary are listed below.

5.1.1 Geometrically Realistic Spacecraft Charging

Although the level of detail in modeling the plasma environment has risen incredibly in this work, the level of detail in modeling the spacecraft has remained low. Modeling the charging of geometrically complex spacecraft is important because not all surfaces are exposed to the plasma and therefore see less flux than expected. Additionally and possibly more importantly, If the spacecraft is not continuously conducting, potential wells can form which do not let environmental particles reach a portion of the spacecraft even though it may be at a voltage that indicates that they would.

5.1.2 Empirical SEE Model

Understanding the SEE characteristics of a spacecraft is probably the greatest challenge to predicting how it will charge. This is compounded by the fact that the material properties change depending on how long they are in space. It is possible to infer the SEE parameters of an entire spacecraft by using electron and ion flux data and the known voltage. By varying SEE parameters so that the predicted voltage matches the actual voltage, an effective SEE model could be created for the spacecraft. Much of this data is already available from the LANL Geo spacecraft.

5.1.3 Optimal Design of Tug Vehicle

For the Electrostatic Tractor, the tug craft needs to carry a lot of charge but does not need to be heavy. This could be achieved by using a large deployable structure to increase the self capacitance without increasing the weight significantly. For instance, a large metallic membrane

could be stretched over deployable hoops and the tug could be a cubesat. This structure could weigh much less than a kilogram but have a 2 or 3 meter radius and increase the force by an order of magnitude. Additionally, electrostatics itself could be used to inflate the structure, but this raises concerns about the structure deforming in an unknown way due to the pull of the debris craft. Since the tug should charge very positive it could also chose exterior materials with very high SEE to help it charge positive.

5.1.4 Laboratory Experiments

Plasma physics is a complex field with relatively few solvable problems. This means that there are a number of questions which do not have clean analytical or even numerical answers and can only be solved through experiment. Two of these are spacecraft charging in a disturbed plasma environment and plasma shielding.

For charging in a disturbed plasma, consider the ET. The tug will charge positive which will attract an abundance of electrons and will change the charging behavior of the debris since its environment is richer in electrons than the undisturbed environments. By the same processes, the tug should have disturbed charging behavior because the debris will attract ions. If one craft were charged much more than the other, analytical approximations could be made, but when they have comparable equal and opposite charge this problem is formidable.

For plasma shielding, earlier work suggest that it is negligible at GEO but that has yet to be confirmed experimentally. Possibly of more interest is the prospect of extending electrostatic actuation to lower altitudes where the density is higher and shielding would have to be considered. Experiments could be performed to understand how significant shielding is when the voltages are very high, or the charging is pulsed at a similar frequency to the plasma frequency.

Bibliography

[1] J. McMahon and D. J. Scheeres, "A New Navigation Force Model for Solar Radiation Pressure," AIAA Journal of Guidance, Control and Dynamics, Vol. 33, 2010, pp. 1418–1428.

[2] C. Früh, D. Ferguson, C. Lin, and M. Jah, "The Effect of Passive Electrostatic Charging on Near-Geosynchronous High Area-To-Mass Ratio Objects," Proc. AAS Space Flight Mechanics Meeting, Santa Fe, NM, Febuary 2014, pp. 3121–3137.

[3] M. Bengtson, K. Wilson, J. Hughes, and H. Schaub, "Survey of the electrostatic tractor research for reorbiting passive GEO space objects," Astrodynamics, Sep 2018, 10.1007/s42064-018-0030-0.

[4] J. I. Minow and L. N. Parker, "Spacecraft Charging: Anomaly and Failure Mechanisms," Spacecraft Anomalies and Failures Workshop, July 24 2014.

[5] T. Bennett and H. Schaub, "Touchless Electrostatic Three-Dimensional Detumbling of Large Axi-Symmetric Debris," Journal of Astronautical Sciences, Vol. 62, No. 3, 2015, pp. 233–253.

[6] J. Fennell, H. Koons, M. Leung, and P. Mizera, "A Review of SCATHA Satellite Results: Charging and Discharging," Tech. Rep. TR-0084A(5940-05)-7, The Aerospace Corporation, El Segundo, CA, 1983.

[7] E. G. Mullen, M. S. Gussenhoven, D. A. Hardy, T. A. Aggson, and B. G. Ledley, "SCATHA Survey of High-Voltage Spacecraft Charging in Sunlight," Journal of Geophysical Research, Vol. 91, No. A2, 1986, pp. 1474–1490, 10.1029/JA091iA02p01474.

[8] R. C. Olsen and C. K. Purvis, "Observations of Charging Dynamics," Journal of Geophysical Research, Vol. 88, July 1983, pp. 5657–5667.

[9] B. Streetman and M. A. Peck, "New Synchronous Orbits Using the Geomagentic Lorentz Force," AIAA Journal of Guidance, Control, and Dynamics, Vol. 30, Nov.–Dec. 2007, pp. 1677–1690.

[10] B. Streetmann and M. A. Peck, "Gravity-Assist Manuvers Augmented by the Lorentz Force," Journal of Guidence, Control, and Dynamics, Vol. 32, October 2009.

[11] Y. Yan, X. Huang, and Y. Yang, Dynamics and Control of Lorentz-Augmented Spacecraft Relative Motion. Springer, 2017.

[12] S. Kawamoto, T. Makida, F. Sasaki, Y. Okawa, and S. i. Nishida, "Precise numerical simulations of electrodynamic tethers for an active debris removal system," Acta Astronautica, Vol. 59, No. 1–5, 2006, pp. 139 – 148, 10.1016/j.actaastro.2006.02.035.

[13] Y. Ishige, S. Kawamoto, and S. Kibe, "Study on electrodynamic tether system for space debris removal," Acta Astronautica, Vol. 55, No. 11, 2004, pp. 917 – 929, https://doi.org/10.1016/j.actaastro.2004.04.015.

[14] D. Ferguson, R. Hoffmann, R. Cooper, and J. Hughes, "1997-2002 Solar Array String failures revisited," Journal of Spacecraft and Rockets, Vol. 54, No. 3, 2017, pp. 542–553.

[15] S. N. Paul and C. Früh, "Space Debris Charging and its Effect on Orbit Evolution," Journal of Guidance, Control, and Dynamics, Vol. 0, 2017, pp. 1–19.

[16] J. Hughes and H. Schaub, "Rapid Charged Geosynchronous Debris Perturbation Modeling of Electrodynamic Disturbances," Journal of Astronautical Sciences, Vol. 65, June 2018, pp. 135–156.

[17] J. Hughes and H. Schaub, "Space Weather Influence on Electromagnetic Geosynchronous Debris Perturbations Using Statistical Fluxes," AGU Space Weather, Vol. 16, No. 4, 2018, pp. 391–405, 10.1002/2017sw001768.

[18] T. Schildknecht, R. Muscia, M. Plonera, G. Beutlera, W. Fluryb, J. Kuuselac, J. d. Leon Cruzd, and L. d. Fatima Dominguez Palmerod, "Optical observations of space debris in GEO and in highly-eccentric orbits," Advances in Space Research, 2004, pp. 901–911.

[19] W. E. Wiesel, "Estimating Nongravitational Accelerations on High Area to Mass Ratio Objects," Journal of Guidance, Control, and Dynamics, Vol. 39, June 2016.

[20] T. Schildknecht, R. Musci, C. Frueh, and M. Ploner, "Color Photometry and Light Curve Observations of Space Debris in GEO," Procedings of the Internaitonal Astronautical Congress, 2008.

[21] J. A. Dever, K. K. d. Groh, J. A. Townsend, and J. A. Townsend, "Mechanical Properties Degradation of Teflon FEP returned from the Hubble Space Telescope," 36th Aerospace Sciences Meeting and Exhibit (A. I. o. Aeronautics and Astronautics, eds.), 1998.

[22] P. V. Anderson and H. Schaub, "Local Orbital Debris Flux Study in the Geostationary Ring," Advances in Space Research, Vol. 51, No. 12, 2013, pp. 2195–2206, 10.1016/j.asr.2013.01.019.

[23] P. Chrystal, D. McKnight, P. L. Meredith, J. Schmidt, M. Fok, and C. Wetton, "Space Debris: On Collision Course for Insurers?," Tech. Rep. 1504360-11-en, Swiss Reinsurance Company Ltd, Zürich, Switzerland, March 2011.

[24] S. I. Association, "State of the Satellite Industry Report," tech. rep., Bryce Space and Technology, 2017.

[25] T. Yasaka, T. Hanada, and H. Hirayama, "GEO Debris Environment: A Model to Forecast the next 100 years," Advances in Space Research, Vol. 23, No. 1, 1999, pp. 191–199.

[26] IADC Proceedings of 15th Inter-Agency Space Debris Coordination Committee Meeting, NASA JSC, Houston, TX, 1997.

[27] N. L. Johnson, "Protecting the GEO environment: policies and practices," Space Policy, Vol. 15, No. 3, 1999, pp. 127–135.

[28] R. Jehn, V. Agapov, and C. Hernández, "The situation in the geostationary ring," Advances in Space Research, Vol. 35, No. 7, 2005, pp. 1318–1327.

[29] H. Schaub, L. E. Z. Jasper, P. Anderson, and D. S. McKnight, "Cost and risk assessment for spacecraft operation decisions caused by the space debris environment," Acta Astronautica, Vol. 113, August–September 2015, pp. 66–79, 10.1016/j.actaastro.2015.03.028.

[30] P. V. Anderson and H. Schaub, "Local Debris Congestion in the Geosynchronous Environment With Population Augmentation," Acta Astronautica, Vol. 94, Feb., 2014, pp. 619–628.

[31] D. Oltrogge and T. Kelso, "Getting to know our space population from the public catalog," Astrodynamics Specialist Conference, Girdwood, AK, USA, 2011.

[32] D. S. McKnight and F. R. D. Pentino, "New insights on the orbital debris collision hazard at GEO," Acta Astronautica, Vol. 85, April–May 2013, pp. 73–82, 10.1016/j.actaastro.2012.12.006.

[33] D. McKnight, "Pay me now or pay me more later: start the development of active orbital debris removal now," advanced Maui optical and space surveillance technologies conference, 2010.

[34] D. L. Oltrogge, S. Alfano, C. Law, A. Cacioni, and T. S. Kelso, "A Comprehensive Assessment of Collision Likelihood in Geosynchronous Earth Orbit," International Astronautical Congress, Adelaide, Australia, Sept. 25–29 2017.

[35] L. Anselmo and C. Pardini, "Analysis of the Consequences in Low Earth Orbit of the Collision Between Cosmos 2251 and Iridium 33," 21st International Symposium on Space Flight Dynamics, Toulouse, France, Sept. 28 – Oct. 2 2009.

[36] T. Kelso, "Analysis of the Iridium 33 - Cosmos 2251 Collision," Proceedings of the Advanced Maui Optical and Space Surveillance Technologies Conference, Wailea, Maui, Hawaii,, September 2009.

[37] E. Carlson, S. Casali, D. Chambers, G. Geissler, A. Lalich, M. Leipold, R. Mach, J. Parry, and F. Weems, "Final design of a space debris removal system," NASA STI/Recon Technical Report N, Vol. 92, Dec. 1990, p. 25382.

[38] J. Reed and S. Barraclough, "Development of harpoon system for capturing space debris," 6th European Conference on Space Debris, Vol. 723, 2013.

[39] R. Dudziak, S. Tuttle, and S. Barraclough, "Harpoon technology development for the active removal of space debris," Advances in Space Research, Vol. 56, No. 3, 2015, pp. 509–527.

[40] J. J. Loughman, "Overview and analysis of the SOLDIER satellite concept for removal of space debris," AIAA Space 2010 Conference and Exposition, 2010.

[41] K. Wormnes, R. Le Letty, L. Summerer, R. Schonenborg, O. Dubois-Matra, E. Luraschi, A. Cropp, H. Krag, and J. Delaval, "ESA technologies for space debris remediation," Proceedings of the 6th IAASS Conference: Safety is Not an Option, 2013, pp. 3–4.

[42] J. L. Forshaw, G. S. Aglietti, T. Salmon, I. Retat, M. Roe, C. Burgess, T. Chabot, A. Pisseloup, A. Phipps, C. Bernal, et al., "Final payload test results for the RemoveDebris active debris removal mission," Acta Astronautica, 2017.

[43] L. E. Z. Jasper and H. Schaub, "Input Shaped Large Thrust Maneuver With A Tethered Debris Object," 6th European Conference on Space Debris, Darmstadt, Germany, ESOC, April 22–25 2013. Paper No. 6a.O-11.

[44] L. E. Z. Jasper, C. R. Seubert, H. Schaub, V. Trushlyakov, and E. Yutkin, "Tethered Tug for Large Low Earth Orbit Debris Removal," AAS/AIAA Spaceflight Mechanics Meeting, Charleston, South Carolina, Jan. 29 – Feb. 2 2012. Paper AAS 12-252.

[45] L. Jasper and H. Schaub, "Input shaped large thrust maneuver with a tethered debris object," Acta Astronautica, Vol. 96, 2014, pp. 128–137.

[46] S.-I. Nishida, S. Kawamoto, Y. Okawa, F. Terui, and S. Kitamura, "Space debris removal system using a small satellite," Acta Astronautica, Vol. 65, No. 1, 2009, pp. 95–102.

[47] S.-I. Nishida and N. Kikuchi, "A Scenario and Technologies for Space Debris Removal," 12th International Symposium on Artificial Intelligence, Robotics and Automation in Space, i-SAIRAS, Vol. 14, 2014.

[48] M. M. Castronuovo, "Active space debris removal–A preliminary mission analysis and design," Acta Astronautica, Vol. 69, 2011, pp. 848–859.

[49] D. A. Smith, C. Martin, M. Kassebom, H. Petersen, A. Shaw, B. Skidmore, D. Smith, H. Stokes, and A. Willig, "A mission to preserve the geostationary region," Advances in Space Research, Vol. 34, No. 5, 2004, pp. 1214 – 1218, 10.1016/j.asr.2003.02.042.

[50] J. A. Lennon, C. G. Henshaw, and W. Purdy, "An Architecture for Autonomous Control of a Robotic Satellite Grappling Missino," AIAA Guidance, Navigation and Control Conference, Honolulu, Hawaii, Aug. 18–21 2008. Paper No. AIAA 2008-7259.

[51] P. Couzin, F. Teti, and R. Rembala, "Active Removal of Large Debris : Rendezvous and Robotic Capture Issues," 2nd European Workshop on Active Debris Removal, Paris, France, 2012. Paper #7.5.

[52] Y. S. Karavaev, R. M. Kopyatkevich, M. N. Mishina, G. S. Mishin, P. G. Papushev, and P. N. Shaburov, "The dynamic properties of rotation and optical characteristics of space debris at geostationary orbit," Advances in the Astronautical Sciences, Vol. 119, 2004.

[53] L. DeLuca, F. Bernelli, F. Maggi, P. Tadini, C. Pardini, L. Anselmo, M. Grassi, D. Pavarin, A. Francesconi, F. Branz, S. Chiesa, N. Viola, C. Bonnal, V. Trushlyakov, and I. Belokonov, "Active space debris removal by a hybrid propulsion module," Acta Astronautica, Vol. 91, 2013, pp. 20–33, 10.1016/j.actaastro.2013.04.025.

[54] R. Schonenborg and H. Schoyer, "Solid Propulsion De-Orbiting and Re-Orbiting," European Conference on Space Debris, Germany, 2009.

[55] M. Vetrisano, N. Thiry, and M. Vasile, "Detumbling large space debris via laser ablation," Aerospace Conference, 2015 IEEE, IEEE, 2015, pp. 1–10.

[56] N. Ortiz Gomez and S. J. I. Walker, "Eddy Currents applied to de-tumbling of space debris: feasibility analysis, design and optimization aspects," Acta Astronautica, Vol. 114, 2015, pp. 34–53.

[57] C. Bombardelli and J. Pelaez, "Ion Beam Shepherd for Contactless Space Debris Removal," AIAA Journal of Guidance, Control, and Dynamics, Vol. 34, May–June 2011, pp. 916–920, 10.2514/1.51832.

[58] S. Kitamura, "Large Space Debris Reorbiter using Ion Beam Irradiation," 61st International Astronautical Congress, Prague, Czech Republic, Sept. 27 – Oct. 1 2010.

[59] J. Berryman and H. Schaub, "Analytical Charge Analysis for 2- and 3-Craft Coulomb Formations," AIAA Journal of Guidance, Control, and Dynamics, Vol. 30, Nov.–Dec. 2007, pp. 1701–1710.

[60] E. Hogan and H. Schaub, "Collinear Invariant Shapes for Three-Craft Coulomb Formations," Acta Astronautica, Vol. 12, March–April 2012, pp. 78–89, 10.1016/j.actaastro.2011.10.020.

[61] P. D. Jasch, E. A. Hogan, and H. Schaub, "Out-of-Plane Stability Analysis of Collinear Spinning Three-Craft Coulomb Formations," Acta Astronautica, Vol. 88, July–Aug. 2012, pp. 89–97.

[62] L. B. King, G. G. Parker, S. Deshmukh, and J.-H. Chong, "Study of Interspacecraft Coulomb Forces and Implications for Formation Flying," AIAA Journal of Propulsion and Power, Vol. 19, May–June 2003, pp. 497–505.

[63] H. Schaub and L. E. Z. Jasper, "Orbit Boosting Maneuvers for Two-Craft Coulomb Formations," AIAA Journal of Guidance, Control, and Dynamics, Vol. 36, Jan. – Feb. 2013, pp. 74–82.

[64] H. Schaub and D. F. Moorer, "Geosynchronous Large Debris Reorbiter: Challenges and Prospects," The Journal of the Astronautical Sciences, Vol. 59, No. 1–2, 2014, pp. 161–176.

[65] H. Schaub and Z. Sternovsky, "Active Space Debris Charging for Contactless Electrostatic Disposal Maneuvers," 6th European Conference on Space Debris, Darmstadt, Germany, ESOC, April 22–25 2013. Paper No. 6b.O-5.

[66] T. Bennett, D. Stevenson, E. Hogan, L. McManus, and H. Schaub, "Prospects and Challenges of Touchless Debris Despinning Using Electrostatics," 3rd European Workshop on Space Debris Modeling and Remediation, CNES, Paris, June 16–18 2014.

[67] D. Stevenson and H. Schaub, "Multi-Sphere Method for Modeling Electrostatic Forces and Torques," Advances in Space Research, Vol. 51, Jan. 2013, pp. 10–20, 10.1016/j.asr.2012.08.014.

[68] D. Stevenson and H. Schaub, "Rotational Testbed for Coulomb Induced Spacecraft Attitude Control," 5th International Conference on Spacecraft Formation Flying Missions and Technologies, Münich, Germany, May 29–31 2013.

[69] T. Bennett and H. Schaub, "Touchless Electrostatic Three-Dimensional Detumbling of Large GEO Debris," AAS/AIAA Spaceflight Mechanics Meeting, Jan. 26–30 2014.

[70] S. T. Lai, Fundamentals of Spacecraft Charging: Spacecraft Interactions with Space Plasmas. Princeton University Press, 2011.

[71] D. E. Hastings and H. B. Garrett, Spacecraft-Environment Interactions. Cambridge University Press, 1996.

[72] S. T. Lai, "An overview of electron and ion beam effects in charging and discharging to spacecraft," IEEE Transactions on Nuclear Science, Vol. 36, Dec 1989, pp. 2027 – 2032.

[73] H. Schaub and Z. Sternovsky, "Active Space Debris Charging for Contactless Electrostatic Disposal Maneuvers," Advances in Space Research, Vol. 53, 2013, pp. 110–118.

[74] E. A. Hogan and H. Schaub, "Impacts of Hot Space Plasma and Ion Beam Emission on Electrostatic Tractor Performance," IEEE Transactions on Plasma Science, Vol. 43, No. 9, 2014, pp. 3115–3129.

[75] E. Hogan and H. Schaub, "Space Weather Influence on Relative Motion Control using the Touchless Electrostatic Tractor," Journal of Astronautical Sciences, Vol. 63, No. 3, 2016, pp. 237–262.

[76] D. Stevenson, Remote Spacecraft Attitude Control by Coulomb Charging. PhD thesis, University of Colorado Boulder, 2015.

[77] B. T. Draine and E. E. Salpeter, "On the physics of dust grains in hot gas," Astrophysical Journal, Vol. 231, July 1979, pp. 77–94, 10.1086/157165.

[78] C. R. Seubert, L. A. Stiles, and H. Schaub, "Effective Coulomb Force Modeling For Spacecraft In Earth Orbit Plasmas," Advances in Space Research, 2014.

[79] D. J. Griffiths, Introduction to Electrodynamics. Prentice Hall, 3rd ed., 1999.

[80] J. D. Jackson, Classical Electrodynamics. John Wiley & Sons, 1999.

[81] P. Metzger and J. Lane, "Electric Potential Due to a System of Conducting Spheres," The Open Applied Physics Journal, Vol. 2, 2009, pp. 32–48.

[82] J. H. Cover, W. Knauer, and H. A. Maurer, "Lightweight Reflecting Structures Utilizing Electrostatic Inflation," US Patent 3,546,706, October 1966.

[83] M. A. Peck, B. Streetman, C. M. Saaj, and V. Lappas, "Spacecraft Formation Flying using Lorentz Forces," Journal of British Interplanetary Society, Vol. 60, July 2007, pp. 263–267.

[84] M. A. Peck, "Prospects and Challenges for Lorentz-Augmented Orbits," AIAA Guidance, Navigation and Control Conference, San Francisco, CA, August 15–18 2005. Paper No. AIAA 2005-5995.

[85] L. B. King, G. G. Parker, S. Deshmukh, and J.-H. Chong, "Spacecraft Formation-Flying using Inter-Vehicle Coulomb Forces," tech. rep., NASA/NIAC, January 2002.

[86] E. Kong, D. W. Miller, and R. J. Sedwick, "Exploiting Orbital Dynamics for Aperture Synthesis using Distributed Satellite Systems," Proceedings of the AAS/AIAA Spaceflight Mechanics Meeting, Breckenridge, CO, Feb. 7–10 1999, pp. 385–301. Paper AAS-99-112.

[87] H. Schaub, G. G. Parker, and L. B. King, "Challenges and Prospect of Coulomb Spacecraft Formation Control," Journal of the Astronautical Sciences, Vol. 52, Jan.–June 2004, pp. 169–193.

[88] A. Natarajan and H. Schaub, "Linear Dynamics and Stability Analysis of a Coulomb Tether Formation," AIAA Journal of Guidance, Control, and Dynamics, Vol. 29, July–Aug. 2006, pp. 831–839.

[89] H. Schaub, C. Hall, and J. Berryman, "Necessary Conditions for Circularly-Restricted Static Coulomb Formations," Journal of the Astronautical Sciences, Vol. 54, July-Dec. 2006, pp. 525–541.

[90] H. Vasavada and H. Schaub, "Analytic Solutions for Equal Mass Four-Craft Static Coulomb Formation," Journal of the Astronautical Sciences, Vol. 56, Jan. – March 2008, pp. 17–40.

[91] D. F. Moorer and H. Schaub, "Hybrid Electrostatic Space Tug," US Patent 0036951-A1, Feb. 17 2011.

[92] D. F. Moorer and H. Schaub, "Electrostatic Spacecraft Reorbiter," US Patent 8,205,838 B2, Feb. 17 2011.

[93] E. A. Hogan, "Impacts of Tug and Debris Sizes on Electrostatic Tractor Charging Performance," Advances in Space Research, Vol. 55, Jan 2014, pp. 630–638.

[94] E. Hogan and H. Schaub, "Relative Motion Control for Two-Spacecraft Electrostatic Orbit Corrections," AIAA Journal of Guidance, Control, and Dynamics, Vol. 36, Jan. – Feb. 2013, pp. 240–249.

[95] N. Murdoch, D. Izzo, C. Bombardelli, I. Carnelli, A. Hilgers, and D. Rodgers, "The Electrostatic Tractor for Asteroid Deflection," 58th International Astronautical Congress, 2008. Paper IAC-08-A3.I.5.

[96] J. Hughes and H. Schaub, "Prospects of Using a Pulsed Electrostatic Tractor With Nominal Geosynchronous Conditions," IEEE Transactions on Plasma Science, Vol. 45, No. 8, 2017, pp. 1887–1897.

[97] Y. Lin and D. C. Joy, "A New Examination of Secondary Electron Yield Data," Surface and Interface Analysis, Vol. 57, 2005, pp. 895–900.

[98] M. Denton, M. Thompsen, V. Jordanova, M. Henderson, J. Borovsky, J. Denton, D. Pitchford, and D. Hartley, "An empirical model of electron and ion fluxes derived from observations at geosynchronous orbit," AGU Space Weather, Vol. 13, 2015, pp. 233–249.

[99] J. Hughes and H. Schaub, "Electrostatic Tractor Analysis Using a Measured Flux Model," The 15th Spacecraft Charging Technology Conference, 2018.

[100] J. Hughes and H. Schaub, "Effects of Space Weather on Geosynchronous Electromagnetic Spacecraft Perturbations Using Statistical Fluxes," AGU Fall Meeting, New Orleans, LA, Dec 11 – 15 2017.

[101] V. Davis and M. J. Mandell, Plasma Interactions with Spacecraft. Volume 2, NASCAP-2K Scientific Documentation for Version 4.1. Science Applications International Corp, 4.1 ed., 2011.

[102] V. Davis, B. Gardner, M. Mandell, and K. Wilcox, NASCAP-2k User's Manual. Science Applications International Corporation, San Diego, CA 92121, 4.1 ed., Febuary 2011.

[103] J. E. Borovsky, T. E. Cayton, M. H. Denton, R. D. Belian, R. A. Christensen, and J. C. Ingraham, "The proton and electron radiation belts at geosynchronous orbit: Statistics and behavior during high-speed stream-driven storms," Journal of Geophysical Research: Space Physics, Vol. 121, 2016, doi:10.1002/ 2016JA022520.

[104] I. Katz, D. E. Parks, M. Mandell, J. M. Harvey, D. H. Brownell, S. Wang, and M. Rotenberg, "A Three Dimensional Dynamic Study of Electrostatic Charging in Materials," tech. rep., Systems, Science, and Software, 1977.

[105] D. Ferguson, R. Hilmer, and V. Davis, "Best Geosyncronous Earth Orbit Daytime Scpacecraft Charging Index," Journal of Spacecraft and Rockets, Vol. 52, No. 2, 2015.

[106] W. R. Smythe, Static and Dynamic Electricity. McGraw–Hill, 3rd ed., 1968.

[107] J. Hughes and H. Schaub, "Orbital and Storm Time Analysis of the Pulsed Electrostatic Tractor," European Conference on Space Debris, ESOC, Darmstadt, Germany, April 18 – 21 2017.

[108] M. Gussenhoven, E. Mullen, and D. Hardy, "Artificial Charging of Spacecraft due to Electron Beam Emission," IEEE Transactions on Nuclear Science, Vol. NS-34, No. 6, 1987.

[109] G. W. Schnueller, M. J. Mandell, D. E. Parks, P. G. Steen, J. J. Cassidey, I. Katz, and A. Rubin, "Charging Analysis of the SCATHA Satellite," Tech. Rep. NAS3-21050, Air Force Geophysics Laboratory, 1979, SCATHA.

[110] N. Balcon, D. Payan, M. Belhaj, T. Tondu, and V. Inguimbert, "Secondary Electron Emission on Space Materials: Evaluation of the Total Secondary Electron Yield From Surface Potential Measurements," IEEE Transactions on Plasma Science, Vol. 40, No. 2, 2012.

[111] H. B. Garrett, "Review of Quantitative Models of the 0 to 1 keV Near-Earth Plasma," Reviews of Geophysics and Space Physics, Vol. 17, May 1979, pp. 397 – 417.

[112] J. Maxwell, A Treatise on Electricity and Magnetism. Oxford University Press, 1893.

[113] J. Lekner, "Electrostatics of two charged conducting spheres," Procedings of the Royal Society, Vol. 468, 2012, pp. 2829–2848.

[114] S. Price, A. Stone, and M. Alderton, "Explicit formulae for the electrostatic energy, forces and torques between a pair of molecules of arbitrary symmetry," Molecular Physics, Vol. 52, No. 4, 1984.

[115] X. Hou, D. J. Scheeres, and X. Xin, "Mutual potential between two rigid bodies with arbitrary shapes and mass distributions," Celestial Mechanics and Dynamical Astronomy, 2016, pp. 1–27.

[116] J. Hughes and H. Schaub, "Appropriate Fidelity Electrostatic Force Evaluation Considering a Range of Spacecraft Separations," AAS/AIAA Spaceflight Mechanics Meeting, Feb. 14–18 2016.

[117] H. Schaub and J. L. Junkins, Analytical Mechanics of Space Systems. Reston, VA: AIAA Education Series, 2nd ed., October 2009.

[118] D. C. Giancoli, Physics for Scientists and Engineers. Pearson Prentice Hall, 2008.

[119] D. Stevenson and H. Schaub, "Multi Sphere Modeling for Electrostatic Forces on Three-Dimensional Spacecraft Shapes," AAS/AIAA Spaceflight Mechanics Meeting, Charleston, South Carolina, Jan. 29 – Feb. 2 2012.

[120] D. Stevenson and H. Schaub, "Optimization of Sphere Population for Electrostatic Multi Sphere Model," IEEE Transactions on Plasma Science, 2013.

[121] R. Bauer, "Distribution of Points on a Sphere with Application to Star Catalogs," Journal of Guidance Control and Dynamics, Vol. 23, No. 1, 2000, pp. 130–137.

[122] R. Harrington, Field Computation by Moment Methods. Wiley IEEE, 1968.

[123] R. H. Alad and S. Chakrabarty, "Electrostatic Analysis of an Artificial Orbiting Satellite for Absolute Charging," IEEE Transactions on Plasma Science, Vol. 43, September 2015, pp. 2887 – 2893.

[124] B. Karthikeyan, V. K. Hariharan, and S. Sanyal, "Estimation of Free Space Capacitance and Body Potential of a Spacecraft for Charging Analysis," IEEE Transactions on Plasma Science, Vol. 41, December 2013, pp. 3487 – 3491.

[125] S. Chakrabarty, "Absolute charging analysis of space-craft bodies using method of moments (MoM)," IEEE Applied Electromagnetics Conference (AEMC), 2015, doi: 10.1109/AEMC.2015.7509140.

[126] P. D. Mehta and S. B. Chakrabarty, "Capacitance of Dielectric-Coated Metallic Bodies Isolated in Free Space," Electromagnetics, Vol. 31, No. 4, 2011, pp. 294 – 314.

[127] J. Hughes and H. Schaub, "Spacecraft Electrostatic Force And Torque Expansions Yielding Appropriate Fidelity Measures," AAS Spaceflight Mechanics Meeting, San Antonio, TX, Feb. 5–9 2017.

[128] D. K. Reitan and T. J. Higgins, "Accurate Determination of the Accurate Determination of the Capacitance of a Thin Rectangular Plate," Transactions of the American Institute of Electrical Engineers, Part I: Communication and Electronics, Vol. 75, No. 6, 1957, pp. 761–766.

[129] Y. Chow and M. Yovanovich, "The shape factor of the capacitance of a conductor," Journal of Applied Physics, Vol. 53, No. 8470, 1986.

[130] G. Ingram, J. Hughes, T. Bennett, C. Reily, and H. Schaub, "Autonomous Volume Multi-Sphere-Model Development Using Electric Field Matching," AAS Spaceflight Mechanics Meeting, Feb 5–9 2017.

[131] P. Chow, J. Hughes, T. Bennett, and H. Schaub, "Automated Sphere Geometry Optimization For The Volume Multi-Sphere Method," AAS/AIAA Spaceflight Mechanics Meeting, Feb. 14–18 2016.

[132] B. Wie, Space Vehicle Dynamics and Control. Reston, VA: AIAA Education Series, 2nd ed., 2008.

[133] N. A. Tsyganenko, "A Magnetospheric magnetic field model with a warped tail current sheet," Planetary and Space Science, Vol. 37, 1989, pp. 5–20.

[134] D. N. D. G. Allen and S. C. R. Dennis, "The Application of Relaxiation Methods to the Solution of Differential Equations in Three Dimensions," Quarterly Journal of Mechanics and Applied Mathematics, Vol. 6, 1953, p. 87.

[135] D. C. Ferguson, W. F. Denig, and J. V. Rodriguez, "Plasma Conditions During the Galaxy 15 Anomaly and the Possibility of ESD from Subsurface Charging," AIAA Aerospace Sciences Meeting including the New Horizons Forum and Aerospace Exposition, Orlando, FL, January 4–7 2011. Paper AIAA 2011-1061.

[136] H. Volland, "A semiemperical Model of Large-Scale Magnetospheric Electric Fields," Journal of Geophysical Research, Vol. 78, No. 1, 1973.

[137] D. P. Stern, "the Motion of a Proton in the Equatorial Magnetosphere," Journal of Geophysical Research, Vol. 90, No. 4, 1975.

[138] H. Korth, M. F. Thomsen, J. E. Borovsky, and D. J. McComas, "Plasma sheet access to geosynchronous orbit," Journal of Geophysical Research, Vol. 104, No. A11, 1999, pp. 25047–25062, 10.1029/1999JA900292.

[139] N. M. A. Chen, "Isolated Cold Plasma Regions: Observations and Their Relation to Possible Production Mechamisms," Journal of Geophysical Research, Vol. 80, No. 7, 1975.

[140] K. H. Bhavnani and R. Vancour, "Coordinate Systems for Space and Geophysical Applications," tech. rep., Phillips Laboratory, Air Force Systems Command, 1991.

[141] J. Hughes and H. Schaub, "Rapid Charged Geosynchronous Debris Perturbation Modeling Of Electromagnetic Disturbances," AAS Spaceflight Mechanics Meeting, Feb 5–9 2017.

[142] J. Hughes and H. Schaub, "Charged Geosynchronous Debris Perturbation Using Rapid Electromagnetic Force and Torque Evaluation," Advanced Maui Optical and Space Surveillance Technologies Conference, 2016, p. 86.

[143] M. Finckenor, "Multilayer Insulation Material Guidelines," tech. rep., NASA Marshall Space Flight Center, 1999.

[144] D. Schrage, L. Yough, B. Campbell, J. Billen, T. Wangler, J. Stovall, F. Martinez, W. Clark, S. Gibbs, G. Bolme, P. O'Shea, M. Lynch, J. Devenport, J. Rathke, R. Micich, J. Rose, R. Richter, and G. Rosato, "A Flight-Qualified RFQ for the BEAR Project," Linear Accelerator Conference, Williamsburg, VA, Oct. 3-7 1988, pp. 54–57.

[145] P. O'Shea, T. Butler, M. Lynch, K. McKenna, M. Fongratz, and T. Zaugg, "A Linear Accelerator in Space–the Beam Experiment Aboard Rocket," Linear Accelerator Conference, Albuquerque, NM, Sept. 10-14 1990, pp. 739–742.

[146] R. Harris, Modern Physics. Pearson, 1998.

[147] B. Macomber, D. Conway, K. A. Cavalieri, C. Moody, and J. L. Junkins, "LASR CV: Vision-Based Relative Navigation and Proximity Operations Pipeline," Advances in Astronautical Sciences, Guidence, Navigation, and Control, Vol. 151, 2014.

[148] D. M. e. al., "Validation of Astrodynamic Formation Flying Models Against SPACE-SI Experiments with Prisma Satellites," 26th Annual AIAA/USU Conference on Small Satellites, Logan, UT, 2012.

[149] M. H. Denton, M. F. Thomsen, H. Korth, S. Lynch, J. C. Zhang, and M. W. Liemohn, "Bulk plasma properties at geosynchronous orbit," Journal of Geophysical Research, Vol. 110, July 2005, 10.1029/2004JA010861.

Appendix A

AFM Force and Torque Derivation

Consider two charged, conducting neighboring spacecraft as is shown in Figure A.1 with a known charge distribution. This later assumption is relaxed later in the development to assume that only the potentials and relative attitude and separation are known. They each experience a force and torque due to the other's charge. The force and torque on body 2 is found by integrating the differential force, which is a function of body 1's charge distribution, across body 2.

$$\mathrm{d}\boldsymbol{F}_2 = \frac{\mathrm{d}q_1 \mathrm{d}q_2 \boldsymbol{R}}{4\pi\epsilon_0 R^3} \tag{A.1}$$

where $\boldsymbol{R}$ points from $\mathrm{d}q_1$ to $\mathrm{d}q_2$. The separation vector is expressed from body vectors and a vector between the center of mass of each body $\boldsymbol{R} = \boldsymbol{R}_c + \boldsymbol{r}_2 - \boldsymbol{r}_1$. Using this substitution makes the differential force

$$\mathrm{d}\boldsymbol{F}_2 = \frac{\mathrm{d}q_1 \, \mathrm{d}q_2 \, \boldsymbol{R}_c + \boldsymbol{r}_2 - \boldsymbol{r}_1}{4\pi\epsilon_0 \, ||\boldsymbol{R}_c + \boldsymbol{r}_2 - \boldsymbol{r}_1||^3} \tag{A.2}$$

Where ϵ_0 is the permittivity of free space, $\epsilon_0 \approx 8.854187 * 10^{-12}$ F/m. The differential force is approximated by binomially expanding the denominator and truncating higher-order terms on the assumption that the body radii ($\boldsymbol{r}_1$ and $\boldsymbol{r}_2$) are small compared to their separation ($\boldsymbol{R}_c$). The differential force is approximated using a binomial series if the denominator is first written as a scalar, assuming that R_c is larger than r_1 or r_2, and lumping all small terms into the variable x.

$$\frac{1}{||\boldsymbol{R}_c + \boldsymbol{r}_2 - \boldsymbol{r}_1||^3} = (R_c^2 + r_1^2 + r_2^2 + 2(\boldsymbol{R}_c \cdot \boldsymbol{r}_2 - \boldsymbol{R}_c \cdot \boldsymbol{r}_1 - \boldsymbol{r}_2 \cdot \boldsymbol{r}_1))^{-3/2} \tag{A.3}$$

$$= \frac{1}{R_c^3}\left[1 + \left(\frac{r_2^2}{R_c^2} + \frac{r_1^2}{R_c^2} + \frac{2}{R_c^2}(\boldsymbol{R}_c \cdot \boldsymbol{r}_2 - \boldsymbol{R}_c \cdot \boldsymbol{r}_1 - \boldsymbol{r}_2 \cdot \boldsymbol{r}_1)\right)\right]^{-3/2} \quad = \frac{1}{R_c^3}(1+x)^{-3/2} \tag{A.4}$$

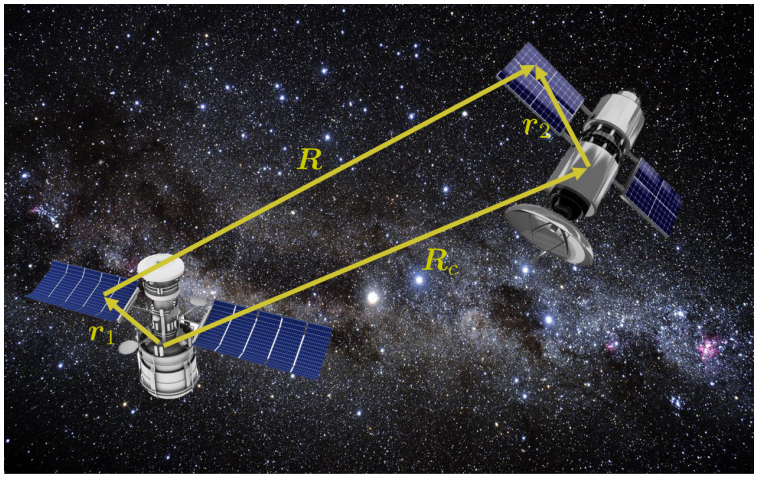

Figure A.1: Coordinate system for inter-craft derivation

Expand the denominator to second order using a binomial series $(1+x)^{-3/2} \approx 1 - \frac{3}{2}x + \frac{15}{8}x^2$ and reassemble to approximate the differential force as:

$$\mathrm{d}\boldsymbol{F}_2 = \frac{\mathrm{d}q_1\,\mathrm{d}q_2}{4\pi\epsilon_0 R_c^3}(\boldsymbol{R}_c + \boldsymbol{r}_2 - \boldsymbol{r}_1)\left(1 - \frac{3r_1^2}{2R_c^2} - \frac{3r_2^2}{2R_c^2} - \frac{3(\boldsymbol{R}_c\cdot\boldsymbol{r}_2 - \boldsymbol{R}_c\cdot\boldsymbol{r}_1 - \boldsymbol{r}_2\cdot\boldsymbol{r}_1)}{R_c^2} + \frac{15((\boldsymbol{R}_c\cdot\boldsymbol{r}_2)^2 + (\boldsymbol{R}_c\cdot\boldsymbol{r}_1)^2 - (\boldsymbol{R}_c\cdot\boldsymbol{r}_1)(\boldsymbol{R}_c\cdot\boldsymbol{r}_2))}{2R_c^4}\right) \quad \text{(A.5)}$$

This differential is integrated over the entire body to obtain the net electrostatic force on this object, or crossed with the body position vector and integrated over the body to obtain torque.

A.1 Fundamental AFM Expansion Terms Definition

The problem of two charged bodies interacting through electrostatics is similar to two massive bodies interacting through gravity. Just as moments of the mass distribution play a key role in solving the gravitational two-body problem [115], moments of the charge distribution play a key role in predicting electrostatic force and torque. Three especially important moments of the charge distribution are identified and named here:

$$Q = \int_B \mathrm{d}q \qquad \boldsymbol{q} = \int_B \boldsymbol{r}\,\mathrm{d}q \qquad [Q] = \int_B -[\tilde{\boldsymbol{r}}][\tilde{\boldsymbol{r}}]\,\mathrm{d}q \quad \text{(A.6)}$$

Q is a scalar and is the total charge, $\boldsymbol{q}$ is a 3×1 vector and is defined as the dipole moment, and $[Q]$ is a 3×3 tensor defined as the charge tensor. The vector $\boldsymbol{r}$ points from the center of mass

to the differential charge dq, and $[\tilde{\boldsymbol{r}}]$ is the matrix form of the vector cross product: $\boldsymbol{a} \times \boldsymbol{b} = [\tilde{\boldsymbol{a}}]\boldsymbol{b}$. If the gravity analogy is used, the total charge Q is similar to the total mass, the dipole moment $\boldsymbol{q}$ is similar to the total mass multiplied by the offset between the center of a coordinate system and the true center of mass, and the charge tensor $[Q]$ is similar to the inertia tensor. The dipole moment $\boldsymbol{q}$ provides a measure of where the center of charge is in relation to the center of mass. If $\boldsymbol{q}$ is zero, then the center of charge and mass locations are identical. To relate these AFM terms to the variables commonly used in multipole expansions, Q and $\boldsymbol{q}$ are the mono and dipole terms, and the charge tensor $[Q]$ defined here is related to the quadrupole $[Q_p]$ by $[Q_p] = -3[Q] + 2\text{tr}([Q])$ [80].

A.2 Inter-Craft Electrostatic Reactions

This section derives the force and torque on body 2 due the charge on body 1 and 2. This is done using the 2nd order binomial expansion for the denominator of the differential force.

A.2.1 Force Derivation

The total force on body 2 is found by integrating the differential force over the entire body

$$\boldsymbol{F}_2 = \frac{1}{4\pi\epsilon_0 R_c^3} \int_{B_1} \int_{B_2} (\boldsymbol{R}_c + \boldsymbol{r}_2 - \boldsymbol{r}_1)\Bigg(1 - \frac{3r_1^2}{2R_c^2} - \frac{3r_2^2}{2R_c^2} - \frac{3(\boldsymbol{R}_c \cdot \boldsymbol{r}_2 - \boldsymbol{R}_c \cdot \boldsymbol{r}_1 - \boldsymbol{r}_2 \cdot \boldsymbol{r}_1)}{R_c^2} + \frac{15((\boldsymbol{R}_c \cdot \boldsymbol{r}_2)^2 + (\boldsymbol{R}_c \cdot \boldsymbol{r}_1)^2 - (\boldsymbol{R}_c \cdot \boldsymbol{r}_1)(\boldsymbol{R}_c \cdot \boldsymbol{r}_2))}{2R_c^4}\Bigg)\text{d}q_2\text{d}q_1 \quad \text{(A.7)}$$

This equation is broken into three parts: the terms resulting from the $\boldsymbol{R}_c, \boldsymbol{r}_1$, and $\boldsymbol{r}_2$ which are denotes as $\boldsymbol{F}_{2_0}, \boldsymbol{F}_{2_1}$ and $\boldsymbol{F}_{2_2}$, respectively. The first term $\boldsymbol{F}_{2_0}$ is expressed as

$$\begin{aligned}\boldsymbol{F}_{2_0} =& \frac{\boldsymbol{R}_c}{4\pi\epsilon_0 R_c^3}\int_{B_1}\int_{B_2}\left(1-\frac{3r_1^2}{2R_c^2}-\frac{3r_2^2}{2R_c^2}-\frac{3(\boldsymbol{R}_c\cdot\boldsymbol{r}_2-\boldsymbol{R}_c\cdot\boldsymbol{r}_1-\boldsymbol{r}_2\cdot\boldsymbol{r}_1)}{R_c^2}+\right.\\ &\left.\frac{15((\boldsymbol{R}_c\cdot\boldsymbol{r}_2)^2+(\boldsymbol{R}_c\cdot\boldsymbol{r}_1)^2-(\boldsymbol{R}_c\cdot\boldsymbol{r}_1)(\boldsymbol{R}_c\cdot\boldsymbol{r}_2))}{2R_c^4}\right)\mathrm{d}q_2\mathrm{d}q_1\\ =& \frac{\boldsymbol{R}_c}{4\pi\epsilon_0 R_c^3}\left[Q_1Q_2-\left(\frac{3}{2R_c^2}\int_{B_1}r_1^2\,\mathrm{d}q_1\int_{B_2}\mathrm{d}q_2\right)-\left(\frac{3}{2R_c^2}\int_{B_2}r_2^2\,\mathrm{d}q_2\int_{B_1}\mathrm{d}q_1\right)\right.\\ &-\left(\frac{3}{R_c^2}\boldsymbol{R}_c\cdot\int_{B_1}\mathrm{d}q_1\int_{B_2}\boldsymbol{r}_2\mathrm{d}q_2\right)+\left(\frac{3}{R_c^2}\boldsymbol{R}_c\cdot\int_{B_2}\mathrm{d}q_2\int_{B_1}\boldsymbol{r}_1\mathrm{d}q_1\right)\\ &+\left(\frac{3}{R_c^2}\int_{B_1}\boldsymbol{r}_1\mathrm{d}q_2\int_{B_2}\boldsymbol{r}_2\mathrm{d}q_2\right)+\left(\frac{15}{2R_c^4}\int_{B_1}\mathrm{d}q_1\int_{B_2}(\boldsymbol{R}_c\cdot\boldsymbol{r}_2)^2\mathrm{d}q_2\right)\\ &\left.+\left(\frac{15}{2R_c^4}\int_{B_2}\mathrm{d}q_2\int_{B_1}(\boldsymbol{R}_c\cdot\boldsymbol{r}_1)^2\mathrm{d}q_1\right)-\left(\frac{15}{2R_c^4}\int_{B_2}(\boldsymbol{R}_c\cdot\boldsymbol{r}_2)\mathrm{d}q_2\int_{B_1}(\boldsymbol{R}_c\cdot\boldsymbol{r}_1)\mathrm{d}q_1\right)\right]\end{aligned} \tag{A.8}$$

Here the moments of the charge distribution given in Eq. 3.7 are used to simplify the equations. Using the identity $\int r^2\mathrm{d}q = \mathrm{tr}([Q])/2$ to simplify the above equation yields:

$$\begin{aligned}\boldsymbol{F}_{2_0} = \frac{\boldsymbol{R}_c}{4\pi\epsilon_0 R_c^3}\Bigg[&Q_1Q_2-\frac{3Q_2}{4R_c^2}\mathrm{tr}([Q_1])-\frac{3Q_1}{4R_c^2}\mathrm{tr}([Q_2])-\frac{3Q_1}{R_c^2}\boldsymbol{R}_c\cdot\boldsymbol{q}_2\\ &+\frac{3Q_2}{R_c^2}\boldsymbol{R}_c\cdot\boldsymbol{q}_1+\frac{3Q_2}{R_c^2}\boldsymbol{q}_2\cdot\boldsymbol{q}_1+\frac{15Q_1}{2R_c^4}\int_{B_2}(\boldsymbol{R}_c\cdot\boldsymbol{r}_2)^2\mathrm{d}q_2\\ &+\frac{15Q_2}{2R_c^4}\int_{B_1}(\boldsymbol{R}_c\cdot\boldsymbol{r}_1)^2\mathrm{d}q_1-\frac{15}{2R_c^4}(\boldsymbol{R}_c\cdot\boldsymbol{q}_2)(\boldsymbol{R}_c\cdot\boldsymbol{q}_1)\Bigg)\Bigg]\end{aligned} \tag{A.9}$$

To solve the two remaining integrals, apply the vector identity $(\boldsymbol{a}\cdot\boldsymbol{b})\boldsymbol{b} = ([\tilde{\boldsymbol{b}}][\tilde{\boldsymbol{b}}]+b^2[I])\boldsymbol{a}$ to the terms of the form $(\boldsymbol{R}_c\cdot\boldsymbol{r})^2$ and integrate to yield

$$\boldsymbol{R}_c\cdot(\boldsymbol{R}_c\cdot\boldsymbol{r})\boldsymbol{r} = \boldsymbol{R}_c\cdot([\tilde{\boldsymbol{r}}][\tilde{\boldsymbol{r}}]+r^2[I])\boldsymbol{R}_c = \boldsymbol{R}_c^T[\tilde{\boldsymbol{r}}][\tilde{\boldsymbol{r}}]\boldsymbol{R}_c + R_c^2r^2 \tag{A.10}$$

$$\rightarrow -\boldsymbol{R}_c^T[Q]\boldsymbol{R}_c + R_c^2\mathrm{tr}([Q])/2 \tag{A.11}$$

and re-write $\boldsymbol{F}_{2_0}$ finally as:

$$\begin{aligned}\boldsymbol{F}_{2_0} = \frac{\boldsymbol{R}_c}{4\pi\epsilon_0 R_c^3}\Bigg[&Q_1Q_2+\frac{3Q_2}{R_c^2}\mathrm{tr}([Q_1])+\frac{3Q_1}{R_c^2}\mathrm{tr}([Q_2])-\frac{3Q_1}{R_c^2}\boldsymbol{R}_c\cdot\boldsymbol{q}_2+\frac{3Q_2}{R_c^2}\boldsymbol{R}_c\cdot\boldsymbol{q}_1\\ &+\frac{3Q_2}{R_c^2}\boldsymbol{q}_2\cdot\boldsymbol{q}_1-\frac{15Q_1}{2R_c^4}\boldsymbol{R}_c^T[Q_2]\boldsymbol{R}_c-\frac{15Q_2}{2R_c^4}\boldsymbol{R}_c^T[Q_1]\boldsymbol{R}_c-\frac{15}{R_c^4}(\boldsymbol{R}_c\cdot\boldsymbol{q}_2)(\boldsymbol{R}_c\cdot\boldsymbol{q}_1)\Bigg]\end{aligned} \tag{A.12}$$

The second part of the force $\boldsymbol{F}_{2_1}$ is much simpler because many of the terms become third order and are neglected in this second order expansion.

$$\boldsymbol{F}_{2_1} = \frac{1}{4\pi\epsilon_0 R_c^3}\int_{B_1}\int_{B_2}\boldsymbol{r}_2\left(1-\frac{3(\boldsymbol{R}_c\cdot\boldsymbol{r}_2-\boldsymbol{R}_c\cdot\boldsymbol{r}_1)}{R_c^2}\right)\mathrm{d}q_2\mathrm{d}q_1 \tag{A.13}$$

$$= \frac{1}{4\pi\epsilon_0 R_c^3}\left[\int_{B_1}\mathrm{d}q_1\int_{B_2}\boldsymbol{r}_2\mathrm{d}q_2-\frac{3}{R_c^2}\int_{B1}\mathrm{d}q_1\int_{B2}\boldsymbol{r}_2(\boldsymbol{R}_c\cdot\boldsymbol{r}_2)\mathrm{d}q_2+\frac{3}{R_c^2}\int_{B1}\boldsymbol{R}_c\cdot\boldsymbol{r}_1\mathrm{d}q_1\int_{B2}\boldsymbol{r}_2\mathrm{d}q_2\right. \tag{A.14}$$

$$= \frac{1}{4\pi\epsilon_0 R_c^3}\left[Q_1\boldsymbol{q}_2-\frac{3}{R_c^2}Q_1\int_{B2}\boldsymbol{r}_2(\boldsymbol{R}_c\cdot\boldsymbol{r}_2)\mathrm{d}q_2+\frac{3}{R_c^2}(\boldsymbol{R}c\cdot\boldsymbol{q}_1)\boldsymbol{q}_2\right. \tag{A.15}$$

$$= \frac{1}{4\pi\epsilon_0 R_c^3}\left[Q_1\boldsymbol{q}_2-\frac{3}{R_c^2}Q_1(-[Q_2]\boldsymbol{R}_c+\mathrm{tr}([Q_2])/2\boldsymbol{R}_c)+\frac{3}{R_c^2}(\boldsymbol{R}c\cdot\boldsymbol{q}_1)\boldsymbol{q}_2\right. \tag{A.16}$$

$$= \frac{1}{4\pi\epsilon_0 R_c^3}\left[Q_1\boldsymbol{q}_2+\frac{3Q_1}{R_c^2}[Q_2]\boldsymbol{R}_c-\frac{3Q_1}{2R_c^2}\mathrm{tr}([Q_2])\boldsymbol{R}_c+\frac{3(\boldsymbol{R}_c\cdot\boldsymbol{q}_1)}{R_c^2}\boldsymbol{q}_2\right] \tag{A.17}$$

The third part of the force $\boldsymbol{F}_{2_2}$ is similar in form to $\boldsymbol{F}_{2_1}$ with the $\boldsymbol{r}_2$ being replaced with a $-\boldsymbol{r}_1$.

$$\boldsymbol{F}_{2_2} = \frac{1}{4\pi\epsilon_0 R_c^3}\int_{B_1}\int_{B_2}-\boldsymbol{r}_1\left(1-\frac{3(\boldsymbol{R}_c\cdot\boldsymbol{r}_2-\boldsymbol{R}_c\cdot\boldsymbol{r}_1)}{R_c^2}\right)\mathrm{d}q_2\mathrm{d}q_1 \tag{A.18}$$

$$= \frac{1}{4\pi\epsilon_0 R_c^3}\left[-Q_2\boldsymbol{q}_1+\frac{3Q_2}{R_c^2}[Q_1]\boldsymbol{R}_c-\frac{3Q_2}{2R_c^2}\mathrm{tr}([Q_1])\boldsymbol{R}_c+\frac{3(\boldsymbol{R}_c\cdot\boldsymbol{q}_2)}{R_c^2}\boldsymbol{q}_1\right] \tag{A.19}$$

The total force is then expressed as

$$\begin{aligned}\boldsymbol{F}_2 = \frac{1}{4\pi\epsilon_0 R_c^3}\Bigg[&\Bigg(Q_1Q_2+\frac{3Q_2}{2R_c^2}\mathrm{tr}([Q_1])+\frac{3Q_1}{2R_c^2}\mathrm{tr}([Q_2])-\frac{3Q_1}{R_c^2}\boldsymbol{R}_c\cdot\boldsymbol{q}_2+\frac{3Q_2}{R_c^2}\boldsymbol{R}_c\cdot\boldsymbol{q}_1+\frac{3Q_2}{R_c^2}\boldsymbol{q}_2\cdot\boldsymbol{q}_1\\&-\frac{15Q_1}{2R_c^4}\boldsymbol{R}_c^T[Q_2]\boldsymbol{R}_c-\frac{15Q_2}{2R_c^4}\boldsymbol{R}_c^T[Q_1]\boldsymbol{R}_c-\frac{15}{R_c^4}(\boldsymbol{R}_c\cdot\boldsymbol{q}_2)(\boldsymbol{R}_c\cdot\boldsymbol{q}_1)\Bigg)\boldsymbol{R}_c\\&+Q_1\boldsymbol{q}_2+\frac{3Q_1}{R_c^2}[Q_2]\boldsymbol{R}_c+\frac{3(\boldsymbol{R}_c\cdot\boldsymbol{q}_1)}{R_c^2}\boldsymbol{q}_2-Q_2\boldsymbol{q}_1+\frac{3Q_2}{R_c^2}[Q_1]\boldsymbol{R}_c+\frac{3(\boldsymbol{R}_c\cdot\boldsymbol{q}_2)}{R_c^2}\boldsymbol{q}_1\Bigg]\end{aligned} \tag{A.20}$$

This equation is visualized in Table A.1, where the common factor of $4\pi\epsilon_0 R_c^3$ is omitted, allowing easy ordering of terms based on which measures $(Q, \boldsymbol{q}, [Q])$ they incorporate. They are also ordered by the dimensionless ratio r/R_c where r is a characteristic dimension of either spacecraft. As the spacecraft move farther and farther away, the higher order terms in this variable matter less and less. The zeroth order term is in the upper left, the two boxes with two terms each are the first order terms, and the three boxes containing twelve terms along the diagonal are the second order terms. This table allows easy selection of the force terms needed for appropriate fidelity.

Table A.1: Force ordering matrix

	Q_1	$\boldsymbol{q}_1$	$[Q_1]$
Q_2	$Q_1 Q_2 \boldsymbol{R}_c$	$\frac{3Q_2}{R_c^2}(\boldsymbol{R}_c \cdot \boldsymbol{q}_1)\boldsymbol{R}_c - Q_2 \boldsymbol{q}_1$	$\frac{3Q_2}{2R_c^2}\mathrm{tr}([Q_1])\boldsymbol{R}_c$ $-\frac{15Q_2}{2R_c^4}(\boldsymbol{R}_c^T[Q_1]\boldsymbol{R}_c)\boldsymbol{R}_c$ $+\frac{3Q_2}{R_c^2}[Q_1]\boldsymbol{R}_c$
$\boldsymbol{q}_2$	$Q_1 \boldsymbol{q}_2 - \frac{3Q_1}{R_c^2}(\boldsymbol{R}_c \cdot \boldsymbol{q}_2)\boldsymbol{R}_c$	$\frac{3}{R_c^2}(\boldsymbol{q}_2 \cdot \boldsymbol{q}_1)\boldsymbol{R}_c$ $-\frac{15}{R_c^4}(\boldsymbol{R}_c \cdot \boldsymbol{q}_2)(\boldsymbol{R}_c \cdot \boldsymbol{q}_1)\boldsymbol{R}_c$ $+\frac{3(\boldsymbol{R}_c \cdot \boldsymbol{q}_1)}{R_c^2}\boldsymbol{q}_2 + \frac{3(\boldsymbol{R}_c \cdot \boldsymbol{q}_2)}{R_c^2}\boldsymbol{q}_1$	
$[Q_2]$	$\frac{3Q_1}{2R_c^2}\mathrm{tr}([Q_2])\boldsymbol{R}_c$ $-\frac{15Q_1}{2R_c^4}(\boldsymbol{R}_c^T[Q_2]\boldsymbol{R}_c)\boldsymbol{R}_c$ $+\frac{3Q_1}{R_c^2}[Q_2]\boldsymbol{R}_c$		

As might be expected, the force expression is symmetric, if one changes the sign on all $\boldsymbol{R}_c$ terms and switches the subscripts the force on body 1 is found to be equal in magnitude but opposite in direction to the force on body 2. This satisfies Newton's 3$^{\text{rd}}$ law.

A.2.2 Torque Derivation

The torque on body 2 is given by $\boldsymbol{T}_2 = \int_{B_1}\int_{B_2} \boldsymbol{r}_2 \times \mathrm{d}\boldsymbol{F}$, where the same binomial expansion as before is used to approximate $\mathrm{d}\boldsymbol{F}$ to second order.

$$\boldsymbol{T}_2 = \frac{1}{4\pi\epsilon_0 R_c^3}\int_{B_1}\int_{B_2} \boldsymbol{r}_2 \times (\boldsymbol{R}_c + \boldsymbol{r}_2 - \boldsymbol{r}_1)\left(1 - \frac{3(\boldsymbol{R}_c\cdot\boldsymbol{r}_2 - \boldsymbol{R}_c\cdot\boldsymbol{r}_1)}{R_c^2}\right)\mathrm{d}q_2\mathrm{d}q_1 \quad \text{(A.21)}$$

Because of the extra $\boldsymbol{r}_2$, many of the terms in the differential force expansion become third order and are neglected. The differential torque has three parts corresponding to the $\boldsymbol{r}_2 \times \boldsymbol{R}_c, \boldsymbol{r}_2 \times \boldsymbol{r}_2$ and $\boldsymbol{r}_2 \times \boldsymbol{r}_1$ components. The middle term is zero and the first and third are labeled by $\boldsymbol{T}_{2_0}$ and $\boldsymbol{T}_{2_1}$, respectivley. $\boldsymbol{T}_{2_0}$ is evaluated first:

$$\boldsymbol{T}_{2_0} = \frac{1}{4\pi\epsilon_0 R_c^3}\int_{B_1}\int_{B_2} \boldsymbol{r}_2 \times \boldsymbol{R}_c\left(1 - \frac{3(\boldsymbol{R}_c\cdot\boldsymbol{r}_2 - \boldsymbol{R}_c\cdot\boldsymbol{r}_1)}{R_c^2}\right)\mathrm{d}q_2\mathrm{d}q_1 \quad \text{(A.22)}$$

$$= -\frac{1}{4\pi\epsilon_0 R_c^3}\boldsymbol{R}_c \times \int_{B_1}\int_{B_2} \boldsymbol{r}_2\left(1 - \frac{3(\boldsymbol{R}_c\cdot\boldsymbol{r}_2 - \boldsymbol{R}_c\cdot\boldsymbol{r}_1)}{R_c^2}\right)\mathrm{d}q_2\mathrm{d}q_1 \quad \text{(A.23)}$$

Where higher order terms in the binomial expansion are neglected. The integral is identical to the force integral in Eq.(A.13) evaluated earlier, and is written down from inspection as:

$$\boldsymbol{T}_{2_0} = -\boldsymbol{R}_c \times \left[\frac{Q_1\boldsymbol{q}_2}{R_c^3} + \frac{3(\boldsymbol{R}_c\cdot\boldsymbol{q}_1)\boldsymbol{q}_2}{R_c^5} + \frac{3Q_1[Q_2]\boldsymbol{R}_c}{R_c^5}\right] \quad \text{(A.24)}$$

The other part of the torque comes from the $\boldsymbol{r}_1$ and is evaluated below:

$$\boldsymbol{T}_{2_1} = -\frac{1}{4\pi\epsilon_0 R_c^3}\int_{B_1}\int_{B_2} (\boldsymbol{r}_2 \times \boldsymbol{r}_1)\mathrm{d}q_2\mathrm{d}q_1 \quad \text{(A.25)}$$

The binomial expansion here is truncated to just the first term because the $\boldsymbol{r}_2 \times \boldsymbol{r}_1$ term is already second order. This gives

$$\boldsymbol{T}_{2_1} = -\frac{1}{4\pi\epsilon_0 R_c^3}\boldsymbol{q}_2 \times \boldsymbol{q}_1 \quad \text{(A.26)}$$

The total torque is found by summing $\boldsymbol{T}_{2_0}$ and $\boldsymbol{T}_{2_1}$ to yield

$$\boldsymbol{T}_2 = \frac{1}{4\pi\epsilon_0 R_c^3}\left[Q_1\boldsymbol{q}_2 \times \boldsymbol{R}_c + \frac{3(\boldsymbol{R}_c \cdot \boldsymbol{q}_1)\boldsymbol{q}_2 \times \boldsymbol{R}_c}{R_c^2} - \frac{3Q_1\boldsymbol{R}_c \times [Q_2]\boldsymbol{R}_c}{R_c^2} + (\boldsymbol{q}_1 \times \boldsymbol{q}_2)\right] \tag{A.27}$$

This equation is visualized in Table A.2 which follows Table A.1 in omitting the factor of $4\pi\epsilon_0 R_c^3$ and grouping terms by their order in the dimensionless ratio r/R_c. Terms closer to the upper left corner are lower order.

Table A.2: Torque ordering matrix

	Q_1	$\boldsymbol{q}_1$	$[Q_1]$
Q_2			
$\boldsymbol{q}_2$	$Q_1\boldsymbol{q}_2 \times \boldsymbol{R}_c$	$\frac{3}{R_c^2}(\boldsymbol{R}_c \cdot \boldsymbol{q}_1)\boldsymbol{q}_2 \times \boldsymbol{R}_c + (\boldsymbol{q}_1 \times \boldsymbol{q}_2)$	
$[Q_2]$	$-\frac{3}{R_c^2}Q_1\boldsymbol{R}_c \times [Q_2]\boldsymbol{R}_c$		

As expected, there are no zeroth order terms, in fact there are no terms at all corresponding to the scalar charge Q_2. Unlike the force expansion, the torque is not symmetric, i.e. $\boldsymbol{T}_1 \neq -\boldsymbol{T}_2$. This is because the torque on body 1 and body 2 are not measured about the same point, but rather the center of mass of each body. If all torques are measured about the same point, such as the barycenter of the system, the torques are equal and opposite and cancel out and are not able to change the angular momentum of the system.